Pulse Emission Properties of Radio Pulsars

A Thesis Submitted for the degree of

Doctor of Philosophy

(In Physics)

to

UNIVERSITY OF PUNE

by

B. C. Joshi

National Center for Radio Astrophysics

Tata Institute of Fundamental Research

Pune 411 007

September 2000

Contents

List of Tables

List of Figures

Acknowledgements

I express my gratitude to Dr. M. Vivekanand for his guidance and encouragement during the course of this thesis work. It was his introduction to pulsar astronomy, which interested me in this field. It has been a pleasure to learn new concepts and ideas from him. I also wish to thank him for his personal support, especially in times of difficulties.

My interest in astronomy in general and radio astronomy in particular was motivated by several popular science articles by Prof. J. V. Narlikar. I express my gratitude for his encouraging words at a chance meeting of Astronomical Society of India meeting in 1984 which prompted me to take astronomy as a career. I am also thankful to Prof. T. Padmanabhan for his encouraging remarks. His excellent course on Statistical mechanics aroused my interest in basic Physics and gave me an opportunity to understand it in a new perspective.

I am thankful to the observers and staff of Ooty Radio Telescope for their help during observations. I also wish to thank Prof. Kandaswamy Subramanian for illuminating theoretical discussions and Prof. D. J. Saikia for his help in sorting out matters related to the Graduate school and University.

A special thanks is due to V. Venkatsubramani and Shekhar in resolving any problems I had with the computing facility at NCRA. I also wish to thank Mrs. Sunita Barve for helping out in obtaining reference articles, which were not easily available and in other library related matters. I am grateful to Shri Prem Kumar for providing me with an excellent photograph of Ooty Radio Telescope. I thank colleagues and students at NCRA, particularly C. H. Ishwar Chandra and S. Jeykumar, for their help regarding Latex and format of thesis.

Finally, I am deeply indebted to my wife Anjali for her support, despite the total lack of attention to household matters on my part, while I was writing this thesis.

Declaration

CERTIFIED that the work incorporated in this thesis entitled **Pulse Emission Properties of Radio Pulsars** submitted by **B. C. Joshi** was carried out by the candidate under my supervision. Such material as has been obtained from other sources has been duly acknowledged in the thesis.

B. C. Joshi
Candidate

Dr. M. Vivekanand
Thesis Supervisor

Place: Pune
Date: September 22, 2000

ABSTRACT

Pulsating radio sources, or Pulsars, are sources that give out broadband radio emission in the form of periodic pulses. A superposition of several of these pulses gives an integrated profile which is characteristic for each pulsar. The integrated pulse profile remains stable over long time scales for most pulsars. However, some pulsars often switch between two or more stable profiles, a phenomenon known as "mode-changing". The integrated profile represents the average emission properties and it often conceals a rich diversity of behaviour among individual pulses. The components of an individual pulse, called subpulses, often occur at random phases within a time window defined by the integrated profile. However, in pulsars such as PSR B0809+74 and PSR B0031-07, subpulses appear at progressively changing positions in successive periods. This marching of subpulses is called "drifting". Sometimes, no emission is detectable for a few pulses, a phenomenon called "pulse nulling". These three phenomena provide an excellent probe for testing models of the pulsar radio emission mechanism, which is not well understood. The subpulse is regarded as one of the basic units of emission and it is supposed to represent the radiation from an isolated location within the distribution of locations covered by the integrated profile. The properties of subpulses thus probe the instantaneous changes in the emitting regions and their study may provide vital clues to the radio emission mechanisms of pulsars. Because of the relatively short periods of pulsars ($\sim$ 1 s, even milliseconds) and low flux densities ($\sim$ 100 mJy at 408 MHz), the individual pulse shapes and their properties have not so far been studied as extensively as the average properties of pulsars. In particular, it is important to study the relationship between "drifting", "nulling" and "mode-changing" in the same pulsar. This can be done in a handful of pulsars which exhibit all the three phenomena. An investigation into the individual pulse properties of PSR B0031-07, which exhibits the above phenomena, is carried out in this research work.

Drifting was first noticed in PSR B1919+21 and PSR B2016+28 by Drake and Craft (1968). Only two or three pulsars exhibit organized drifting (Rankin 1986). PSR B0809+74 has a unique drift rate, whereas PSR B0031-07 exhibits three distinct drift rates. Quantitative study of the subpulse properties, such as the separation between the drifting subpulses (also referred to as P2), as a function of drift rate have not been reported before. A given drift band, *i.e.* an association of subpulses over successive periods, is linear to a first order, although a variation in the drift rate with pulse position has been reported (Backer 1973; Krishnamohan 1980; Proszynski and Wolszczan 1986). The variation at the edges of the integrated profile has not been studied extensively. The origin of drifting is explained in the currently popular model by invoking $\mathbf{E} \times \mathbf{B}$ drift of sparks (or bursts of charges) in the vacuum gap above the pulsar. It is believed that the coherent radio emission, which is locked to these sparks, follows the drifting of sparks (Ruderman and Sutherland

1975). Thus, this model implies a full series of well separated subpulses outside the pulse window (Curtis Michel 1991). The sparks are separated by a distance of the order of gap height which is also related to its drift speed in this model. This suggests that the subpulse separation increases with drift rate, although this observational implication has not been stated explicitly either in Ruderman and Sutherland (1975) model or its subsequent modification and a new study to test this is required. The drift rate is supposed to be enhanced at the edges of the integrated profile.

In some pulsars such as PSR B1237+25 and PSR B1133+16, no pulse emission is observed for several pulses. This phenomenon was first reported by Backer (1970c) and has since been seen in several pulsars (Ritchings 1976; Rankin 1986; Biggs 1992; Vivekanand 1995). Null duration can range from a single period to several hundred pulses. It is important to know the factor by which the radio emission from pulsars decreases during a null. This factor has been estimated as ~ 100 for PSR B1944+17 (Deich et al. 1986) and for PSR B0031-07 (Vivekanand 1995). The mean energy in null state is estimated as -0.23 ± 0.43 per cent for PSR B0809+74 (Lyne and Ashworth 1983). It has been suggested that nulling occurs because of loss of coherence in a steady discharge of the vacuum gap (Filippenko and Radhakrishnan 1982), but this is not confirmed yet.

Mode-changing was first noticed in PSR B1237+25 by Backer (1970a) and is observed in several other pulsars such as PSR B0329+54, PSR B0355+54, PSR B2045-16 (Helfand, Manchester and Taylor 1975; Morris et al. 1980; Bartel et al. 1982). The changes in the integrated profile in some mode-changing pulsars depend upon their drifting behaviour. For instance, PSR B2319+60 is believed to exhibit three drift rates and the integrated profile for each drift rate is different (Wright and Fowler 1981a). A similar behaviour has been indicated in case of PSR B0031-07, but a detailed analysis of this pulsar has not been reported. No explanation for mode-changing has been proposed, although it is conjectured that a mode-change involves a redistribution of the excitation over several components (Lyne and Graham-Smith 1990).

In some pulsars, at least two of the three phenomena, namely "drifting", "nulling" and "mode-changing", have been seen. Wright and Fowler (1981b) note a connection between drifting and mode-changing in PSR B0031-07, but no figure is shown to substantiate this claim. A disturbance of the subpulse drifting at nulls was first noted for PSR B0809+74 by Cole (1970). A sudden change of drift rate at the start of null followed by an exponential relaxation to the normal drift rate was reported for this pulsar, and it was suggested that the change of subpulse position during the null is proportional to null length (Page 1973; Unwin et al. 1978; Lyne and Ashworth 1983). On the other hand, no evidence for memory of subpulse position across nulls was observed for PSR B1944+17 (Deich et al. 1986). Thus, there is no consensus on this issue. The inter-relationship between these three phenomena is not yet clearly understood.

The main objective of this research work was to study these phenomena and their relationship with each other in a pulsar which exhibits all these phenomena. In particular, it was proposed to obtain the distribution of drift rates for such a pulsar and study its subpulse properties as a function of drift rates. It is also useful to study the variation of drift rate at the edge of the integrated profile

and obtain the average sub-beam pattern of the pulsar. Lastly, it was proposed to investigate the connection between drifting and mode-changing and the interaction between nulling and drifting. Thus, this work was carried out with two main scientific objectives - (1) to verify the implications of Ruderman and Sutherland model cited above by studying the the subpulse properties both as a function of drift rate as well as after removing the drift in a systematic drifting pulsar and (2) to study the connection between drifting and mode-changing as well as that interaction between nulling and drifting phenomenon in the same pulsar. The main thrust of the work is to understand the inter-relationship between the three phenomena mentioned earlier and to provide observational constraints to motivate further development of theoretical models.

Very few pulsars exhibit organized drifting and significant nulling. In most pulsars, drifting is sporadic (PSR B1944+17), variable (PSR B2016+28) or across small portions of the integrated profile (PSR B1237+25, PSR B1919+21 and PSR B1632+24) (Rankin 1986; Proszynski and Wolszczan 1986; Hankins and Wolszczan 1987). A much smaller subset of these drifters exhibit significant nulling. Among these, the organized drifting is exhibited by barely two pulsars - PSR B0809+74 and PSR B0031-07. As mentioned before, pulsars are weak radio sources and a sensitive instrument is required for an individual pulse study. Several hours of observing time, required for the kind of analysis reported in this thesis, was available to us at Ooty Radio Telescope, or ORT (Swarup et al. 1971). PSR B0809+74 is unfortunately not observable with ORT because its limit of declination ($\approx \pm 55°$) is smaller than the declination of this pulsar ($+74°$). On the other hand, the only instrument available for high sensitivity observations of PSR B0031-07 is ORT as the declination of this pulsar is -7 degrees. Therefore, this thesis concerns with the individual pulse properties of the only other systematic drifting pulsar PSR B0031-07.

PSR B0031-07 is a pulsar with a period of 0.94295 s and a mean flux of 100 mJy at 326.5 MHz. It has a smooth integrated profile with a width of approximately 130 ms. A typical period has two peaks of emission or subpulses. The subpulses exhibit a systematic advancement of phase from the trailing edge to the leading edge of the integrated profile with increasing period number. The values of drift rates for various drift bands fall in three distinct classes called Class A, B and C (Huguenin, Taylor and Troland 1970). This pulsar also exhibits nulling for 44.6 ± 1.3 per cent of time (Vivekanand 1995). Both short as well as long nulls are observed. Thus, this pulsar presents a good opportunity to study the subpulse properties as a function of drift rate and to explore the relationship between the drifting and the nulling phenomena, which were the main objectives of this thesis.

This pulsar was observed using ORT at a frequency of 326.5 MHz with a bandwidth of 9 MHz and data were obtained on approximately 40000 periods. This data set was analyzed to estimate the drift rates and other pulse properties described in this thesis. A set of programs was especially developed for this purpose and a brief description of data reduction procedure is given below. The data were calibrated using the flux of a calibrator source and weighted using the dynamic spectra of the pulsar. Then, the energy in the on-pulse window (the duration when the pulsar's

energy is received) and that in the off-pulse window were estimated approximately by summing the highest 3 to 5 samples within the respective windows. This method gives a better estimate of the on-pulse energy for pulsars such as PSR B0031-07 as the number of samples in an individual pulse is a small fraction of that in the integrated profile. All periods with on-pulse energy below a threshold, defined as the sum of the mean off-pulse energy and 5 times its standard deviation, were considered as nulled pulse. The subpulses in the individual periods were then modeled as Gaussians. The centroid of the Gaussian was taken as the position of the subpulse and the width of the Gaussian as a measure of root mean square error on the position. The drift bands were then visually selected and a straight line was fitted in the least square sense to each of the 3338 bands in the data. The drift rate of a given band was taken as the slope of the fitted line. Thus, the nulled and burst periods were identified and the drift rates were determined in the first phase of the analysis. The calibrated data were then analyzed with another set of programs to determine the subpulse properties and its correlations with drift rates both during the bursts and across nulls.

The main results of this analysis are enumerated below.

1 The pair of drifting subpulses are well separated. More than two subpulses are sometimes seen consistent with the existence of several sparks marching around the polar cap implied by Ruderman and Sutherland (1975) model.

2 The drift rate is enhanced at the edge of the integrated profile as expected on the basis of Ruderman and Sutherland model. The path of a drifting subpulse seems to be consistent with at least a third order polynomial for Class B drift bands whereas it is more or less linear for Class A bands.

3 Measurements of the drift rate for 3338 drift bands are presented in this thesis. Three drift modes can be inferred from the observed distribution centered at -4.05 ms period^{-1} (Class A), -7.78 ms period^{-1} (Class B) and -11.46 ms period^{-1} (Class C). The former two are dominant modes for this pulsar occurring in 15.6 % and 81.8 % of pulses whereas the last mode occurs rarely. These results are consistent with the values quoted by Huguenin, Taylor and Troland (1970).

4 There is a significant feature in the spectrum of the nulling pattern indicating that nulling is perhaps quasi-periodic in this pulsar. This spectral feature is consistent with a much weaker feature reported by Huguenin, Taylor and Troland (1970).

5 The average value of the subpulse width is 7.44 ms and is independent of the drift rate. The subpulse energy is higher in the dominant drift mode (Class B), but no correlation is apparent with drift rate otherwise. These measurements have been reported for the first time.

6 The average spacing P_2 between the two drifting subpulses increases monotonically with the modulus of drift rate, contrary to the observational belief held so far. This is a new result of the thesis.

7 The energies of adjacent subpulses are anti-correlated and this suggest a competition between the subpulses. Such a phenomenon is being reported for the first time in any pulsar.

8 The pulses belonging to the three drift modes for this pulsar add upto three integrated profiles, which are significantly different. This result demonstrates a possible connection between drifting and mode-changing and is consistent with a qualitative result reported earlier (Wright and Fowler 1981b). The three profiles are being reported for the first time.

9 The average pulse for the Class A mode arrives earlier than that for Class B mode. There is a similar shift in longitude between Class B and Class C. The RMS width of the profile decreases progressively from Class C mode to Class A. However, these results should be treated with caution as our data are single polarization data.

10 The data imply a phase correlation across nulls which decreases with null duration. This result, together with the reported behaviour of PSR B1944+17 and PSR B0809+74, imply different time scales for phase correlation in different pulsars and is being reported for the first time.

11 The drift rate during the short nulls appears to be constant for Class A drift mode transitions, whereas it decreases with null duration for Class B transitions. This suggests a relationship between drifting and nulling in this pulsar.

A detailed study of single pulses in PSR B0031-07 was presented in this thesis discussing drifting, nulling and mode-changing phenomena in this pulsar. In summary, our results indicate that PSR B0031-07 operates in three (possibly four) different modes. These modes are characterized by different fluctuation properties as well as different integrated profile and they may be associated with changes in the properties of vacuum gap in the Ruderman and Sutherland framework. It appears that the radial distance of the emission region from the star is different in different modes of the pulsar. Our results appear to suggest the existence of distinct time-scales over which the pulsar radiation changes in a characteristic fashion and drifting, nulling and mode-changing seem to be observational manifestations of such time scales. Thus, these results broadly support Ruderman and Sutherland model, although many of these motivate the further development of this model and provide observational constraints for such modifications. It appears that "drifting", "mode-changing" and "nulling" are related phenomena and may find a common explanation by elaborating the basic Ruderman and Sutherland model.

The thesis is mainly based on the following publications

1. M. Vivekanand and **B. C. Joshi**, "The drifting behavior of PSR B0031-07", 1997, Astrophysical Journal, 477, 431

2. M. Vivekanand and **B. C. Joshi**, "Competing drifting subpulses in PSR B0031-07", 1999, Astrophysical Journal, 515, 398

3. **B. C. Joshi** and M. Vivekanand, "A study of Sub-pulse Phase Correlation across Nulls in PSR B0031-07", 2000, Monthly Notices of Royal Astronomical Society, 316, 716

4. **B. C. Joshi** and M. Vivekanand, "Constraints on Emission Mechanism from the Nulling and Drifting Pulsar PSR B0031−07", 2000, in Proceedings of IAU Colloquium 177 - "Pulsars, 2000 and Beyond", eds. M. Kramer, N. Wex and R. Wielebinski, 202, 173

Chapter 1

Introduction

The discovery of clocklike radio pulses from compact objects in our galaxy (Hewish et al. 1968) marked the beginning of a new field of radio astronomy. These objects are called Pulsating radio sources, or Pulsars, and have stimulated astrophysical research for over three decades. In recent times, many of these have also been detected at higher frequencies. They exhibit a rich and varied phenomenology which is probably due to the extreme magnitude of magnetic and electric fields as well as densities existing in these stars. They provide an unconventional laboratory for testing physical theories of matter under such extreme conditions. These stars have also been used to test the general theory of relativity and as important probes of inter-stellar medium. This thesis presents a detailed observational study of the radio emission from one such source, PSR B0031−07.

The radio emission of pulsars is in the form of a train of highly periodic pulses. The most remarkable property of this emission is the stability of its period, which is comparable to best atomic time standards. The periods range from 1.5 ms to 8.5 s and these increase with time. These timing properties suggested a compact and massive source. Two such sources are known from stellar evolution theories - white dwarfs and neutron stars. While the timing properties of pulsars cannot be explained by the radial oscillations of a single class of compact stars or by the orbital period of a binary system, they are in accord with a rotating neutron star model. Hence, these sources were identified as rotating magnetized neutron stars soon after their detection (Gold 1968; Pacini and Salpeter 1968; Pacini 1968; Gold 1969). In this picture, the pulse is supposedly formed by a narrow beam of radiation, anchored on the star, that sweeps across the observer's line of sight as in a lighthouse.

These neutron stars are compact cores left behind in the aftermath of the explosion of the progenitor star. Such explosions are called supernova. The neutron star and its accompanying supernova remnant (SNR) were predicted much before the discovery of pulsars by Baade and Zwicky (1934) in the course of their investigations of supernova light curves. It is known from the stellar evolution theory that the nuclear fuel is exhausted in the proto-core of the star in such an explosion and its large mass can only be supported by degenerate neutrons. Hence, these stars are primarily made up of superfluid neutrons. The typical mass of such stars is believed to be $1.4 M_{\odot}$

and their radius is in the range of $10 - 16$ Km. Depending on the equation of state, the central density of these stars is between 10^{14} to 10^{15} gm cm^{-3}. Thus, these stars posses a large moment of inertia (10^{44} gm cm^{-3}) (Lyne and Graham-Smith 1990).

The typical radio luminosity of pulsars is of the order of 10^{25} ergs s^{-1} (Michel 1991). The large moment of inertia of the star together with the slow-down in the rotation rate of pulsar (typical increase in period is 10^{-15} s/s) implies a loss of rotational kinetic energy of the star of the order of 10^{31} ergs s^{-1}, which is at least five orders of magnitude more than their typical radio luminosity. Hence, these sources are also sometimes referred as rotation powered pulsars. If one makes a simple assumption that this loss is due to dipole radiation by a uniformly magnetized rotating sphere, an estimate for the magnetic field of the neutron star can be obtained. This estimate, often called the spin-down estimate, is of the order of 10^{12} G for a vast majority of pulsars indicating that these are highly magnetized stars.

The radio emission of pulsars is observed from meter waves to millimeter waves. The distance and the radio luminosity of pulsars indicate a very high brightness temperature for these sources. Hence, this emission is unlikely to be due to thermal or incoherent synchrotron emission. Another observed characteristic of pulsar radio emission is the rich and varied phenomenology associated with it. Despite several attempts in the last three decades, the mechanism responsible for this emission has not been well understood. While theoretical models are faced with problems of inconsistency, not many observational studies focusing on the relationship between the varied phenomenology have been carried out. In this thesis, a study of the relationships between the phenomena representing the dynamics of pulsar radio emission for an interesting pulsar, PSR B0031−07, has been presented.

1.1 Pulsar population and distribution

The total number of radio pulsars that have been detected so far (till 2000 AD) is approximately 1300 (Camilo et al. 2000). Most of these stars were detected by their radio emission. The only exceptions are PSR B1509−58, PSR B0540−69 and PSR J0633+1746, which is also known as Geminga. While the former two were detected in X-rays first (Seward and Harnden 1982; Seward 1984), Geminga was discovered in gamma rays (Halpern and Holt 1992; Bertsch et al. 1992). A handful of radio pulsars have also been observed to emit pulsed radiation in optical, X rays and gamma rays. The radiation properties of these stars at high energies are remarkably different from those at radio wavelengths.

All but five of the pulsars discovered so far are in our galaxy. The five extra-galactic pulsars are associated with nearest satellite galaxies to Milky way, the Magellanic Clouds. The galactic pulsars are distributed near the galactic disk with typical scale height of 400 pc as opposed to 50 - 100 pc for supernova remnants and massive stars, which are believed to be the progenitors of these stars. This larger scale height is probably due to their observed relatively large peculiar

transverse velocities, which are typically 300 km s^{-1} (Lyne and Lorimer 1994). A vast majority of these objects are isolated neutron stars, although many residing in a binary system have also been discovered. A handful of these stars are associated with supernova remnants. Such associations were a strong argument in favour of the neutron star model for these sources in the first decade of their discovery, although the much larger population sample available today indicates that only a small percentage of observed pulsars have a visible SNR shell associated with it.

In the recent years, three distinct classes of radio pulsars have begun to emerge. A vast majority of pulsars have periods in the range of 0.1 s and a couple of seconds. The typical rate of increase of this period for these pulsars is of the order of $10^{-15}s/s$. Thus, the typical spin-down estimate for the magnetic field of these stars is of the order of 10^{12} G and these are often called "normal" population of pulsars. On the other hand, a small fraction of pulsars have very short periods (1 - 20 ms) and a small change of period ($10^{-18}s/s$), indicating a magnetic field of the order of 10^9 G. Further, almost half of such pulsars are found in binary systems in contrast with the normal pulsars. Many of them are found in globular clusters of our galaxy and these are known as "millisecond" or "recycled" pulsars. It is believed that these are very old neutron stars and their evolution is very different from the normal variety of pulsars.

In the last couple of years, a third class of pulsars has begun to emerge. Unlike the normal and the millisecond pulsars, these have fairly long periods (typically few seconds) and large rate of increase of periods (typically $10^{-13}s/s$) suggesting a very high magnetic field (10^{13} G). These share their timing properties with a new class of high energy sources, *namely*, Anamolous X-ray pulsars and Soft Gamma ray Repeaters. Although only a couple of confirmed examples are known so far, it appears that this sample will be enhanced soon by the currently ongoing pulsar searches (Camilo et al. 2000).

1.2 Observational characteristics of pulsar radio emission

The individual pulses from pulsars vary a great deal, but when these are averaged over several pulses a remarkably stable integrated pulse profile is obtained. This profile is characteristic of each pulsar. The typical width of this profile is of the order of 10°, where 360° represents the full spin period of the pulsar. The integrated pulse profile remains stable over long time scales for most pulsars. However, some pulsars often switch between two or more stable profiles, a phenomenon known as "mode-changing". The individual pulses are made up of two or more components called subpulses with typical width of few degrees. On a much shorter time-scale (10 - 100 μs), micropulses with widths less than a degree are observed. The integrated profile and the subpulses are believed to be due to the rotation of a narrow beam emanating from the polar cap of the neutron star, whereas the micropulses are believed to be a temporal modulation of this emission. The narrow widths of subpulses and the microstructure indicate that pulsar radiation involves some form of relativistic beaming.

Pulsars exhibit a large variety of integrated profile shapes. The profiles are smooth curves, generally with one to three components, more rarely with five components. The profiles usually become narrower with increasing frequency of observation. The shape of the profile also evolves with frequency in most pulsars. A classification of pulsars based on the spectral evolution of the morphology of their profiles was proposed by Rankin (1983). She noted that the integrated profile for some pulsars with single component profile characteristically evolve by broadening and ultimately bifurcating at progressively lower frequencies. Similarly, the integrated profile, for other pulsars with two component profiles, narrows and even merges at a high frequency. The profiles of such pulsars have relatively larger widths. These pulsars, which also have similar timing and polarization properties, were called conal single or conal double pulsars in the classification scheme mentioned above. In contrast, many other pulsars exhibit a single component integrated profile with widths much less than that of the conal profiles. At progressively higher frequencies, the profile for such pulsar changes form by attaching a pair of outriders. The central component has a steep spectrum and is marked by significant circular polarization, which changes its sense at the center of the profile. This latter class of pulsars is called as core single pulsars. In case of pulsars with more than two components in their integrated profile, the properties of the central component of the profile often resemble those of the component of the core single pulsars, whereas the outer components are similar to the components of conal single or double pulsars.

Since the integrated profile represents the average emission properties of the pulsar, its shape can be interpreted in terms of the geometry of the emission beam of pulsar. The abovementioned study of the morphology of the profile indicates that this beam is probably organized as a set of nested cones around the magnetic axis of the pulsar (Rankin 1983). The central beam in this picture is called as core beam. This beam is surrounded by a set of hollow cones concentric with it and these are referred as conal beams in this phenomenological model.

The pulsar radio emission is characterized by high linear polarization which reaches upto 100 percent in subpulses for some pulsars. The integrated profiles are often polarized upto 50 percent. The linear polarization angle usually varies monotonically across the integrated profile. This simple pattern of polarization suggests that the pulsar radiation must emanate from the neighbourhood of magnetic poles (Radhakrishnan and Cooke 1969). A small degree of circular polarization is usually detected and this reverses its sense near the center of the profile. These polarization properties are very similar to those of curvature radiation produced by relativistic charges moving in a curved flux-tube. In some pulsars, the polarization angle exhibits jumps of around 90 degrees and this phenomenon is called orthogonal mode change. The simultaneous existence of both linear and circular polarization is a notable feature of the pulsar radiation.

It has already been mentioned that the typical radio luminosity of pulsars is of the order of 10^{25} ergs s^{-1}. Since these stars are at a typical distance of 1 Kpc, this luminosity represents a brightness temperature of $10^{29}\ ^{\circ}K$. Such large kinetic temperatures are not possible for a "dead" star like neutron star. So, the nature of this radiation is not thermal. The strong magnetic field of

the star suggests a non-thermal mechanism such as synchrotron radiation. A relativistic particle quickly loses its energy in the strong magnetic field of the pulsar. The magnitude of this loss by synchrotron radiation is too small to account for the radio luminosity of pulsars. At the same time, most of this radiation lies in the X-ray range, so this mechanism cannot explain the radio radiation. Another likely mechanism for particles to radiate is the curvature radiation, which is produced when the relativistic particles move along a curved magnetic field line. However, the power output per particle falls far short of that required to explain the typical radio luminosities. Thus, the high brightness temperature of pulsars cannot be explained by any incoherent mechanism. However, coherent curvature radiation by a bunch of relativistic electrons can explain such temperatures. Alternative coherent mechanisms such as maser curvature radiation and linear acceleration mechanism have also been proposed to explain such high temperatures (Melrose 1993).

The random electron density fluctuations over very wide range of spatial scales in the inter-stellar medium cause random intensity fluctuations in the pulsar signal called inter-stellar scintillation. If the inter-stellar medium is considered as a screen or lens with inhomogeneities, the pulsar signal scattered by it produces an intensity modulation in frequency and space. Additionally, a temporal modulation is caused by the motion of pulsar with respect to the screen. These variations are called Diffractive inter-stellar scintillation (DISS) and are usually studied through plots of intensity with both time and frequency called dynamic spectra. In addition, the propagation of pulsar signal through large-scale electron density inhomogeneities gives rise to a variation in flux over long time scales (typically more than a day), a phenomenon called Refractive inter-stellar scintillation (RISS).

The radio emission is broadband and is seen from few tens of MHz to several GHz. This emission has a steep spectrum in general. However, RISS described above makes accurate determination of pulsar spectrum very difficult. The determination of pulsar flux at different frequencies over several epochs to take care of RISS effects have indicated that the pulsar radio emission has a mean spectral index of 2.0.

The integrated profile represents the average emission properties and it often conceals a rich diversity of behaviour among individual pulses. Pulsars exhibit variations in the intensity subpulses from pulse to pulse after the effect of inter-stellar scattering is taken into account. The individual pulse intensity in some pulsars have a normal distribution with a well defined mean, whereas a few pulsars show an asymmetric distribution with a long high intensity tail. These intensity variations are sometimes associated with subpulse phenomena described below.

The subpulses often occur at random phases within a time window defined by the integrated profile. However, in pulsars such as PSR B0809+74 and PSR B0031−07, subpulses appear at progressively changing positions in successive periods. This marching of subpulses is called “drifting”. Sometimes, no emission is detectable for a few periods, a phenomenon called “pulse nulling”. These individual pulse phenomena represents the dynamics of pulsar emission as opposed to the

average spatial distribution or kinematics described by the properties of the integrated profile.

In summary, the radio emission of pulsars is characterized by the following observed properties

1. A monotonic sweep of linear polarization angle across the integrated profile
2. Co-existence of linear and circular polarization
3. Generally narrow subpulse widths
4. High Brightness Temperature
5. Spectral range of tens of MHz to tens of GHz
6. Varied integrated profile morphologies which can be interpreted as core and conal beams - Kinematics of beam
7. mode-changing, drifting and nulling - Dynamics of beam

These properties show considerable variations over the pulsar population. For example, there exists both weakly polarized pulsars as well as pulsars with almost 100 percent polarization. Some of these variations may have a geometric origin, but this has not been unequivocally established.

1.3 Pulsar models

An explanation of the radio emission properties described in the last section has proven to be a difficult task in the last three decades. Although several attempts have been made, most pulsar models have been beset with inconsistencies. A brief account of the proposed models in the literature is given in this section.

1.3.1 Goldreich-Julian model

One of the earliest models was the Goldreich-Julian model in which an aligned rotator was considered. Considering the neutron star to be a perfectly conducting sphere with a dipolar external magnetic field, it was shown that the external electric field, in case of a magnetosphere without any charges, is quadripolar in nature. This vacuum external electric field has a non-zero component along the magnetic field. Its value at the surface is given by

$$E_{\|} \approx 6 \times 10^{10} B_{12} P^{-1} \qquad (\mathrm{V\ cm^{-1}}) \tag{1.1}$$

where P is the period of pulsar in seconds and B_{12} is the surface magnetic field in units of 10^{12} G. The magnitude of the electric force experienced by charges on the surface is much larger than the gravitational force. Provided the binding energies of these particles are not very large, this implies that the charges will be ripped off from the surface filling the magnetosphere. Thus, the magnetosphere cannot be empty; there must be plasma distribution in it (Goldreich and Julian 1969).

The charges in a plasma-filled magnetosphere, with infinite conductivity and negligible particle inertia, satisfy the following relation

$$\overline{\mathbf{E}} + \frac{1}{c}\left(\overline{\Omega} \times \overline{\mathbf{r}}\right) \times \overline{\mathbf{B}} = 0 \tag{1.2}$$

The charge distribution screens the parallel electric field given by Equation 1.1 and this leads to their rigid corotation with star. The electric charge distribution in the magnetosphere is given by

$$\rho_c = -\frac{1}{2\pi c}\overline{\Omega} \cdot \overline{\mathbf{B}} \qquad (\text{ cm}^{-3}) \tag{1.3}$$

where Ω is the rotation frequency of the star in Hz and $\mathbf{B}$ is the magnetic field in G. This density is also called the Goldreich-Julian density.

The strict corotation implied above cannot exist beyond the surface where the tangential velocity equals the speed of light. This surface is cylindrical in shape. Its radius is therefore called radius of light cylinder and is given by

$$R_L = \frac{c}{\Omega} \qquad (\text{cm}) \tag{1.4}$$

The charges on the magnetic field lines with a maximum equatorial radius smaller than R_L corotate with star. The magnetic field lines, which would have a maximum equatorial radius larger than R_L in absence of rotation, penetrate the light cylinder and become open field lines. The open field lines define a region in the polar cap with a radius

$$R_p = R\left(\frac{\Omega R}{c}\right)^{\frac{1}{2}} \approx 1.4 \times 10^4 P^{-\frac{1}{2}} \qquad (\text{cm}) \tag{1.5}$$

The charge particles along the open field line escape to infinity and are replenished by the stellar surface. This outflow of charges is referred to as Goldreich-Julian outflow and these charges are believed to be responsible for the radio radiation in most of the models.

Many features of this model re-appear in the later models. This model was successful in explaining the energetics of pulsars and the injection of charged particles in the supernova remnant around the pulsar. However, it did not explain the details of the observed radio emission. This was attempted in the models described below while retaining the essential features of this model.

1.3.2 Rotating vector model

Radhakrishnan and Cooke (1969) proposed a rotating vector model based on the their observations of the polarization angle swing in Vela pulsar. In this model, the relativistic particles stream out from a polar cap in a manner similar to Goldreich-Julian model. They are however constrained to move along the magnetic field lines due to the strong magnetic field of the star. Since the magnetic field lines are curved, this motion generates curvature radiation with a plane of polarization parallel to the magnetic field line. This model was therefore successful in explaining the polarization angle swing in Vela pulsar. It also implies a hollow cone geometry of the pulsar beam (Komesaroff 1970). The variation of integrated profile with wavelength of observation was also explained. Hence, some

of its features were incorporated in later models. On the other hand, it was inadequate to explain three or more components, seen in the integrated profile of pulsars discovered later. It also did not give any details of the process responsible for the acceleration of particles to ultra-relativistic energies.

1.3.3 Pair Cascade

The issue of the acceleration of particles was addressed in an extension of the above model proposed by Sturrock (1971). Here, it was assumed that the charge density in the magnetosphere is given by the Goldreich-Julian density (Equation 1.3). These particles streaming from the polar cap are accelerated to Lorentz factors of 10^7 by an accelerating potential given by

$$\Delta V \approx \left(\frac{\Omega^2 R^3}{2c^2}\right) B_{12} \approx 6.6 \times 10^{12} B_{12} P^{-2} \qquad \text{(V)} \tag{1.6}$$

Here, R is the radius of the star, B_{12} is the surface magnetic field in units of 10^{12} G and P is the period of the pulsar in seconds. This is essentially the potential difference between the center and the edge of the polar cap. The accelerated particles radiate their energy by curvature radiation producing gamma ray photons. These photons in turn are involved in a magnetic one-photon pair production process (Erber 1966). These secondary pairs are also accelerated and create gamma rays leading to further pairs, resulting in a pair cascade. These pairs form bunches much above the polar cap. The observed radio emission is due to the coherent radiation by these bunches at lower frequencies.

The accelerating potential assumed in this model was calculated assuming absence of plasma in the magnetosphere above the polar cap and is an upper limit. The space charge effects may limit this potential to a value much below the critical value required to initiate a cascade. In spite of this difficulty, the idea of cascade proposed in this model was used in later models.

1.3.4 Ruderman and Sutherland model and its extensions

A major development of this model was carried out by Ruderman and Sutherland (1975). Their model incorporated many useful features of the previous models and introduced two seminal ideas concerning vacuum gaps and "sparks". Although their fundamental assumption, regarding the ion work functions, is no longer accepted (Michel 1974; Hillebrandt and Muller 1976; Fawley, Arons and Scharlemann 1977), this model is probably the only model which has been able to explain some of the intriguing aspects of the pulsar radio emission such as the "drifting subpulses". A detailed account of this model is presented in this section.

In this model, an axisymmetric but counteraligned rotator has been assumed. The corotating magnetospheric plasma above the polar cap for such a configuration has a net positive charge. Ruderman and Sutherland (1975) argued that the binding energy for ions in the surface of neutron stars are large enough so that these ions cannot be pulled out by (1) the electric field on the surface

of the neutron star, (2) by thermionic emission or (3) by collisions of backward flowing particles. Thus, they assume that the neutron star surface yields no positive ions.

At the same time, there exists an outflow of charged particles on the open field lines through the light cylinder in the steady state as mentioned in Section 1.3.1. This depletes the positive charge above the polar cap which is not replaced by an equivalent flow of charge from the stellar surface owing to the high binding energies. Thus, a vacuum gap is created above the polar caps. Now, $\mathbf{E} \cdot \mathbf{B}$ essentially vanishes wherever magnetosphere charge density is non-zero. However, the parallel electric field in the gap differs from zero and is given by

$$E_{\parallel} = \frac{2\Omega B}{c} h \qquad (\text{V cm}^{-1}) \tag{1.7}$$

where h is gap height. The accelerating potential across the gap is given by

$$\Delta V = \frac{\Omega B}{c} h^2 \qquad (\text{V}) \tag{1.8}$$

This potential is smaller than the Sturrock potential given by Equation 1.6 as the onset of a discharge described below limits the gap height to a value smaller than the polar cap radius. For the magnetospheric regions connected to the neutron star by magnetic lines of force all along which $\mathbf{E} \cdot \mathbf{B}$ does not vanish, the angular velocity of the charged particles differs from that of the neutron star itself. Thus, another implication of the existence of a gap is that the charged particles in the magnetosphere along the open field lines above the polar cap no longer corotate with the star. This leads to a drift of "sparks" as explained later which has useful observational implications.

Ruderman and Sutherland (1975) introduced for the first time the idea of spark discharges. They showed that the gap potential and height are limited by the development of this discharge which is similar to the pair cascade proposed by Sturrock (1971). In the strong magnetic field, a random gamma ray in the gap will produce a pair by the one-photon process (Erber 1966). Both the created particles are accelerated to ultra-relativistic energies by the gap potential. Since these particles move on curved magnetic field lines, they generate curvature photons with a characteristic energy

$$E_{ph} \approx \frac{3}{2} \gamma^3 \hbar c / \rho \tag{1.9}$$

where ρ is the radius of curvature of the field line. The mean free path l of these photons is given by

$$l = \frac{4.4}{(e^2/\hbar c)} \frac{\hbar}{mc} \frac{B_q}{B_{\perp}} \exp\left(\frac{4}{3\chi}\right) \tag{1.10}$$

where χ is defined as

$$\chi \equiv \frac{\hbar\omega}{2mc^2} \frac{B_{\perp}}{B_q} \tag{1.11}$$

Here, χ is assumed to be much less than 1 and B_q is the critical magnetic field

$$B_q = \frac{m^2 c^3}{e\hbar} \qquad (\text{G}) \tag{1.12}$$

and

$$B_{\perp} \equiv Bsin\theta \qquad \text{(G)} \tag{1.13}$$

θ is the angle between the direction of propagation of the photon and the magnetic field B; ω is the frequency of photon. Thus, the curvature photons are converted into secondary electron-positron pair in a distance comparable to l. The above process repeats and an avalanche of pair production proceeds exponentially till the gap height h becomes comparable to the mean free path l. Thus, the gap height is limited by this process in a quasi-steady discharge. The expression for gap height is

$$h \approx 5 \times 10^3 \rho_6^{\frac{2}{7}} P^{\frac{3}{7}} B_{12}^{-\frac{4}{7}} \qquad \text{(cm)} \tag{1.14}$$

The gap potential is given by

$$\Delta V \approx 1.6 \times 10^{12} B_{12}^{-\frac{1}{7}} P^{-\frac{1}{7}} \rho_6^{\frac{4}{7}} \qquad \text{(V)} \tag{1.15}$$

where ρ_6 is the radius of curvature of the field line in units of 10^6 cm.

The discharge develops only when the gap potential is higher than about $10^{12}V$. The gap is continually discharged by this "spark" due to flow of electrons towards the stellar surface and that of positrons towards the light cylinder.

Equation 1.15 is not valid when h becomes comparable to polar cap radius and the potential approaches the maximum value given in the Sturrock model. In older pulsars, this potential is too small to sustain a discharge and the pulsar action terminates.

The discharge at a given point of the polar cap inhibits another simultaneous discharge within a distance $\sim h$. Thus, the gap discharges through a group of localized sparks in this model. Each spark injects energetic positron beams in the magnetosphere above the gap. These positrons are no longer accelerated in this part of the magnetosphere as $\mathbf{E} \cdot \mathbf{B} = 0$ here. But, these particles get bunched due to a two stream instability and these bunches generate coherent curvature radiation by virtue of their motion along curved magnetic field lines. This radiation falls in the radio wavelength and these authors showed that it is sufficient to explain the high brightness temperatures of pulsars.

The magnetosphere above the gap does not corotate with the star as long as the charge density in the gap is zero as was noted before. Hence, the sparks in the gap do not exactly corotate with the star and they exhibit a motion with respect to the stellar surface. If the observed subpulse emission is produced by the secondary plasma injected by these sparks, the subpulses are expected to exhibit a similar drift. As mentioned in the last section, such a drift is observed and this was a great success for this model.

Apart from the subpulse drift, this model was quite successful in explaining the integrated profile shapes and widths and pulsar spectra known at the time the model was proposed and is in general accord with the observed properties of pulsars. However, several theoretical difficulties in the model were soon discovered by subsequent investigators. Firstly, the fundamental assumption regarding the ion work functions is no longer accepted (Michel 1974; Hillebrandt and Muller 1976;

Fawley, Arons and Scharlemann 1977). Thus, the formation of vacuum gap itself is not established theoretically. The model was subsequently modified by proposing that the potential drop above the polar cap may arise either from the inertia of freely released ions in a space-charge limited flow or from surface binding of ions leading to a gap formation. Pair production by thermal X-rays from the polar cap surface in the Coulomb field of relativistic ions was also proposed as an alternative mechanism in this modification (Cheng and Ruderman 1977a), but it is not clear which is the correct mechanism. Secondly, the two stream instability proposed by Ruderman and Sutherland (1975) was found to have too little growth rate (Benford and Buschauer 1977). Another alternative mechanism for bunching due to relative streaming of electrons and positrons moving along a curved field line was proposed by Cheng and Ruderman (1977b). Other alternatives have also been proposed for bunching and it is not clear which of these is the correct process. Thirdly, it was also shown that the Sturrock type pair production discharges always travel towards the magnetic axis and eventually terminate. Cheng and Ruderman (1977a) propose localization of this discharge by a hot-spot produced by the backflow of 10^{12} eV electrons to circumvent this difficulty.

All the modifications mentioned above were incorporated in a revised model where a thermostatic regulation of the gap is proposed (Cheng and Ruderman 1980). However, the theoretical aspects of these modifications are still a subject of debate. Since the basic model and its subsequent modifications are essentially extensions of the hollow cone and Goldreich-Julian model, they have limitations similar to these models. Thus, there is no explanation for a return current to compensate for the outward flow of positrons. Further, there is no explanation for the core beam indicated by complex integrated profiles.

1.3.5 Slot gap model

A significantly different approach towards a consistent pulsar model was developed by Arons and co-workers (Fawley, Arons and Scharlemann 1977; Scharlemann, Arons and Fawley 1978; Arons and Scharlemann 1979; Arons 1981a; Arons 1983). These authors considered an oblique rotator with charge densities differing from the Goldreich-Julian corotation densities. In the previous models, it was argued that a force-free $\mathbf{E} \cdot \mathbf{B} = 0$ corotation charge density exists everywhere in the pulsar magnetosphere together with an outflow of charge at speed c along the open field lines. However, this is true only if the field lines form cylindrical surfaces parallel to rotation axis. In actual practice, a flow at speed c for a curved magnetic field in an oblique rotator is halted for field lines curving away from the rotation axis (the so called unfavourably curved field lines) whereas a residual accelerating field accompanied with an outflow appears for field lines bending towards the rotation axis (favourably curved lines). A pair cascade similar to Ruderman and Sutherland (1975) model takes place on these lines forming an abrupt pair formation front. The residual fields are shorted beyond this pair formation front and a slot like gap is formed in the regions of favourably curved lines where particle acceleration takes place.

In the Ruderman and Sutherland (1975) model, the accelerating potential is smaller than the pair cascade model, which also reduces the maximum particle luminosity. This luminosity is adequate for pulsar with periods of about 1 s, but it becomes too small for fast rotating pulsars. In contrast, the slot-gap model provides a more accurate estimate for the particle luminosity over most of the range of normal pulsar periods. This model also does not suffer from the usual theoretical difficulties such as the return current problem or the required binding energies for the ions and is a theoretically more consistent model.

In spite of this consistency, there is little explanation for the observed pulsar phenomenon such as "subpulse drifting" in this model. It is difficult to reproduce the observed phenomenology of the pulsar radio emission in this model without compromising its consistency, which is its main advantage. Hence, it has been of little use as far as interpretation of observations has been concerned.

1.4 Motivation for the thesis

The individual pulses in pulsars exhibit rich and varied phenomenology, such as "subpulse drifting" and "nulling". These phenomena provide excellent probes for testing models of the pulsar radio emission mechanism, which is not well understood. The subpulse is regarded as one of the basic units of emission and it is supposed to represent the radiation from an isolated location within the distribution of locations covered by the integrated profile. The properties of subpulses thus probe the instantaneous changes in the emitting regions and their study may provide vital clues to the radio emission mechanisms of pulsars.

Because of the relatively short periods of pulsars ($\sim$ 1 s, even milliseconds) and low flux densities ($\sim$ 100 mJy[a] at 408 MHz), the individual pulse shapes and their properties have not so far been studied as extensively as the average properties of pulsars. In particular, it is important to study the relationship between "drifting", "nulling" and "mode-changing" in the same pulsar. This can be done in a handful of pulsars which exhibit all the three phenomena. Very few such studies have been carried out. Moreover, these have often been based on a small number of pulses as it is difficult to obtain extended observation time on telescopes to study a single object.

The prime motivation of this research work was to carry out a study of the kind described above with as large a data set as possible. PSR B0031$-$07 was selected for this purpose as it exhibits all the above mentioned phenomena. Moreover, it was possible to use data consisting of more than 30,000 high sensitivity pulses in this study because of the availability of time on Ooty Radio Telescope (ORT). Finally, this is a unique data set on this pulsar as the only sensitive instrument which can observe this pulsar is ORT.

The results of a study of these high sensitivity data are presented in this research work. A review of the past investigations in the individual pulse phenomena is presented in Chapter 2 alongwith

[a] 1 mJy $= 10^{-29}$ W/m^2/Hz

a brief description of some extensions to pulsar models to explain these. ORT is described briefly in Chapter 3. Data acquisition and reduction procedure is reviewed and the measurements of drift rates for drifting subpulse are also presented in this chapter. Chapter 4 presents the drift dependent properties of drifting subpulses. The relationship between drifting and mode-changing is examined in Chapter 5. The drift independent profiles of subpulse and the competition between subpulse energy is discussed in Chapter 6. The variation of drift rate across the integrated profile is studied in Chapter 7. The interaction between nulling and drifting is discussed in Chapter 8. Finally, the results of this work are summarized and discussed in Chapter 9.

Chapter 2

Drifting, Nulling and Mode-changing phenomena in Pulsars

"Subpulse Drifting" and "Nulling" are well studied individual pulse phenomena exhibited by many pulsars, while "mode-changing" is canonically related to changes in the integrated profile. Since these phenomena are related to changes in the pulsar emission from pulse to pulse, they are useful to characterize its dynamics. In particular, it is important to study the relationship between these phenomena in the same source and only a handful of such studies are available. A brief review of previous studies of these phenomena is presented in this chapter to set the context of this research work followed by a description of the goals of the thesis.

2.1 Subpulse drifting

Drifting was first noticed in PSR B1919+21 and PSR B2016+28 by Drake and Craft (1968). Since then, it has kept evoking interest from different points of view. The phenomenon has been studied from the point of view of classification of pulsar integrated profiles, mode-changing and the radio pulse emission mechanism. Previous observations of the subpulse drift are discussed first in this section followed by the proposed explanations for these observations .

2.1.1 Observations of subpulse drift

In many pulsars, intensity fluctuations are correlated over different phases or longitudes within the integrated profile. These can be detected by a technique based on the spectrum of intensity fluctuations at different longitudes. An analysis of the phase of Fourier components of the spectrum at the frequency of a line feature then reveals drifting of subpulses (Backer 1970c). An

alternative technique involving cross-correlation functions can be employed for many pulsars with weak subpulses, where raw data suggest a weak correlation over longitude. In this method, the intensity fluctuations at a given longitude or phase within the integrated profile for a sequence of periods are cross-correlated with those for a reference phase, which is usually chosen to be the longitude bin corresponding to the peak of the integrated profile. This gives a set of one-dimensional cross-correlation functions for all the longitudes in the integrated profile. These functions describe the average subpulse drift pattern in the longitude-period number lag diagram as a drift band is essentially a correlated subpulse structure across several periods (Proszynski and Wolszczan 1986).

The fluctuation spectrum technique was employed by Backer to study the subpulse drift in a sample of 23 pulsars including PSR B1919+21 and PSR B1237+25 (Backer 1970c; Backer 1970b; Backer 1973; Backer, Rankin and Campbell 1975). These investigations suggested that some form of drifting of subpulses may be occurring in most pulsars. This was termed the "generalized drifting subpulse phenomenon" by Backer (1973), which is explained later on. He claimed that the intensity fluctuations in many pulsars have a periodicity although the phase of the subpulse does not change and cited this as evidence for the "generalized drifting subpulse phenomenon". However, there is no consensus on this issue and it has been claimed that a generalization of drifting to all pulsars cannot readily account for the widely differing fluctuation spectra observed for various pulsars, particularly for the pulsars with a white fluctuation spectrum (Huguenin, Manchester and Taylor 1971). Later, it was shown that drifting is seen in many pulsars, but the phenomenon is generally restricted to the conal components of the integrated profile of these pulsars. Pulsars with a single core component[a] on the other hand invariably showed featureless white fluctuation spectra implying that no drifting takes place in these pulsars. Thus, drifting appears to be a conal phenomenon (Rankin 1986).

Organized drifting is seen in only a handful of pulsars, which exhibit a line feature in their fluctuation spectra. All of these belong to the conal single class of pulsars (Rankin 1986). All such pulsars show a marching of the subpulses across the integrated profile and the drift parameters refer to an association of subpulses across successive individual periods called a drift band. The subpulse drifting is evident by a visual inspection of the data in these pulsars and the drift path can be directly obtained by fitting a suitable curve to the positions of the subpulse in each period. The subpulses appear at the trailing edge of the profile and drift towards the leading edge in more than half of such pulsars.

This subpulse drift can be understood better from diagrams of the type shown in Figure 2.1 where pulse intensity is plotted as a function of time or pulse number (increasing upwards) and phase (or equivalently longitude) in a period for a conal single pulsar (Page 1973). The present day nomenclature, describing drifting in terms of two subsidiary periods P_2 and P_3, is due to Sutton et al. (1970). There are three different periodicities which are associated with a drifting pulsar. The normal pulse periodicity is labeled as P_1 and the separation between the subpulses

[a] "Core" and "cone" components were defined in Chapter 1 Section 1.2

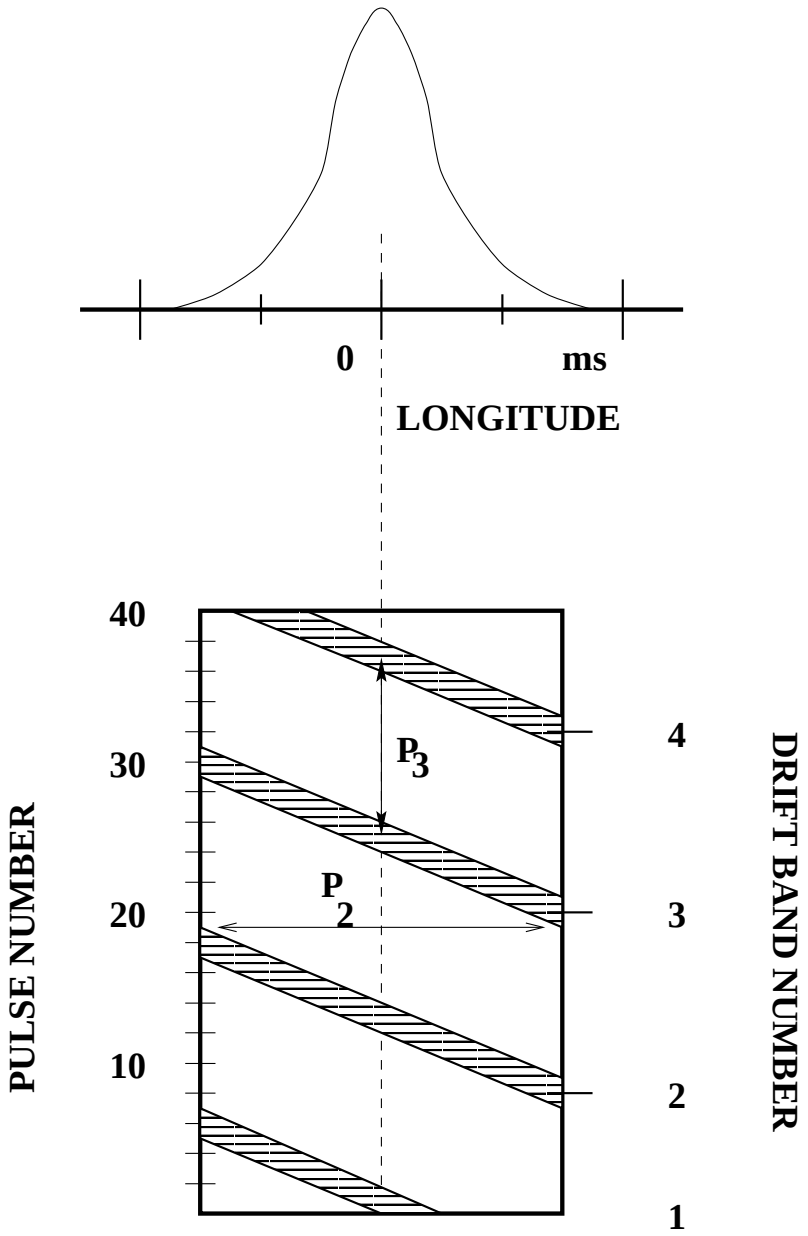

Figure 2.1: Subpulses shown schematically to illustrate the nomenclature described in the text. The subpulse occurs during the hatched part of a period

within a single period is defined as P_2. The third periodicity P_3 is the time between successive appearance of a subpulse at the same phase. P_2 and P_3 are indicated in Figure 2.1. The drift rate, α, is defined as the rate of drift in phase per period, and is given by the ratio of P_2 and P_3.

According to Backer's generalized drifting subpulse scheme, there are three forms of subpulse drifting in pulsars. One is the "linear" drift pattern, in which the subpulses march along a straight line in the longitude-pulse number diagram as in Figure 2.1. The second is the "non-linear" drift pattern where the subpulses march along an approximate S shaped curve in the longitude-pulse number diagram. The last is called the "pattern" form, where the subpulses move along a curve that is not definite in shape, and almost random in nature. However, the pattern of subpulse emission repeats at intervals of P_3.

The pulsars which show more or less "linear" drift with a high periodicity are PSR B0809+74, PSR B0031-07, PSR B0818-13, PSR B2016+28, PSR B0320+39 and PSR B0820+02 (Huguenin, Taylor and Troland 1970; Taylor and Huguenin 1971; Page 1973; Taylor, Manchester and Huguenin 1975; Backer, Rankin and Campbell 1975; Ritchings 1976; Oster, Hilton and Sieber 1977; Izvekova, Kuzmin and Shitov 1982; Lyne and Ashworth 1983). While the first four show drift from the trailing edge to the leading edge, the latter two exhibit drift in the opposite sense. The first two pulsars cited above show the most organized or regular drifting subpulses. PSR B0809+74 has a unique drift rate, whereas PSR B0031-07 exhibits three distinct drift rates. The rest of the pulsars show drifting with varying degrees of regularity. Another pulsar which shows "linear" drift is PSR B1944+17, although its drift pattern is not as regular as that for the pulsars mentioned above (Backer, Rankin and Campbell 1975; Deich et al. 1986). All these stars belong to the conal single class of pulsars in Rankin's classification, which means that the traverse of the line of sight intersects the hollow conal beam of these pulsars tangentially.

Drifting is also inferred in other classes of pulsars, namely pulsars showing the conal double, triple or multiple component profile. In these pulsars, drifting is detected mostly by using the cross-correlation or the fluctuation spectra method described earlier. Prominent members of conal double class of pulsars in which drifting has been detected by these methods are PSR B1919+21, PSR B0525+21 and PSR B1133+16 (Backer 1970b; Backer 1973; Taylor, Manchester and Huguenin 1975; Proszynski and Wolszczan 1986). The drift pattern is "non-linear" in Backer's terminology in these pulsars and the drift bands are not continuous across the integrated profile. Instead, each integrated profile component appears to have its own system of drifting subpulses indicating that the morphology of the integrated profile and the subpulse patterns are correlated (Proszynski and Wolszczan 1986). In some of these pulsars, periodic subpulse modulations appear more as longitude stationery intensity fluctuations unlike the drifts across longitude seen in the "linear" drifters. Hence, the sense of drift in some of these pulsars is ambiguous (Rankin 1986).

Similarly, the triple or multiple profile pulsars show "non-linear" drift associated with one or more components of their integrated profile. Often, such drift is inferred from longitude-stationery fluctuations. In pulsars such as PSR B2319+60 and PSR B1237+25, the drift related modulation

is seen in the outer components of the profile, which are usually classified as conal components (Backer 1970a; Backer 1973; Wright and Fowler 1981a). The central component usually shows a long period fluctuation feature which Rankin claims to be unrelated with drifting (Rankin 1986). Similarly, PSR B1112+50 and PSR B1822-09 show drifting in one component of the profile which can be interpreted as a conal component (Fowler, Wright and Morris 1981; Wright, Sieber and Wolszczan 1986; Gil et al. 1994). The exception to this trend are three triple profile pulsars, namely PSR B1632+24, PSR B1845-01 and PSR B1918+19. While the drifting is associated mostly with the central component of the integrated profile for the former two pulsars, it is seen in the longitudes corresponding to all three components in PSR B1918+19 (Hankins and Wolszczan 1987). These authors claim that all the three components in these pulsars are conal components and the line of sight completely misses the core component, which is absent from the profile. In some of these pulsars, the drift is of the "pattern" form in Backer's nomenclature. Often these pulsars also exhibit mode changes. Such pulsars exhibit drifting subpulses corresponding to the phase of one component in the integrated profile for one mode of the profile, while no modulation or at most a longitude stationery modulation is seen in the other mode (Gil et al. 1994).

There appears to be no preferred direction of drift and pulsars with subpulses marching from the leading edge to trailing edge have also been reported (Rankin 1986), although some of these cases can be questioned on grounds of aliasing. Early observations by Ritchings and Lyne (1975) suggested that pulsars with low spin down in period, $\dot{P}$, show drifting from the trailing edge to the leading edge of the integrated profile. The drift direction is opposite for pulsars with high $\dot{P}$. However, there is no consensus on this issue and Rankin (1986) has argued that this correlation is very weak. A high correlation has , however, been observed between P_3 and the magnetic dipole moment of the star and P_3 increases with increasing dipole moment (Huguenin, Manchester and Taylor 1971; Rankin 1986).

It is rather difficult to make accurate measurements of drift rates in most of these pulsars as these are weak sources. The drift rates are estimated from indirect techniques such as fluctuation spectra and have considerable errors. Moreover, the drift rates vary from one drift band to another in most pulsars and a distribution of drift rates is required to characterize drifting. These determinations require a data set with large number of pulses. Hence, such distributions are available for a handful of pulsars, which exhibit linear drift, such as PSR B0809+74, PSR B1944+17, PSR B0031-07 and PSR B1918+19. Among these, the only extensively studied pulsar is PSR B0809+74. It has a unique drift rate and a power spectrum feature with a Q[b] in excess of 40 (Unwin et al. 1978; Lyne and Ashworth 1983). Most other drifters, however, exhibit more than one value of drift rate. A pulsar with rather complex pulse modulation characteristics is PSR B1944+17 which exhibits bursts of organized drifting interlaced with chaotic subpulse behaviour (Backer, Rankin and Campbell 1975; Deich et al. 1986). Apart from these two pulsars, drift rate distributions based on much smaller data sets have been reported for PSR B0031-07

[b]Q is a measure of spectral purity of a frequency source and is defined as $Q = \frac{f_0}{\Delta f}$

and PSR B1918+19 (Huguenin, Taylor and Troland 1970; Hankins and Wolszczan 1987), both of which appear to show three different drift rates. Thus, there is a need to measure the drift rate distributions for these pulsars more accurately.

Subpulses from two adjacent bands are often found in a given individual period in pulsars, which exhibit highly organized drift (Sutton et al. 1970; Huguenin, Taylor and Troland 1970). The properties of these subpulses as a function of drift rate have not been reported before to the best of our knowledge and such studies are required to constrain the pulsar emission mechanism. A given drift band is linear to a first order in these pulsars, although a variation in the drift rate with longitude has been reported (Backer 1973; Krishnamohan 1980; Proszynski and Wolszczan 1986). A variation of the order of 20 percent in drift rate across the profile is usually seen (Lyne and Graham-Smith 1990). Such studies can be useful in constraining the geometry of emission beams. Subpulse drift rates have been observed to be independent of frequency of observation (Wolszczan, Bartel and Sieber 1981; Nowakowski et al. 1981) suggesting that these are intimately related to the physics of polar cap.

There is some evidence that drifting and pulse nulling may be related phenomena. A disturbance of the subpulse drifting at nulls was first noted for PSR B0809+74 by Cole (1970). Subsequent studies have indicated that there is a sudden change in the drift rate at the onset of pulse null followed by a relaxation of drift rate in this pulsar (Unwin et al. 1978; Lyne and Ashworth 1983). On the other hand, no phase correlation across nulls was observed for PSR B1944+17 (Deich et al. 1986). Thus, there is no consensus on this issue and this interaction needs to be studied in other pulsars for a better understanding.

2.1.2 Origin of subpulse drift

Although drifting was generally explained by invoking some kind of circulating disturbance around the neutron star or in the polar cap, the first specific model was proposed by Ruderman and Sutherland (1975). The origin of drifting is explained in this currently popular model by invoking $\mathbf{E} \times \mathbf{B}$ drift of sparks (or bursts of charges) in the vacuum gap above the pulsar polar cap. It is believed that the coherent radio emission, which is locked to these sparks, follows the drifting of sparks (Ruderman and Sutherland 1975). This model was discussed in Section 1.3.4 and an elaboration of this model on the origin of drift is presented below.

When a discharge begins at some point on the polar cap, the $\mathbf{E} \cdot \mathbf{B}$ that has built up across the gap rapidly falls at this point and its neighbourhood. This is expected to inhibit another simultaneous discharge within a distance comparable to gap height $\sim h$. Thus, the vacuum gap discharges through a group of localized sparks in this model. The magnetosphere above the gap does not corotate with the star as long as the charge density in the gap is zero as was noted before. Hence, the sparks in the gap exhibit a motion with respect to the stellar surface. Ruderman and Sutherland (1975) showed that the average drift velocity of the sparks around the magnetic poles

is given by

$$\Delta v = \frac{\Delta V}{B_{12} r_p} c \tag{2.1}$$

where ΔV is the gap potential, r_p is the polar cap radius and B_{12} is the surface magnetic field. The time (P_3) for a spark to make a complete rotation around the magnetic pole is then given by

$$\frac{P_3}{P} \approx 5.6 B_{12} P^{-2} \approx 1.8 \times 10^{20} \dot{P}^{\frac{1}{2}} P^{-\frac{3}{2}} \tag{2.2}$$

where P is the period of pulsar in seconds, $\dot{P}$ is the period derivative and B_{12} is the magnetic field in units of 10^{12} G.

These sparks inject energetic positron beams in the magnetosphere above the gap, which get bunched due to a plasma instability. The radio emission is then produced by the coherent curvature radiation of bunches. Thus, the position of the emission regions on the polar cap is determined by the underlying spark and the subpulses are expected to exhibit a similar drift.

Although the details of the drifting phenomenon were not derived, the model does give an estimate of P_3 (Equation 2.2) in terms of P_1 and $\dot{P}_1$ and the agreement with observations is remarkable for the small sample of consistent drifters (Wolszczan 1986; Wright and Fowler 1981a). This has been a great success for this model, although it has been criticized on various theoretical grounds. Drifting is explained in a very qualitative fashion in the competing models by either invoking a disturbance drifting around the pulsar at the velocity of light cylinder with a velocity smaller than the corotation velocity or a low frequency transverse wave (Arons 1981b). It is difficult in these models to relate the drift parameters to the physics of the emitting region. Thus, the Ruderman and Sutherland model is the only model with a viable explanation for the subpulse drift.

This model implies a full series of well separated subpulses outside the pulse window (Curtis Michel 1991). The sparks are separated by a distance of the order of gap height which is also related to its drift speed in this model. This suggests that the subpulse separation increases with drift rate, although this observational implication has not been stated explicitly either in this model or its subsequent modifications and a new study to test this is required. This model also implies that the emission regions drift inside a hollow cone. Since, the observer's line of sight intersects this trajectory tangentially, the drift rate is supposed to be enhanced at the edges of the integrated profile (Oster, Hilton and Sieber 1977; Wright 1981) and this can also be tested observationally. These issues are addressed in this thesis.

2.2 Pulse Nulling

In some pulsars such as PSR B1237+25 and PSR B1133+16, no pulse emission is observed for several pulses. This phenomenon was first reported by Backer (1970c) and has since been seen in several pulsars (Ritchings 1976; Rankin 1986; Biggs 1992; Vivekanand 1995). The pulse energy abruptly decreases by a factor of more than hundred for several pulses in these pulsars. Hence,

it must represent the failure of some essential characteristics of pulsar radio emission and is an important probe for the pulse emission mechanism. First, observations of this phenomenon are presented in this section. Then, three qualitative models for pulse nulling are discussed.

2.2.1 Observations of pulse nulling

Backer (1970c) studied four pulsars, namely PSR B0834+06, PSR B1133+16, PSR B1237+25 and PSR B1929+10 and reported two different types of nulls in these pulsars. Nulls with a duration between three to ten pulses were termed Type I by him. Such nulls repeat with a spacing of about 50 pulses. On the other hand, Type II nulls occur frequently (with a spacing of three to ten pulses) and generally have one or two pulses only. A weak feature in the spectrum of nulling pattern in PSR B1929+10 was also reported indicating some kind of quasi-periodicity in the nulling pattern. Subsequently, nulling was also reported in PSR B0031-07 (Huguenin, Taylor and Troland 1970), PSR B0809+74 (Page 1973), PSR B1944+17, PSR B0950+08, PSR B0525+21 and PSR B0823+26 (Hesse and Wielebinski 1974).

It is difficult to detect nulling in some of these pulsars as they are weak. Therefore, nulling is often deduced by carrying out a statistical analysis on single pulse intensity measurements as explained below. First, the energy in a window, defined by those samples of the integrated profile in which the signal from the pulsar is received, is measured for each single period. This window is called the on-pulse window. A similar measurement is carried out for an off-pulse window[c]. The energy in the off-pulse window represents the system noise or the minimum detectable power. A histogram of both on-pulse and off-pulse measurements is then obtained. In general, on-pulse histogram has two components - a zero energy component and a component centered at the mean energy of single pulses. Since the nulled pulses contribute system noise only, an excess of zero energy pulses in the on-pulse histogram implies nulling (Hesse and Wielebinski 1974). The percentage of such zero energy pulses in this histogram gives an estimate of the fraction of pulses for which a pulsar nulls and is called the nulling fraction. If the two components are well separated, a lower limit for the nulling fraction can be determined. Otherwise, these histograms provide an upper limit (Ritchings 1976). Recently, an improved method, in which the energies in the on-pulse and off-pulse windows are estimated using two or three extreme values, has been proposed. This method is particularly suitable for drifting pulsars (Vivekanand 1995).

Nulling has been reported in more than 80 pulsars using these techniques. Nulling fractions range from a fraction of percent to more than 70 percent (Rankin 1986). Many pulsars have very small nulling fractions (of the order of 0.05 percent) and it can be concluded that such pulsars do not null. When nulling is examined from the point of view of morphology of the integrated profile, it appears that conal single pulsars have a smaller nulling fraction as compared to conal double, triple or multiple component profile pulsars. However, there are pulsars in each of these classes

[c]This is a window of width equal to the on-pulse window, but located well away from the on-pulse region of the integrated profile

which do not null (Rankin 1986). Although Rankin (1986) showed that core single pulsars do not null, a later study reports five such pulsars where nulled pulses have been observed (Biggs 1992).

Earlier studies indicated that old pulsars have a higher fraction of null pulses than younger pulsars (Ritchings 1976). A subsequent analysis of available pulsar nulling statistics suggested that stars with conal single or double profiles and with triple and multiple profiles can be one to three orders of magnitude older than those with core single profile. Since the former class of stars have a larger null fraction, there appears to be a correlation between the nulling fraction and the age of the pulsar (Rankin 1986). However, Biggs (1992) claims that the discovery of significant nulling in five southern core single pulsars weakens this argument. In summary, it is yet not clear if pulsars "die" by increasing their nulling fraction as they age.

Null durations can range from a single pulse to several hundred pulses. Most pulsars exhibit type II nulls which are one to three pulses long. In addition, a whole range of null durations are observed in pulsars such as PSR B0031-07 and PSR B1944+17. Typically, the radio emission from pulsars decreases by two orders of magnitude during a null. This factor has been estimated as ~ 100 for PSR B1944+17 (Deich et al. 1986) and for PSR B0031-07 (Vivekanand 1995). The mean energy in null state is estimated as -0.23 ± 0.43 per cent for PSR B0809+74 (Lyne and Ashworth 1983). Now, nulling could be due to a loss of coherence of the radio emission mechanism. Hence, this limit on the radio emission during a null has significant implication for the emission mechanisms and it needs to be determined more accurately from high sensitivity data.

2.2.2 Models for pulse nulling

Few qualitative explanations for this phenomenon have been suggested as the pulsar models have not evolved sufficiently to explain the observations cited above and fundamental theoretical work is needed. Three likely explanation proposed in the literature are briefly discussed below.

No explicit explanation for nulling was proposed in Ruderman and Sutherland (1975) model and its subsequent modifications. Qualitatively, nulling could be explained by invoking either a total cessation of pair production or a loss of coherence of the radiation mechanism within this framework. A model for the burst-null-burst transition using the former hypothesis was developed by (Jones 1983). In this model, the backward flow of relativistic electron in a Sturrock discharge, similar to Ruderman and Sutherland (1975) model, heats the polar cap surface. This decreases the mean surface nuclear charge by driving an ion current from the surface which produces photoelectrons by interacting with the background black-body radiation field. The ion current and photoelectrons soon dominate the current flow in the gap and the gap potential falls below the pair-production threshold. No positron beam is injected in the upper magnetosphere and the star enters a null state. In the null state, as the mean surface nuclear charge grows, the ion emission decreases and the gap potential rises. Eventually, pair production resumes and a transition to burst state takes place. However, it is difficult to test this model against observations as no details regarding the range of null durations have been suggested.

An extension of the Ruderman and Sutherland model was proposed by Filippenko and Radhakrishnan (1982) to explain the phase memory in PSR B0809+74. This model also attempts to give a qualitative explanation for nulling. In this model, the discharges occur in localized flux tubes which are regions with higher $E_{\parallel}$. These tubes drift in a manner similar to Ruderman and Sutherland (1975) sparks. Normally, the potential in each tube rises exponentially till it is discharged by the onset of a spark. The discharge, which lasts for about 10^{-6} s, is eventually terminated when the gap potential falls below the threshold for pair production. However, the outflow of charged particles from the tube continues and a gap is formed again. Then, the process repeats again and the discharge in this mode is a continuously interrupted discharge rather than the quasi-steady Ruderman and Sutherland (1975) discharge. These authors claim that this interrupted discharge leads automatically to bunching of the secondary plasma. These bunches are supposed to give the observed radio emission. During a null, the gap height adjusts itself in such a manner that there is a steady discharge in the flux tube. In this manner, the bunch formation is inhibited and the efficiency of radio emission declines drastically leading to a null. The steady discharge also reduces the gap potential and consequently the drift velocity of flux tubes substantially, which can explain the phase memory phenomenon.

A significantly different approach is to assume that the parallel electric field extracts particles from the stellar surface and these form a primary beam (Sturrock 1971; Arons 1981b). These particles are accelerated to high Lorentz factors and generate a secondary pair plasma with much smaller Lorentz factors. Interaction of these two beams gives rise to a plasma instability which is responsible for radio radiation. In the burst state, the primary beam distribution is narrow. However, the positrons produced in the pair cascade are accelerated towards the stellar surface and heat it. This broadens the primary beam distribution as well as reduces the potential in the acceleration zone. Thus, the peak of the primary beam moves towards low Lorentz factors and the instability leading to radio radiation is quenched. As a result, a null is observed (Kazbegi et al. 1996).

The studies of nulling fractions mentioned earlier do not provide sufficient constraints to discriminate between these qualitative explanations. On the other hand, investigations of periodicities in the nulling pattern and null-drift interaction provide better constraints, which will motivate further development of these models. An attempt is carried out in this direction in this research work.

2.3 Mode-changing

Mode-changing was first noticed in PSR B1237+25 by Backer (1970b). He reported that the pulse emission of this pulsar changes characteristically for several pulses. The integrated profile for these pulses differs significantly from the usual profile of the pulsar. A similar phenomenon was reported in PSR B0329+54 by Lyne (1971) and is observed in several other pulsars now. A brief discussion

this phenomenon and its proposed explanations is given in this section.

2.3.1 Observations of mode-changing

Mode-changing is readily observed in pulsars with complex profiles such as PSR B1237+25 and B0329+54, which have three or more components. Most of these pulsars normally exhibit an integrated profile which is symmetrical about its central component. This mode is usually called the "normal" mode of the pulsar. On the other hand, these pulsars show a remarkably asymmetrical integrated profile in the so called "abnormal" mode. The exceptions to this nomenclature is PSR B0355+54 and PSR B1737+13, which exhibits an asymmetrical profile in its "normal" mode. In some of these stars, successive averages of a few hundred pulses have widely different forms indicating several discrete modes (Rankin 1986).

Detailed studies of this phenomenon have been carried out for two pulsars, PSR B1237+25 and PSR B0329+54. Simultaneous two frequency observations of these pulsars indicate that the switch between two modes is broad band as it occurs simultaneously at the two frequencies. The abnormal mode pulse profiles are strikingly more frequency dependent than the normal profiles indicating that the spectral index of different components changes during a switch (Bartel et al. 1982). The polarization angle curve as well as the circular polarization's sense reversal signature is broadly the same for the two modes. However, the details of the polarization behaviour in two modes are different indicating a possible shift of emission regions relative to the trajectory of line of sight (Lyne 1971; Bartel et al. 1982; Rankin 1986). The mode changes in both these pulsars are accompanied by changes in their fluctuation spectrum.

Apart from the above two well studied pulsars, mode changing has been reported in several other stars. The other multiple component pulsar with similar properties is PSR B1737+13. A characteristic fluctuation pattern is observed in the normal mode of this pulsar, whereas it is absent in the abnormal mode (Rankin, Wolszczan and Stinebring 1988). There are several examples of pulsars with triple profile, which show mode-changes. In PSR B1926+18, the intensity of the central component increases by a factor of eight in the abnormal mode as compared to the normal mode. The overall intensity of pulsar is also larger in the abnormal mode. At the same time, the separation between the peaks of the outer components reduces in the abnormal mode (Ferguson et al. 1981).

Two interesting pulsars exhibiting mode-changing are PSR B1822-09 and PSR B1055-52. Both these pulsars show an interpulse[d] and are good candidates for studying the correlation between the main pulse and the interpulse. PSR B1822-09 has two distinct forms of the integrated profile. The main pulse has two components (C1 and C2) in the B mode, where the interpulse is either weak or absent. In contrast, a strong interpulse is present in Q mode, where C1 component is absent. Thus, intensity in C1 component and interpulse appear to be anti-correlated (Fowler, Wright and

[d]Some pulsars exhibit an integrated profile with two narrow components separated typically by 180 degrees. The stronger component is usually labelled as main pulse, while the weaker component is called interpulse

Morris 1981; Morris, Graham and Bartel 1981; Fowler and Wright 1982; Gil et al. 1994). On the other hand, a correlation between the intensity of main pulse and interpulse is indicated by the observations of PSR B1055-52 (Biggs 1990).

The changes in the integrated profile in some mode-changing pulsars depend upon their single pulse behaviour. For instance, PSR B2319+60, which has a three component integrated profile, is believed to exhibit three drift rates and the integrated profile for each mode is associated with a different drift rate (Wright and Fowler 1981a). Other pulsars discussed above also exhibit distinct changes in the fluctuation spectrum for different modes. PSR B2319+60 motivates investigation of mode-changing in pulsars which exhibit distinct drift rates such as PSR B0031-07, but show a single component and usually stable integrated profile. Such a behaviour has been indicated in PSR B0031−07 (Wright and Fowler 1981b). Unfortunately, a detailed analysis of this pulsar was not been reported by these authors and such a study is useful.

2.3.2 Proposed explanations for mode-changing

No explanation for mode-changing has been proposed, although it is conjectured that a mode change involves a redistribution of the excitation over several components (Lyne and Graham-Smith 1990). The polarization properties indicate a possible shift of the emission regions with respect to the magnetic axis of the pulsar. In this context, an interesting possibility involving a change in the emission altitude was suggested by Nowakowski (1994). A connection between mode-changing and drifting further suggests that abrupt changes in the gap properties may be related to profile changes. Recently, a model suggesting three alternative mechanisms or modes for the pulsar inner gap breakdown has been proposed. In this model, the pair cascade in the inner gap proposed by Ruderman and Sutherland (1975) can be triggered by one of the following mechanisms - (1) curvature radiation photons, (2) photons upscattered by inverse Compton scattering at a resonant frequency where the cross section for this process is largest, and (3) upscattered photons corresponding to the thermal peak of the background black body radiation. One of these mechanism will dominate the gap break down depending on the surface temperature of the star and eventually determine gap properties such as gap height h or the gap potential. It is suggested that the gap operates in more than one mode for the mode-changing pulsars, leading to a reorganization of radio emission regions (Zhang et al. 1997).

Thus, it can be seen that the dynamics of pulsar emission is clearly involved in mode-changing phenomenon. It has been historically associated with dramatic changes in the multi - component integrated profiles as these are easier to detect. But, such changes are invariably accompanied by changes in the individual pulse behaviour as described above. Thus, it is likely that subpulse behaviour is more fundamental and the profile changes a mere manifestation of these as suggested by Wright and Fowler (1981a). Hence, a study of profile changes as a function of drift rate can provide useful information on the nature of this phenomena.

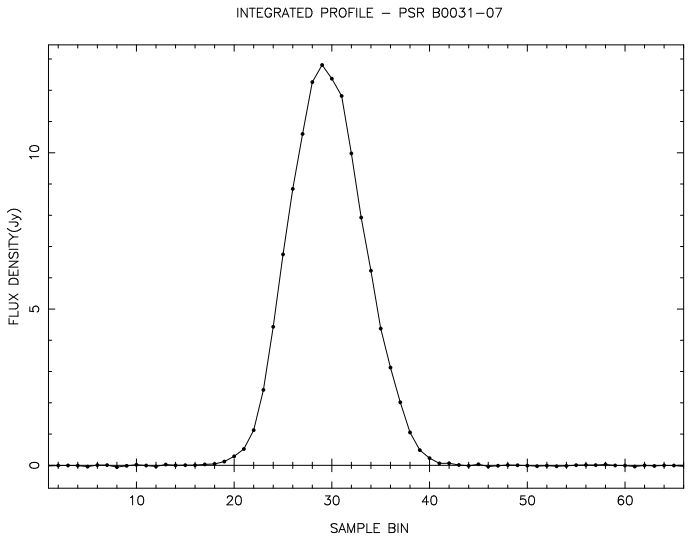

Figure 2.2: Integrated Profile of PSR B0031-07 for March12,1996 observations

Period	$\dot{P}$	DM	S_{400}	log τ_s	log B
				$\tau_s =$	$B =$
				$\frac{1}{2}P/\dot{P}$	$(3.2 \cdot 10^{19} \cdot)$
	(10^{-15})				$(P\dot{P})^{1/2}$
(s)	(s/s)	$(cm^{-3}pc)$	(mJy)	(s)	(G)
0.942950785	0.4083	10.89	52	7.56	11.80

Table 2.1: Summary of observed and derived properties of PSR B0031-07 (Goldstein and James 1969; Manchester and Taylor 1981; Lorimer et al. 1995)

2.4 PSR B0031-07

The pulsar PSR B0031-07 is a unique pulsar known for its beautiful **harmonic** drift and long nulls. It is the only other known pulsar which exhibits well organized drifting, the most organized one occurring in PSR B0809+74 among the known drifting pulsars. The salient features of radio emission from this pulsar and a review of its earlier observations is described in this section.

PSR B0031-07 has a period of 0.942 s and a mean flux of $\approx$ 100 mJy at 326.5 MHz. Some observed and derived properties of this pulsar are summarized in Table 2.1. It has a smooth integrated profile at this frequency with a width[e] of approximately 130 ms as shown in Figure 2.2. A typical pulse has two well separated peaks of emission or subpulses (Figure 2.3) and these subpulses drift from the trailing edge of the profile to the leading edge. The separation P_2 between two subpulses varies with frequency as $\nu^{-0.25}$ (Taylor, Manchester and Huguenin 1975). The pulsar has a large characteristic age and low magnetic dipole moment(Table 2.1).

[e]The width of profile is defined as the phase interval between the points on the profile where the profile intensity is 10 % of the peak intensity

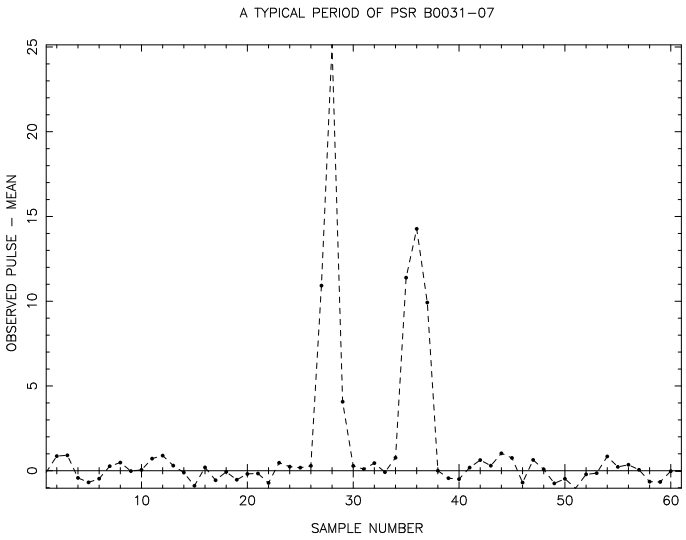

Figure 2.3: Typical Subpulses in an individual period of PSR B0031-07. "MEAN" is the average energy in the off pulse samples.)

The drifting in PSR B0031-07 was first reported by (Sutton et al. 1970). The drift rate within a band is usually constant to a zero order though it varies from band to band. Measurements of drift rate were made for 150 drift bands ($\approx$ 3000 individual pulses) by Huguenin, Taylor and Troland (1970). They claimed that the drifting behaviour assumes one of three distinct states and they called these as classes A, B and C. The characteristics of these three classes as reported by them are reproduced in Table 2.2. They found that the Class C and Class B modes occur in a single burst. Accordingly, the frequency of occurrence of class C mode is quoted by them as a percentage of total class B bursts. The mean drift rates for these classes appear to be integral multiple of the drift rate for class A. Although other investigators have observed this pulsar, these are the only estimates quoted in the literature for PSR B0031-07 till the present work.

The drift bands were observed to be in phase over at least the frequency range of 275-430 MHz when simultaneous observations at several frequencies were made (Taylor, Manchester and Huguenin 1975). The drift rate is also seen to be independent of frequency of observation (Backer, Rankin and Campbell 1975; Izvekova et al. 1993). The drift rate is, however, seen to vary with longitude (Krishnamohan 1980). The individual pulses corresponding to different drift rates add upto different integrated profiles (Wright and Fowler 1981b).

The intensities of the subpulses vary from pulse to pulse. The pulsar is typically inactive for 10 to some hundred periods and then emits a burst of similar number of periods (Huguenin, Taylor and Troland 1970). It exhibits nulling for 44.6 ± 1.3 per cent of time and both short as well as long nulls are observed. The distribution of null lengths indicates two population of nulls, which correspond to Type I and II nulls in the Backer's nomenclature (Vivekanand 1995).

Thus, this pulsar presents a good opportunity to study the subpulse properties as a function of drift rate and to explore the relationship between the drifting, nulling and mode-changing

Class	Drift Rate α	P_3	Relative frequency of Occurrence
A	4.5 ± 0.4	12.5 ± 0.5	20 %
B	8.5 ± 1.5	6.8 ± 0.8	80 %
C	14 ± 3	4.0 ± 0.5	5 % of B

Table 2.2: Table 1 of Huguenin, Taylor and Troland (1970) giving characteristics of three drift modes

phenomena, which were the main objectives of this thesis.

2.5 Objectives of the thesis

The three pulsar phenomena, namely "drifting", "nulling" and "mode-changing", provide important probes for the study of pulsar emission mechanism. The main objective of this research work was to study these phenomena and their relationship with each other in a pulsar which exhibits all these phenomena. Such a study is necessary not only to provide constraints for the existing models, but also to motivate the development of these models.

Very few pulsars exhibit organized drifting and significant nulling. In most pulsars, drifting is sporadic (PSR B1944+17), variable (PSR2016+28) or across small portions of the integrated profile as in PSR B1237+25, PSR B1919+21 and PSR B1632+24 (Rankin 1986; Proszynski and Wolszczan 1986; Hankins and Wolszczan 1987). A much smaller subset of these drifters exhibit significant nulling. Among these, the organized drifting is exhibited by barely two pulsars - PSR B0809+74 and PSR B0031-07. As mentioned before, pulsars are weak radio sources and a sensitive instrument is required for an individual pulse study. Several hours of observing time, required for the kind of analysis reported in this thesis, was available to us at Ooty Radio Telescope, or ORT (Swarup et al. 1971). PSR B0809+74 is unfortunately not observable with ORT because its limit of declination ($\approx \pm 55°$) is smaller than the declination of this pulsar ($+74°$). On the other hand, the only instrument available for high sensitivity observations of PSR B0031-07 is ORT as the declination of this pulsar is -7 degrees. Therefore, this thesis concerns with the individual pulse properties of the only other systematic drifting pulsar PSR B0031-07.

Although the subpulse drift has been studied in many pulsars, quantitative distributions of drift rates are available for only a few pulsars as mentioned in Section 2.1. This requires the measurements of drift rates for a large number of drift bands. The number of drift bands for PSR B0031-07 in the data available to us was larger by a factor of ten than any previous study. Hence, a more accurate distribution of drift rates for this pulsar was obtained and presented for the first time in this thesis.

In Ruderman and Sutherland model, the drift velocity of the sparks, believed to be responsible for the observed subpulses, depends on the properties of the vacuum gap. Thus, it is expected that

changes in the gap configuration will also affect the properties of the subpulses. Observationally, this can be examined by studying properties of subpulse as a function of drift rate. No quantitative study of the subpulse properties as a function of drift rate has been reported to the best of our knowledge. In particular, the variation of the average subpulse separation with drift rate needs to be studied as mentioned in Section 2.1. Hence, the second objective of this research work was to investigate this issue in detail.

Ruderman and Sutherland model implies a number of localized sparks. In a dynamical situation, the adjacent sparks will influence each other. This in turn have observational consequences for the adjacent subpulses. This is best done by studying a pair of drifting subpulse after removing the drift, which was estimated earlier for each drift band. No such study has been reported earlier in the literature. Hence, the third goal of this thesis was to present such a study of the drift independent properties of a pair of drifting subpulses.

Wright and Fowler (1981b) note a connection between drifting and mode changing in PSR B0031-07, but no figure is shown to substantiate this claim. As a large number of pulses on this pulsar were available to us, integrated profiles for the three drift modes could be obtained. Such profiles are presented for the first time for a conal single pulsar. The suggestion by Wright and Fowler (1981a) that the single pulse behaviour is more fundamental is examined in the context of these profiles.

Although the drift bands in PSR B0031-07 are linear to a first order, a variation in the drift rate with subpulse position has been reported (Krishnamohan 1980). However, high sensitivity data is required to study the variation at the edges of the integrated profile, which is expected in the hollow cone geometry of Ruderman and Sutherland (1975) model. This has been investigated for PSR B0031-07 in this thesis.

It was mentioned in Section 2.1 that there is no consensus on the existence of phase memory or correlation across nulls although a disturbance of the subpulse drifting at nulls has been noticed in many pulsars. An interaction between drifting and nulling in PSR B0031-07 has been often referred in the literature during discussions on nulling and drifting in other pulsars (Page 1973; Wright and Fowler 1981a), but no study has ever been reported. Such a study is essential in the absence of consensus on the phase memory based on studies of two pulsars only. Hence, this was one of the main goals of the present research work.

Thus, this work was carried out with two main scientific objectives - (1) to verify the implications of Ruderman and Sutherland model cited above by studying the subpulse properties both as a function of drift rate as well as after removing the drift in a systematic drifting pulsar, (2) to study the connection between drifting and mode-changing and the interaction between nulling and drifting phenomenon by studying the phase correlation and drifting across nulls in the same pulsar. The main thrust of the work is to understand the inter-relationship between the three phenomena mentioned earlier and to provide observational constraints to motivate further development of theoretical models.

Chapter 3

Observations of PSR B0031-07 and data reduction

The observations for this thesis were carried out using the Ooty Radio Telescope (ORT). This unique facility at equatorial latitudes (Swarup et al. 1971) has become a highly sensitive instrument for pulsar studies with the recent upgrade of its feed system (Selvanayagam et al. 1993). Here, a brief description of ORT and the data acquisition system is presented. The acquired data was reduced using a set of programs which is discussed briefly. Finally, a distribution of drift rates for PSR B0031−07 is presented followed by a discussion on quasi-periodicity in the nulling pattern of this pulsar.

3.1 The Ooty Radio Telescope

Located at an altitude of 2150 m in the Nilgiri hills in South India (latitude of $+11°23'$ and longitude of $76°40'$ E), ORT is a 530 m long and 30 m wide parabolic cylindrical antenna (Figure 3.1). The effective collecting area of the telescope is approximately 7100 m^2. The antenna consists of 24 parabolic frames spaced 23 m apart. The reflecting surface consists of 1100 thin stainless steel wires spread over the 24 frames. The signals are received by 1056 dipoles placed along the focal line on a feed truss. ORT is erected on a north-south mountain slope with an inclination of $11°23'$ with its long axis in the north-south direction. This makes it an equatorially mounted antenna with its long axis parallel to the earth's rotation axis. The declination of a source is set by suitably phasing the dipole array while the source is tracked in hour angle by rotating the antenna around its long axis. Sources with declination ranging from $-55°$ to $+55°$ can be observed using the telescope. A source can be tracked from 4 h 05 m East to 5 h 30 m West although for high sensitivity work a range of 3 h 40 m E to 4 h 30 m W is recommended.

The operating frequency of the telescope is 326.5 MHz with a bandwidth of 9 MHz. As the axis of the feed dipoles is aligned in the north-south direction, the signal at the feed output is

Figure 3.1: Ootucumund Radio Telescope

proportional to north-south component of the electric field vector, or a single polarization of the radiation received by the telescope. The dipoles are arranged into 22 groups called MODULES, which are further subgrouped into two halves called north and south halves. This division is useful to operate the entire phased antenna in a mode where the signal from the north half is correlated with that from the south half thereby eliminating any uncorrelated noise in each half.

A block diagram of the receiver electronics is as shown in Figure 3.2. A low noise radio-frequency (RF) amplifier is used to amplify each module output which is then down-converted to an intermediate frequency (IF) of 30 MHz. The signal is then suitably amplified and phased to the correct declination. The phased signals of each half of ORT are combined together to form 12 beams in declination. Beam 7 of ORT was used for the PSR B0031-07 observations described in this thesis. The IF output is filtered and converted to the baseband by mixing with a second local oscillator (LO) of 35.3 MHz frequency suitably adjusted to get a good passband. The baseband signal is processed and acquired using one of the four different backends in use with ORT. The digital correlator was used as the backend for these observations.

The 512-channel digital correlator, designed by Dr. R. Subrahmanyan, is an XF type of correlator (in which the correlation is done first, followed by a Fourier transform) with a personal computer (PC) interface for data acquisition. The baseband signals from each half of ORT are sampled at 18.432 MHz and then converted to 1-bit digital signals, where 1 implies signal values above the 0.0 volts, and 0 implies voltages below this value. The signals from the north and south halves of ORT are then multiplied with each other after introducing 64 fixed delays between them. In this way, 32 leads and 32 lags are generated which are equivalent to 32 frequency channels after taking a Fourier transform. Thus, the correlator is equivalent to a 32 channel digital spectrometer. These correlations are integrated in the correlator for a duration fixed by the user, which becomes

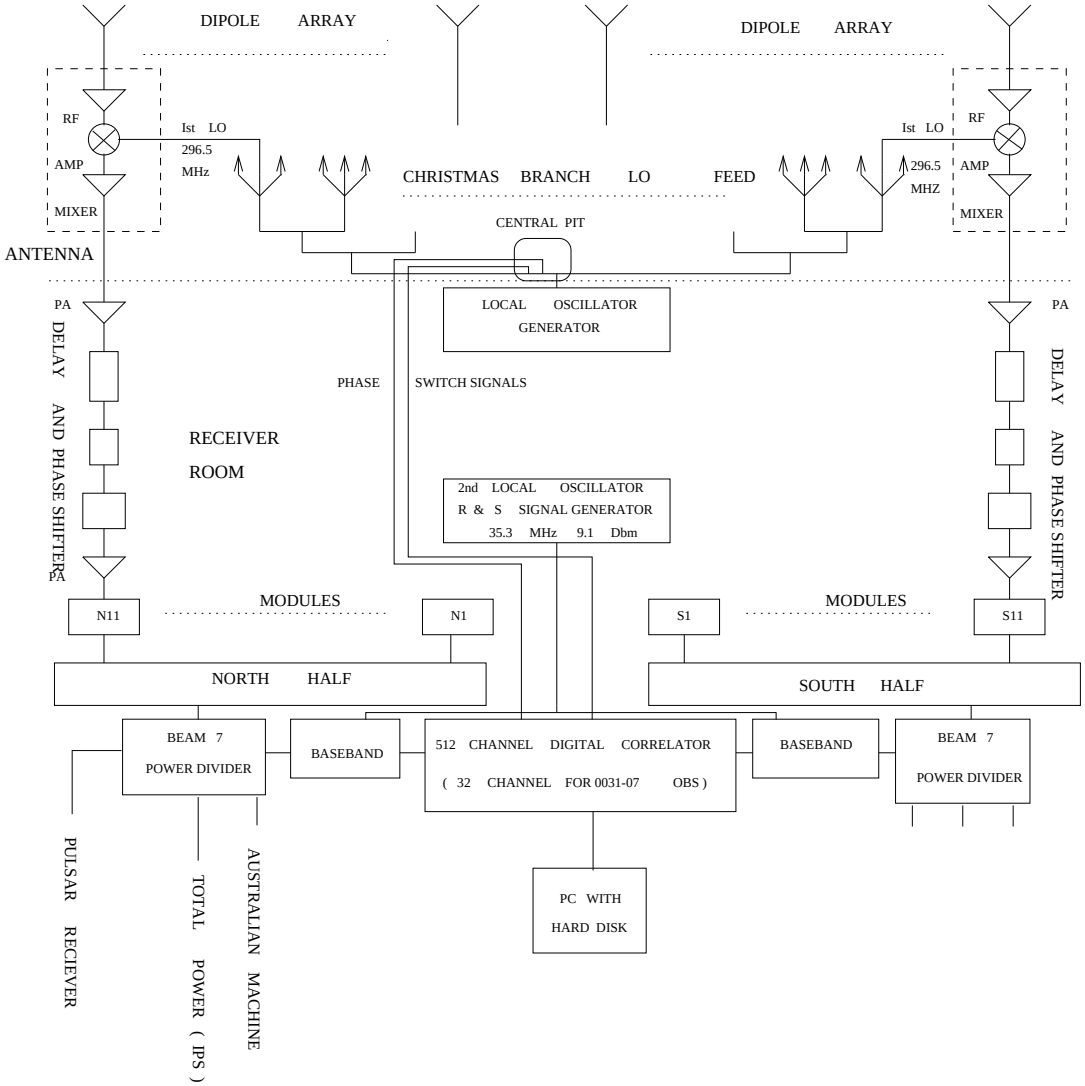

Figure 3.2: Block Diagram of the receiver electronics of ORT

the effective sampling interval for the observations (typically 5 to 10 ms). The correlations and a count of the total number of clock cycles are read via an interface card by a program running on the control PC. The correlation coefficients are read once every integration time which is determined by an interrupt pulse generated every 0.1 ms by a GPS clock in the receiver room. Diagnostic square wave signals can be generated and fed to the sampler internally in the correlator instead of the baseband outputs by pressing a test switch. The health of the system can be quickly checked using this facility. The reader is referred to Subrahmanyan (1989) for details.

Spurious correlation coefficients are introduced due to leakage of signal power from one half of ORT to the other as well as due to the sampler offsets. A phase switching scheme was used to eliminate these spurious correlation coefficients. Two orthogonal functions - square waves of 5 MHz and 10 MHz - were generated in the clock generation logic of the correlator and used to modulate the first LO. The baseband signal was synchronously demodulated at the sampler eliminating any coupled signal.

A set of test display and acquisition programs was used to operate the correlator and to acquire the data. The test display program displays the correlation coefficients as well as their power spectrum. This program is useful for a quick on-line evaluation of the entire system before the commencement of the actual observations. The correlator is initialized and data samples are acquired using the main acquisition program which uses the parameters set in a receiver configuration file. First the pulsar is observed in the monitor mode of this program where the integrated profile is continuously displayed. Then, a gated window is set around the part of the profile where pulse emission is seen. The window bin numbers are interactively entered from the keyboard and the data acquisition is begun. The acquired data is written to the hard disk of the PC.

3.2 The Data Acquisition

The performance of the instrument was checked using the test program with the correlator in test mode. A square wave input is fed to the correlator in this mode and hence, the correlation function is expected to have a triangular form. Then , a few samples were acquired using this program while the telescope was tracking a calibrator radio source. The power spectrum displayed in this mode was inspected to make sure that the pass band of the instrument is reasonably uniform and is free of any major sources of interference. Sometimes, interference was strong and the observations had to be postponed. In addition, the total power from the telescope was monitored on a chart record. Sometimes, severe ionospheric scintillation occurred causing the total power to fluctuate significantly during an observing session and such data were rejected.

Once good observing conditions were ensured, a calibrator source located in a direction close to that of the pulsar was observed and typically 1000 to 2000 data samples (τ[a] typically 5 to 10

[a] τ is the sampling period

ms) were acquired. These data were later used to calibrate the pulsar flux and to get an idea of the sensitivity of the telescope at the time of observations. It was observed that sometimes the phasing of ORT modules was not proper resulting in a fall in sensitivity. Whenever this occurred, the module phasing was carried out afresh. The calibrator used most often was 3C17 which is almost at the same declination as PSR B0031-07.

The pulsar was then observed by using the acquisition program in the monitor mode. The pulsar flux at an observing frequency varies due to interstellar scintillation. Data were acquired only when the pulsar flux was seen enhanced. Typically, data could be acquired only during 50 percent of the observing time scheduled. A total of 44,404 individual periods were retained from a much larger data set obtained from ORT. The calibration of the data and analysis are described in the next section.

3.3 The Data Calibration and Reduction

The data were processed in three phases. First, the sensitivity of the data was enhanced using the dynamic spectra[b] of the pulsar. Then, the null and burst periods were identified. The subpulses in an individual period were replaced with equivalent Gaussians in the third phase of the analysis and the positions of the Gaussians were used to identify the drift bands. Finally, the drift rates for these bands were estimated. A brief description of the procedure of analysis is presented below.

3.3.1 The Data Calibration

The calibrated flux density (in Jy), in a sampling interval of $\approx$ 5 ms in the 32 frequency channels that span ORT's bandwidth of 9 MHz, was estimated from the raw correlations. The correlations acquired on a calibration source, observed just before or after the pulsar observations using the same set up, were used for calibration of raw pulsar data. Typically, correlation coefficients for a few thousand samples (τ, sampling interval, typically 5 to 10 ms) were acquired on the calibrator. The Fourier transform of the correlation coefficients was computed to obtain the power spectrum which is the bandpass of the instrument. These data were used to calculate the mean power and variance in all 32 channels. The ratio of mean power to variance is the signal-to-noise ratio of each channel and this was used as weights in the calibration procedure. These are shown in Figure 3.3 for the calibrator 3C17 for March 12,1996 observations. The response of the pulsar in a frequency channel was scaled by that of the calibrator in the same channel to obtain flux density in Jy in that channel. The 32 flux densities were then averaged using the signal-to-noise ratio in each channel as the corresponding weight. This procedure reduces the contribution of those channels in which the signal to noise ratio is small. The contribution of those channels which are corrupted by sustained interference is also minimized.

The interstellar scintillation increase or decrease the pulsar intensities over sub-bands in the

[b]Dynamic spectra is a plot of intensity as a function of time and frequency. See Chapter 1 Section 1.2

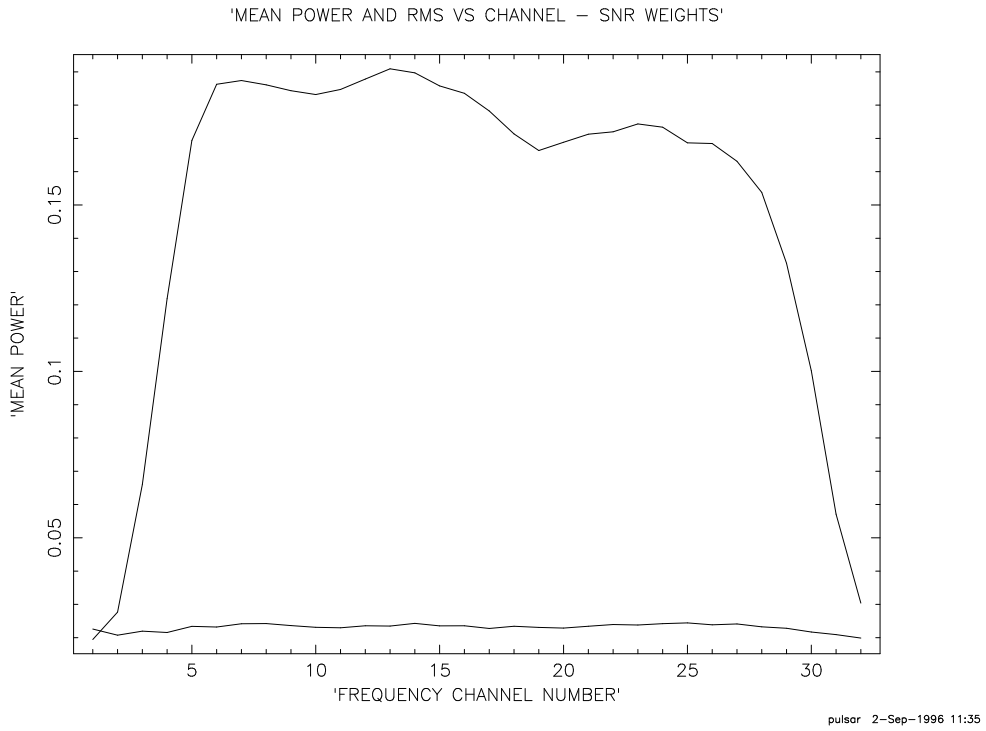

Figure 3.3: The mean power and RMS plotted as a function of frequency channel number for 3C17 on March 12, 1996 observations

overall band of frequencies and this can be used to advantage as explained below. The dynamic spectra of the pulsar can be used to preferentially weight those channels which have a high signal-to-noise ratio. This improves the sensitivity at the cost of the observation bandwidth (Vivekanand 1995); this method was used here. First, two windows were identified for each observation that typically contained 1000 pulses. One is referred to as on-pulse window, and consists of the time samples within which the pulse arrives in each period; the off-pulse window consists of an equal number of off pulse samples. The flux densities of the on-pulse samples were averaged separately in the 32 frequency channels, for sets of 200 individual pulses to obtain the dynamic spectra of the pulsar. This was used to weight the original calibrated flux densities for each channel. The weights for a typical ISS block are shown in Figure 3.4. The decorrelation bandwidth deduced from this figure agrees with the expected value for a DM[c] of 10.9. Typically, the sensitivity of the pulsar data was enhanced by a factor of $\sqrt{2}$.

The flux density of the pulsar after calibration is given by the following formula.

$$S_p = \frac{S_c}{\overline{R_c}} \cdot \frac{\sum_{i=1}^{32} R_i \cdot W_i \cdot W_{dsp}(i)}{\sum_{i=1}^{32} W_i \cdot W_{dsp}(i)} (Jy) \tag{3.1}$$

where

[c]DM - Dispersion measure is the column density of electrons in the path to the source ($\int_0^d n_e dl$)

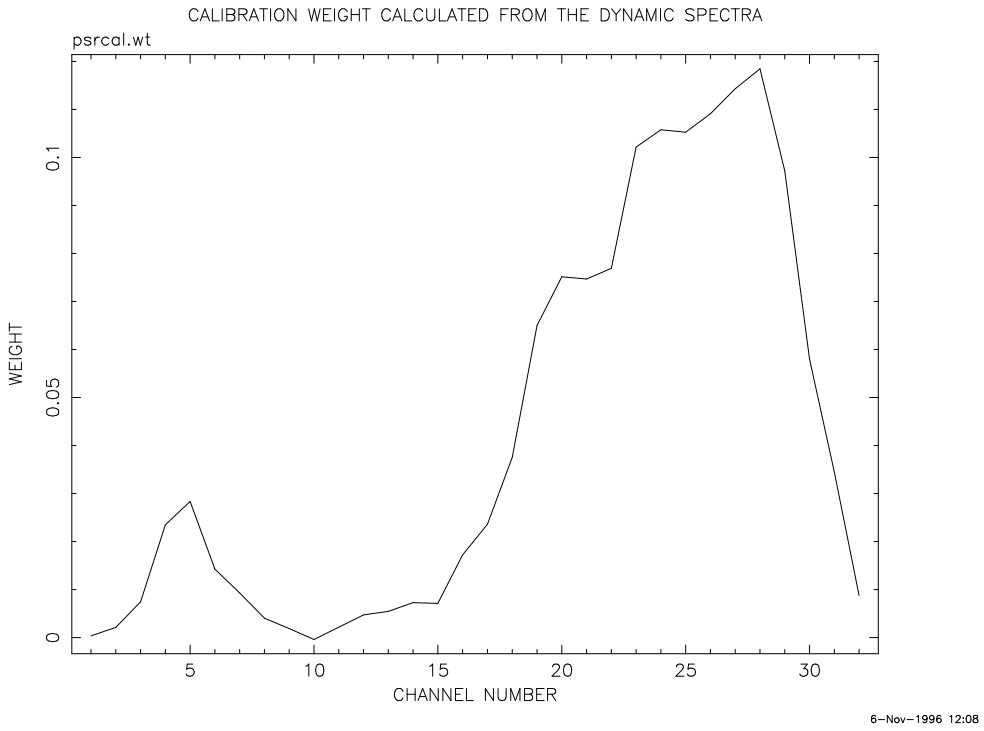

Figure 3.4: The dynamic spectra weights for a typical ISS block

S_p = weighted pulsar flux over 9 MHz bandwidth (Jy)

S_c = flux of calibrator (Jy)

$\overline{R_c}$ = mean response of a channel to the calibrator obtained from the calibrator observations (arbitrary units)

R_i = response to the pulsar in a channel i obtained from the pulsar observations (arbitrary units)

W_i = Signal-to-noise ratio in the i^{th} channel as derived from the response to the calibrator (dimensionless)

$W_{dsp}(i)$ = weight of a channel derived from the dynamic spectra (arbitrary units)

The summation in the numerator and denominator of Equation 3.1 was typically over channels 3 to 30 to ignore end channels.

The DM of the pulsar was used to dedisperse the data and collapse power in all 32 channels to give a single time series for the pulsar. The null and the burst pulses in this time series were then identified using the procedure described in the next section.

3.3.2 Identification of Null and Burst Pulses

One aim of this thesis was to study the relationship between nulling and drifting. Hence, it is necessary to identify the null and burst periods and this was carried out using the extreme value method proposed by Vivekanand (1995). A brief description of this method is given in this section.

First, all pulses in a typical observing session were averaged modulo the period to obtain the

integrated profile. The range of samples, corresponding to this profile, were identified in each period. This window, referred as the on-pulse window, represents a duration when the pulsar's energy is received. An equal number of samples, well away from those corresponding to the on-pulse window were also identified as off-pulse samples.

The energy in these windows can be estimated by adding the power corresponding to all the samples in the window. The off-pulse energy is simply the receiver noise and has a zero mean normal distribution, whereas the on-pulse energy represents the distribution of individual pulse intensities. No emission is detectable during a nulled pulse and the on-pulse energy is just the receiver noise. Hence, the on-pulse energy for the nulled pulse has a distribution similar to the off-pulse energy. Therefore, the nulling pulsars exhibit a bimodal on-pulse energy distribution. The null and burst periods can therefore be identified by considering a suitable threshold separating the two distributions.

These distributions overlap in many pulsars for the following reasons. Firstly, pulsars are weak radio sources and the observed mean intensity for these sources is usually not much larger than few times the standard deviation of the off-pulse distribution due to the sensitivity limitations of most telescopes. Secondly, the width of subpulse is typically much smaller than the on-pulse window. Thus, no pulsar power is received in the large fraction of on-pulse samples. Lastly, the estimation of on-pulse energy is complicated for pulsars such as PSR B0031-07, where the subpulse arrive at progressively changing phase within the on-pulse window. There are usually two or more subpulses present in a period and the shape of weak subpulses is also affected by the receiver noise making a matched filter approach for estimating on-pulse energy difficult for such pulses. Therefore, it is difficult to decide a suitable threshold for such pulsars.

Vivekanand (1995) showed that these difficulties can be overcome by estimating the on-pulse and off-pulse energies by considering the highest three to five samples (typically the width of a subpulse) in these windows. This estimator is a biased estimator as the off-pulse energy distribution now has a non-zero mean, but the improvement over the previous method is $\sim \sqrt{N/M}$ where N is the number of samples in the on-pulse window and M is the number of extreme values considered. This factor is usually of the order of 2 for most pulsars.

The energy in the on-pulse window and that in the off-pulse window were estimated approximately by summing the highest 3 to 5 samples within the respective windows as the typical subpulse width is of the order of three samples for the data used in this thesis. All periods with on-pulse energy below a threshold, defined as the sum of the mean off-pulse energy and 5 times its standard deviation, were considered as nulled periods. For these nulled periods the root-mean-square (RMS) energy in the on-pulse window was monitored, and a visual examination of the data for those nulled periods which had a higher on-pulse RMS invariably showed weak subpulses. These subpulses were also compared with the drifting pattern in the preceding and succeeding periods for additional confirmation. Such pulses were relabeled as burst pulses. Finally, the integrated profiles of the burst and the nulled pulses were separately obtained. The power in the null

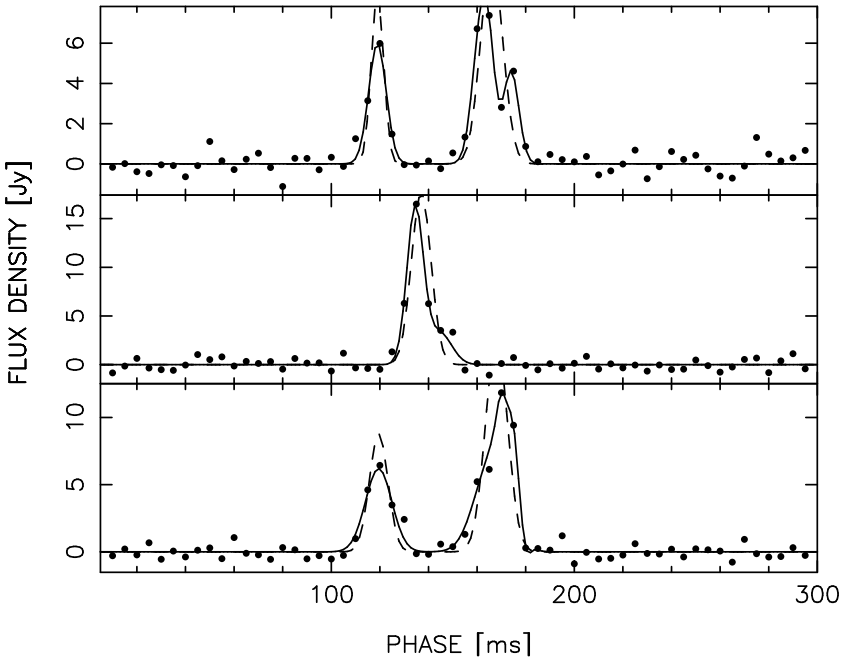

Figure 3.5: Three examples of calibrated flux density of PSR B0031-07 obtained on Oct 25, 1992. The solid curves are modeled subpulses; the dashed curves are the equivalent Gaussians

pulse profile is less than 0.01 per cent of that in the burst. Moreover, any peak in the nulled pulse profile is uncorrelated with the the burst profile. So, we are confident that almost no weak burst period would have been wrongly identified as a null period.

Once the burst pulses were identified, their subpulses were modeled as Gaussians as described in the next section and the drift rates were obtained from this modeled data.

3.3.3 The Subpulse Modeling

A visual examination of the data revealed that a majority of the subpulses closely resembled a Gaussian in shape. Hence, it was decided to model the subpulses using Gaussians. Moreover, it was also more convenient to obtain the position and width of the subpulse from the modeled Gaussian.

An example of typical subpulses is shown in Figure 3.5. The calibrated data are plotted as dots. First, all peaks within the on-pulse window that are above a threshold flux density (typically 3 times the RMS receiver noise) were located. A set of Gaussians, typically 2 or 3, was then fitted in a least square sense to these features. A non-linear fitting routine[d] was used for this purpose (Press et al. 1992). The pulses with a reduced χ^2[e] higher than 1.75 were flagged and the process was repeated three to four times using different initial values for the Gaussian parameters. Each

[d]Non-linear model fitting is reviewed in Appendix A.3

[e]χ^2 is defined in Appendix A.1

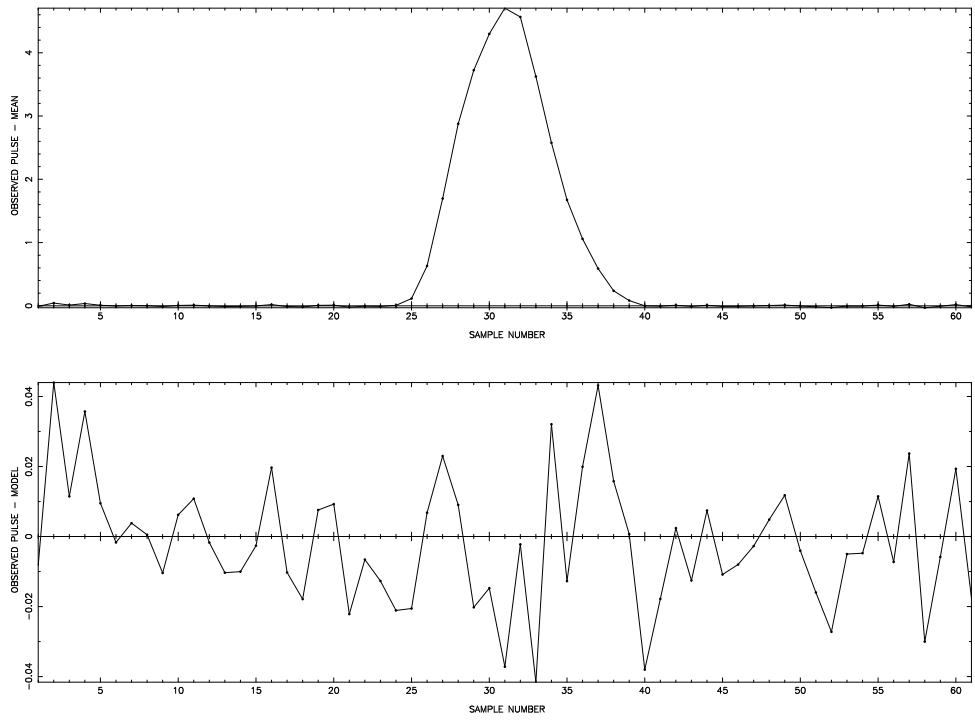

Figure 3.6: The integrated profile and the residual profile for June 10, 1995 data

fit was visually examined by superposing the modeled curve upon the corresponding data and the bad fits were flagged. These subpulses were individually modeled by trial and error until almost every fit met the required criterion of the reduced χ^2. Thus, each subpulse was modeled as a sum of 2 or 3 Gaussians. The solid curves in Figure 3.5 represent the modeled subpulses. The integrated profile and the residual profile obtained after removing the model contribution from the raw data were then obtained for each observing session. The profiles for June 10,1995 data are shown in Figure 3.6. The ratio of the integrated profile peak to residual peak was treated as a measure of the goodness of fit for the entire data. Typically, this number was 0.02 (or 2 percent). The above analysis was carried out successfully for 34126 out of 44404 individual periods of data. The data for the rest of the individual periods were of relatively poor quality.

Once all the pulses were modeled by a set of Gaussians, these were separated into groups representing subpulses. Any pair of Gaussians with a separation of peaks less than 1.75 times the sum of their widths was considered to belong to a group. Each group of Gaussians was reduced to an equivalent Gaussian, representing the subpulse, having the same area and the equivalent width, and positioned at the mean position of the group. Now, the modeled curve is given in terms of the constituent Gaussians by

$$y(x) = \sum_{i=1}^{N} A_i \cdot \exp\left(-\left(\frac{x - B_i}{C_i}\right)^2\right) \tag{3.2}$$

then, the parameters of the equivalent Gaussian are given in terms of the constituent Gaussians.

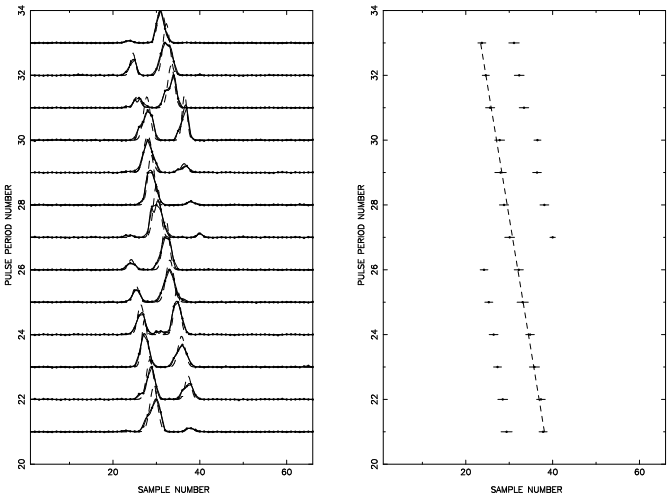

Figure 3.7: Drift bands with best fit straight lines from March 12,1996 data

The normalizing coefficient is

$$A_s = \sum_{i=1}^{n} (\sqrt{\pi} \cdot A_i \cdot C_i) \tag{3.3}$$

the mean position of the subpulse, $\overline{x}$, is

$$\overline{x} = B_s = \frac{\sum_{i=1}^{n} (A_i \cdot C_i \cdot B_i)}{\sum_{i=1}^{n} (A_i \cdot C_i)} \tag{3.4}$$

$$\overline{x^2} = \frac{\sum_{i=1}^{n} (A_i \cdot C_i \cdot (C_i^2/2 + B_i^2))}{\sum_{i=1}^{n} (A_i \cdot C_i)} \tag{3.5}$$

the mean square width of the subpulse is given by

$$C_s^2 = \overline{x^2} - \overline{x}^2 \tag{3.6}$$

These equivalent Gaussians should not be confused with the Gaussians used to model the data. These are indicated by the dashed curve in Figure 3.5. Each equivalent Gaussian was visually checked by superposing over the raw data and the modeled data and the overlap criterion was changed, if necessary. The visual examination of the entire data set makes this exercise very tedious and this is one of the reasons why such analysis were rarely carried out earlier.

In the next step, individual pulses belonging to a drift band were identified by visual examination. A least squares fit to the subpulse positions as a function of the pulse number was carried out using the inverse square of the errors on the positions as the weights. The fitting procedure gave the slope of the line, which is the drift rate α (ms /period), as well as its mean square error. Drift bands with extent less than three individual periods were not considered. The individual periods with subpulses below a threshold energy were also omitted from the fits. A set of individual periods from the data of March 12, 1996, forming a drift band with a straight line fit is shown in Figure 3.7.

The subpulse modeling was useful in estimating subpulse position, the drift rates α, and their errors for 3338 drift bands and these measurements constitute the basis for the study of different subpulse properties in this thesis. A set of special program was developed for these measurements as explained in the next section.

3.4 The Analysis Software

The data reduction software to carry out the tasks described in the last section was written in a general form for estimating subpulse drift in pulsars. Most of the programs were written in FORTRAN77, although a part of the analysis was carried out using a set of procedures written in Interactive Data Language, or IDL (Interactive Data Language 1995).

As is evident from the description in the preceding section, the analysis proceeds in a step by step fashion with a repetition of some steps in order to carry out potentially difficult fits to the data. Experience with the data revealed that the program was able to fit almost 98 percent of the data if 4 to 5 standard set of initial parameters were supplied. The programs were therefore written in an automated mode of operation, in which these standard sets are supplied in a loop. This automated mode could process 1000 individual pulses typically in half an hour (on a Sparc station) without human intervention. The software provides a manual mode in which interactive fitting can be carried out on a visual display of data. This mode was used for the remainder 2 percent of the individual periods for which fitting was comparatively harder. The software also provides a mechanism of examining raw as well as fitted data for each individual period. The fits for the entire data were checked visually using this mode.

Apart from the data reduction software, another set of programs was developed as a part of this thesis. These programs implement the procedure followed for the statistical analysis of the calibrated data described in the subsequent chapters. The data reduction software together with the statistical analysis software consists of more than 50,000 lines of code. It needs to be emphasized that no standard software exists for the analysis carried out in this research work. Hence, this program development forms a substantial and an essential part of this research work.

This software was first tested thoroughly on a small subset of data on PSR B0031−07. Then, the entire data was calibrated and inspected visually to get a qualitative picture of subpulse drift and nulling in this pulsar. This was followed by estimating the drift rates and their distribution. These are presented in the next sections.

3.5 General features of radio emission in PSR B0031−07

A visual examination of PSR B0031−07 data revealed several interesting features. Here, a qualitative description of this data is presented.

Typically, two subpulses were observed in an individual period. The integrated profile, shown in Figure 2.2, was smooth as expected with a typical width of 130 ms. The subpulses were nearly

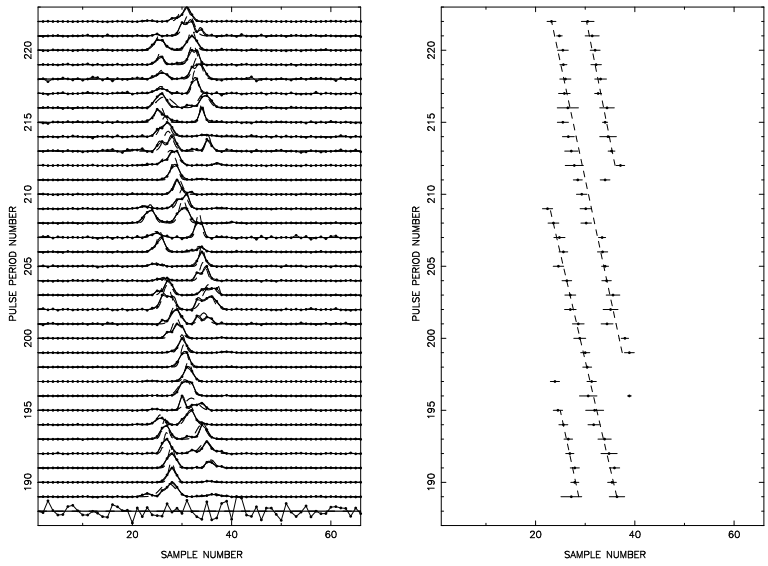

Figure 3.8: A drift band belonging to Class A mode

Gaussian with a typical half power width of $\sim$ 15 ms.

The observed subpulse drift is more variable than what was believed earlier. Mostly, the drift bands were linear with the slope α varying from band to band. A typical drift band lasted for ≈ 10 individual periods consistent with the earlier observations (Huguenin, Taylor and Troland 1970). Distinct states of drifting were apparent to the eye as reported earlier. An example of Class A[f] drift mode is shown in Figure 3.8 and a Class B drift mode is shown in Figure 3.9. Class C drift bands were seen rarely. The transition from one mode to another was often abrupt. Class A mode was observed to generally precede Class B mode in a burst and an isolated burst of Class A mode was never observed. The drifting in Class A mode was observed to be more regular than Class B.

PSR B0031−07 shows prominent nulling with null durations ranging from 1 pulse to 384 pulses, which was the longest null in our data. In general, two different types of nulls were observed in the data. Nulls with durations ranging from one pulse to three pulses were observed frequently and these were typically separated by one to ten pulses. The drift rates in the burst before and after such nulls belonged to the same drift mode for most of these null transitions. In contrast, nulls of longer durations (typically four to several hundred pulses) occurred between bursts with different drift modes. The separation between such nulls was typically 50 periods. These results are consistent with earlier studies of this pulsar (Huguenin, Taylor and Troland 1970; Vivekanand 1995). The latter type of nulls correspond to Type I nulls in Backer's terminology, while the former are Type II nulls. The nulling pattern of this pulsar is presented at the end of this chapter.

[f]Class A, B and C modes were defined in Section 2.4

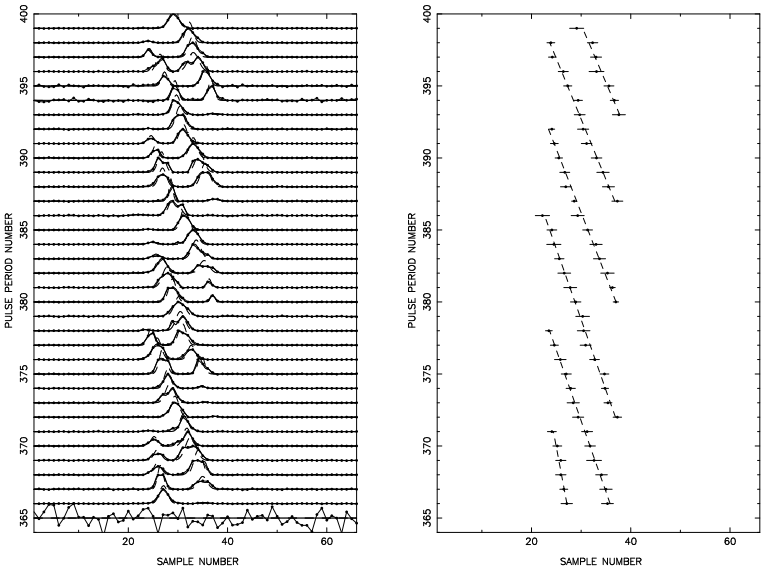

Figure 3.9: A drift band belonging to Class B mode

3.6 The distribution of drift rates

The drift rates for all the drift bands identified in the data were measured using the programs described in the earlier sections and a distribution of drift rates was obtained. This distribution, presented in this section, has two prominent peaks, which confirms a multimodal behaviour of drifting for this pulsar.

The drift rates as a function of band number for the entire data set are plotted in Figure 3.10. A histogram was obtained from the drift rates and their errors for all drift bands in the second phase of the analysis in the following manner. The drift rate of each band can be represented by a Gaussian of unit area, width equal to its RMS error, centered at the given value of drift rate. Here, it is assumed that the measured values of drift rate were derived from a normal distribution. With this assumption, the probability distribution of the drift rates is given by a normalized sum of such Gaussians as given below

$$P_x(\alpha) = \frac{1}{N} \cdot \sum_{i=1}^{N} \frac{1}{\sqrt{\pi} \cdot \sigma_i} \cdot \exp\left[-\left(\frac{\alpha - x_i}{\sigma_i} \right)^2 \right] \tag{3.7}$$

where, N = total number of drift bands

x_i = the i^{th} drift rate

σ_i = the error in i^{th} drift rate

Any peaks in this distribution represent a dominant mode of drifting behaviour. Several curves were fitted to reproduce these peaks. It was found that the following curve fits the data best

$$Q_{\alpha_j}(\alpha) = \sum_{j=1}^{2} L_j \exp\left[-\left(\frac{M_j - \alpha}{N_j} \right)^2 \right] \tag{3.8}$$

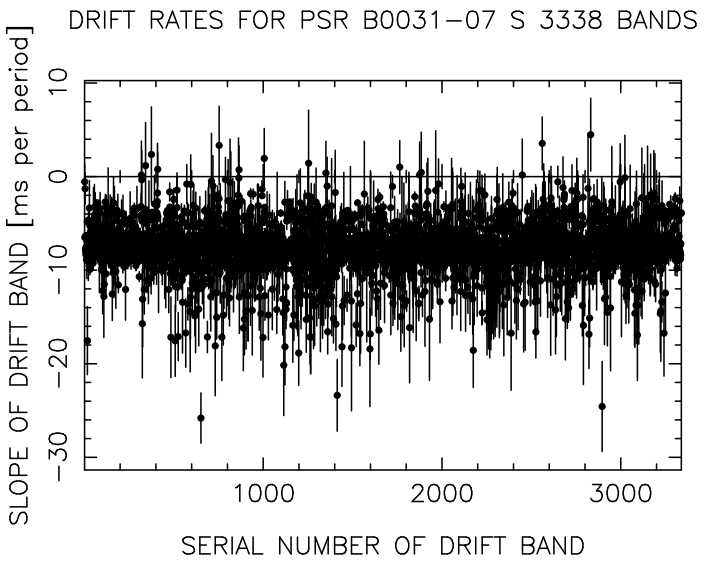

Figure 3.10: Plot of drift rates as a function of band numbers for all 3338 bands

$$\begin{aligned} & L_j = \text{the amplitude of the } j^{th} \text{ model Gaussian} \\ \text{where, } & M_j = \text{the position of the } j^{th} \text{ model Gaussian} \\ & N_j = \text{the width of the } j^{th} \text{ model Gaussian} \end{aligned}$$

The areas of these Gaussians were taken to be proportional to the frequency of occurrence of the given drift mode and the mean position as the mean drift rate.

The observed probability of occurrence of α, given by Equation 3.7 is shown in Figure 3.11. This distribution was computed for 3338 drift bands from 34126 individual periods. The positive values of α in Figure 3.11 had large measurement errors and the area under the curve for $\alpha > 0.0$ was only 1.31 percent. Thus, this pulsar does not show a positive drift consistent with earlier studies.

The curve below $\alpha = 0.0$ in Figure 3.11 shows two prominent peaks. The curve between $\alpha = -13.65$ and $\alpha = -1.16$ was identified by trial and error as most suitable for modeling. The area under this part of the curve is 94.1 % of the total area which leaves 4.6 % of the area below $\alpha = 0.0$ unmodeled. Three Gaussians of the form given by Equation 3.8 plus a constant value were fitted to the curve. The best fit parameters are given in Table 3.1. We define the three drift modes (the definition is somewhat arbitrary) as follows : $-5.4 \leq \alpha < -1.7$ ms/period (Class A), $-10.0 \leq \alpha < -5.4$ (Class B) and $\alpha < -10.0$ msec/period (Class C). The relative occurrence of the two modes is therefore 15.6 %, 81.8 % and 2.6 % respectively. A comparison with Table 2.2 indicates that the drift parameters for these modes are consistent with those of Huguenin, Taylor and Troland (1970).

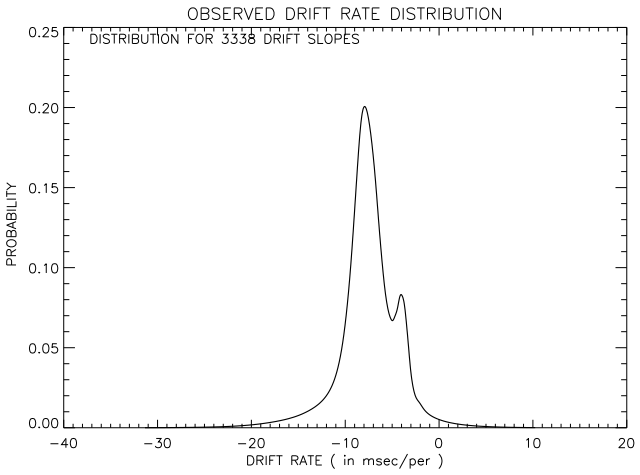

Figure 3.11: Observed Probability Distribution of drift rates

Class	L	M	N	Number of bands
Class A	0.062 ± 0.001	-4.054 ± 0.009	1.138 ± 0.015	520
Class B	0.187 ± 0.001	-7.783 ± 0.004	1.976 ± 0.009	2730
Class C	0.010 ± 0.001	-11.464 ± 0.065	1.288 ± 0.100	88
Const	0.011 ± 0.001			

Table 3.1: Characteristics of three drift modes in PSR B0031−07

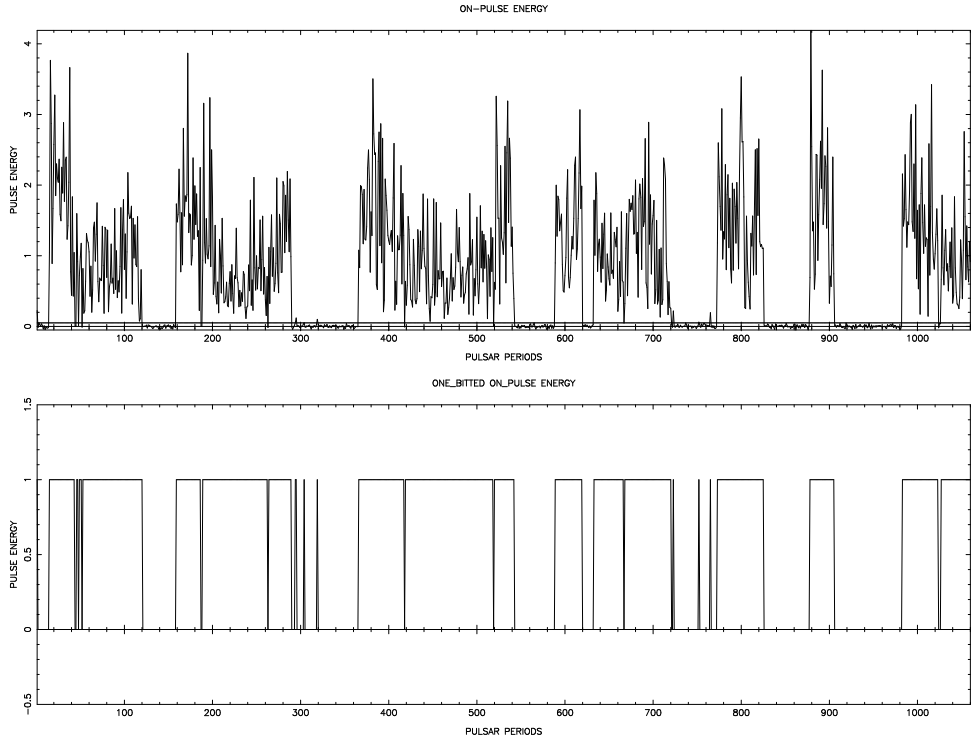

Figure 3.12: Nulling pattern of PSR B0031−07 for the data observed on March 11, 1996. The top panel shows the on-pulse energy as a function of period number and the corresponding nulling pattern is shown in the bottom panel

3.7 Nulling pattern of PSR B0031−07

The nulling pattern of the pulsar, representing the sequence of null and burst pulses, was obtained by representing every null and burst pulse by 0 and 1 respectively. This pattern for the observation of March 11, 1996 is shown in the bottom panel of Figure 3.12. This figure also shows the on-pulse energy as a function of period number in the top panel and it illustrates the abrupt decline in the radio emission from a burst to null. It also suggests a periodicity in this pattern which was tested in the following fashion.

The spectrum of the nulling pattern for each observation, consisting of 1024 pulses, was obtained using Fast Fourier transform. The mean of the data was subtracted and it was multiplied by a hamming window before the Fourier transform was taken. The variance of the data was used to normalize the spectrum for each observation. The spectra for all observations were averaged after normalisation. Any quasi-periodic feature in the nulling pattern is indicated by a broad line feature in this averaged spectrum.

The averaged spectrum for the nulling pattern of PSR B0031−07 is shown in Figure 3.13 and shows a significant feature corresponding to $\approx$ 80 periods. This feature corresponds to a much weaker feature in a similar spectrum reported by Huguenin, Taylor and Troland (1970). However, this feature is quite broad indicating at most a quasi-periodicity in the nulling pattern.

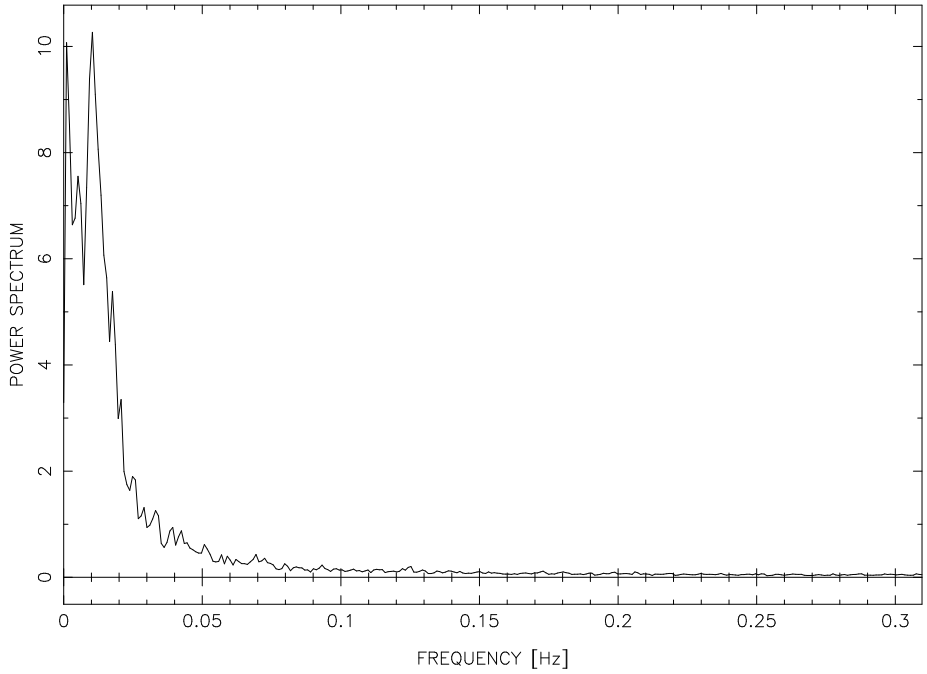

Figure 3.13: Averaged spectrum of the nulling pattern of PSR B0031−07

The measurements presented in this chapter form the essential basis for the study of different aspects of subpulse drift, nulling and mode-changing suggested by the visual inspection of data mentioned above. A detailed analysis of each of these aspects was then carried out using the calibrated and the modeled data and this is described in the next five chapters.

Chapter 4

The Properties of Drifting Subpulses

The drifting phenomenon exhibited by subpulses, which are sometimes regarded as one of the basic units of pulsar radio emission, represents the dynamics of the emission processes. Hence, a useful insight into the changes in these processes is provided by a study of the variation of subpulse properties with the drift rate. The variation of the subpulse width and energy, and that of the separation between two subpulses is investigated in this chapter.

Although subpulse properties, such as the subpulse width and energy, have been studied in the past, there exists no study of their variation with drift rate to the best of our knowledge. Lyne and Ashworth (1983) have reported the energies of subpulses before and after a null for PSR B0809+74 and PSR B0818-13, but its variation with drift rate is not studied as these pulsars exhibit very stable drift rates. Such a variation has also not been reported for PSR B1944+17 (Deich et al. 1986) or PSR B1918+19 (Hankins and Wolszczan 1987), which show a variable drift.

A study of subpulse properties as a function of the drift rate can provide useful new results. For example, the subpulse separation, P_2, has been believed to be constant for pulsars, such as PSR B2016+28. This was first noticed in PSR B0809+74 (Page 1973; Lyne and Ashworth 1983), which exhibits very organized subpulse drift with typically two subpulses in an individual pulse. The subpulse separation in this pulsar can be estimated directly from the positions of the subpulses in the individual pulses. On the other hand, no such direct measurements have been made for pulsars such as PSR B2016+28, which show variable drift rates. The average subpulse separation for these pulsars is inferred from the phase resolved fluctuation spectrum [a]. It is difficult to make quantitative comparisons of the stability of subpulse separation and the drift rates using the phase resolved fluctuation spectrum. Such comparisons have not been reported in the literature except in the case of PSR B0809+74, where Lyne and Ashworth (1983) showed from their direct

[a]The Fourier spectrum of pulse to pulse intensity fluctuations at a given position or phase within the integrated profile is called phase resolved fluctuation spectrum. This is usually computed over 512 pulsar periods. See Section 2.1.1

measurements that the subpulse separation was much more stable than the drift rate. It has been assumed that this stability implies a value of the subpulse separation, which does not change for a given pulsar. However, this reported stability *need not* imply that the subpulse separation is independent of drift rate as this pulsar also exhibits very little variation in the drift rate. In other words, it is not clear whether the constant subpulse separation in this pulsar is a consequence of a more or less constant drift rate. Thus, there is a need to investigate the variation of the subpulse separation with the drift rate for a pulsar, which not only exhibits organized drift, but also permits a direct estimation of the subpulse separation as in the case of PSR B0809+74.

The results of such a study can be useful in constraining the pulse emission mechanism of pulsars. In the example cited above, a value of subpulse separation which does not vary with the drift rate implies that this separation is determined independently of the process which causes drifting. At the same time, a careful scrutiny of Ruderman and Sutherland (1975) model reveals that the separation of "sparks", which are responsible for the subpulse emission in this model, and their motion are related. This issue is discussed in detail in the context of the results of this chapter in Chapter 9 and it can be resolved by a study of the kind described in this chapter. Since PSR B0031−31 exhibits both organized drifting as well as drifting with different values of drift rates in three drift modes, it is well suited for such a study. The drift dependent properties of subpulses in this pulsar are presented in this chapter.

4.1 Average subpulse properties for a drift band

The subpulse energy, in general, varies from pulse to pulse, while the subpulse width is observed to be more or less constant. Since the objective of this study was to examine their dependence on the drift rate, α, these subpulse properties were averaged over each of the drift bands identified in the data. The measurements of the root mean square deviation of a subpulse from the linear systematic drift of a drifting subpulse as well as those of the average subpulse energy and width for a drift band are presented in this section after a brief description of the method of analysis.

4.1.1 Analysis Procedure

In order to average the subpulse energy or width over a drift band, it is necessary to know the drift rate and the extent of this band as well as the location of the subpulses in the band. These quantities were estimated in the data reduction phase as mentioned in the last chapter. Here, the calibrated data were examined using the results of that analysis and the above mentioned properties were estimated.

As mentioned in the last chapter, a small number of drift bands showed irregularities in drifting behaviour, such as systematic reduction or enhancement of drift rate at the edges. Abrupt change of drift rate in the middle of the band was also noticed for a small number of drift bands. Such

drift bands were not considered in this analysis, which included a total of 3155 drift bands. The typical ratio of the peak of the subpulse to the RMS of the samples in the off-pulse window [b], also called signal to noise ratio, was of the order of 20 for the drift bands in consideration.

The starting point of this analysis was to use the drift band identifications carried out in the data reduction phase (See Section 3.3.3) to find out the periods constituting a given drift band. Often, these periods have two subpulses and the first task was to select the subpulses associated with the drift band in consideration. First, the positions of subpulses in each period were obtained. These subpulses were modeled as Gaussians in the data reduction stage and the centroid of the Gaussian was taken as the location of the subpulse in the calibrated data (Section 3.3.3). A line was fitted to each band in Section 3.3.3 and the expected position of a subpulse , x_b, belonging to a given band can be calculated from the best fit slope, α, and the offset, x_{off}, of this line. The subpulse located closest to this expected position was taken to be associated with the given drift band. The drift rate of this band, given by the slope α, of this line, was also noted.

Then, the root mean square deviation of the subpulse from a linear drift was calculated for each drift band. This is given by

$$\Delta x = \sqrt{\frac{1}{N}\sum_i (x_b - x_{si})^2} \tag{4.1}$$

where,

x_b = position of the subpulse predicted by the overall drift rate of the band, *i.e.*, $x_b = x_{off} + n\alpha$, where

- x_{0ff} = phase offset of the best-fit line for the drift band
- n = period number
- α = slope of the best-fit line or the drift rate for the band

x_{si} = position of the i^{th} modeled subpulse

N = total number of periods in the band

and the error on this deviation is given by

$$\sigma_{\Delta x} = \left(\frac{\frac{1}{N}\sum y_i^2 - (\frac{1}{N}\sum y_i)^2}{4(\frac{1}{N}\sum y_i)} \right)^{\frac{1}{2}} \tag{4.2}$$

where

$$y_i = z_i^2 = (x_b - x_{si})^2 \tag{4.3}$$

These expressions are derived in Appendix C.3. It is to be noted that the expression for $\sigma_{\Delta x}$ does not assume any explicit distribution for the random variable such as z_i and the standard error is calculated from the data using first principles. However, this expression reduces to $\sigma_{z_i}^2/2$ in the case when z_i are normally distributed random variables ($z_i = x_b - x_{si}$ as defined in Equation 4.3). This can be verified by substituting the second and fourth moments of z_i, which is a zero mean normal random variable by definition in this particular case.

[b] Off-pulse window is defined in Section 2.2

Next, the subpulses associated with the given drift band were isolated. This is required as there exists typically two subpulses in a majority of the individual pulses in this pulsar and it is convenient to estimate the subpulse properties averaged over a given band by removing the subpulses belonging to other drift bands. First, the mean energy in the off-pulse samples was estimated in each period associated with the drift band and this was subtracted from the calibrated data. Then, a range of samples around the associated subpulse in the calibrated data were retained for each period in the drift band in consideration. As will be shown later in Section 6.1.2, the average subpulse separation, P_2, between two subpulses in this pulsar is 50.81 ms. Hence, a range corresponding to 60 ms around the subpulse was selected in the final analysis for this purpose. All the samples lying within 30 ms of the position of the subpulse subpulse were included and the rest of the samples were made zero. This effectively removes any subpulses belonging to drift bands other than the one in consideration.

However, such an isolation could not be carried out for a small number of drift bands as the separation between the adjacent bands was much smaller than the above mentioned typical value for these bands. This was seen in about two percent of total number of drift bands and such drift bands were not considered for this analysis.

Then, all the subpulse associated with the isolated drift band were aligned to an arbitrary reference phase. The phase shift required to align each subpulse in the band with this reference phase was obtained from position estimated from the modeled subpulse data. Each subpulses was then suitably shifted. Some examples of individual drift bands before and after alignment are shown in the left and middle panels of Figures 4.1, 4.2, 4.3 and 4.4.

Finally, an integrated profile of the subpulse for the band was formed by adding these aligned pulses as shown in the rightmost panel in these figures. The range of samples associated with the subpulse was determined by visually examining the profile for each drift band for the entire data set. The subpulse energy was observed to lie within 22.5 ms of the peak in all these profiles and this was selected as the range of samples for the subpulse. A sum of the energies in these samples gives an estimate of the mean energy in the subpulse. The error in this estimate was computed by determining its second moment.

A weighted root mean square deviation from the mean position of the subpulse profile obtained above was used to estimate the width of the subpulse for each drift band. This is given by

$$W = \left(\frac{\sum p_i x_i^2}{\sum p_i} - \left[\frac{\sum p_i x_i}{\sum p_i} \right]^2 \right)^{\frac{1}{2}} \tag{4.4}$$

where,

p_i = power in the i^{th} sample in the subpulse profile

x_i = phase of the subpulse profile

and its standard error is given by

$$\sigma_w = \left[\frac{\sum \left(\frac{x_i (x_i - 2\overline{x})}{(\sum p_i)^2} \right)^2 \sigma_{p_i}^2}{4W^2} \right]^{\frac{1}{2}} \tag{4.5}$$

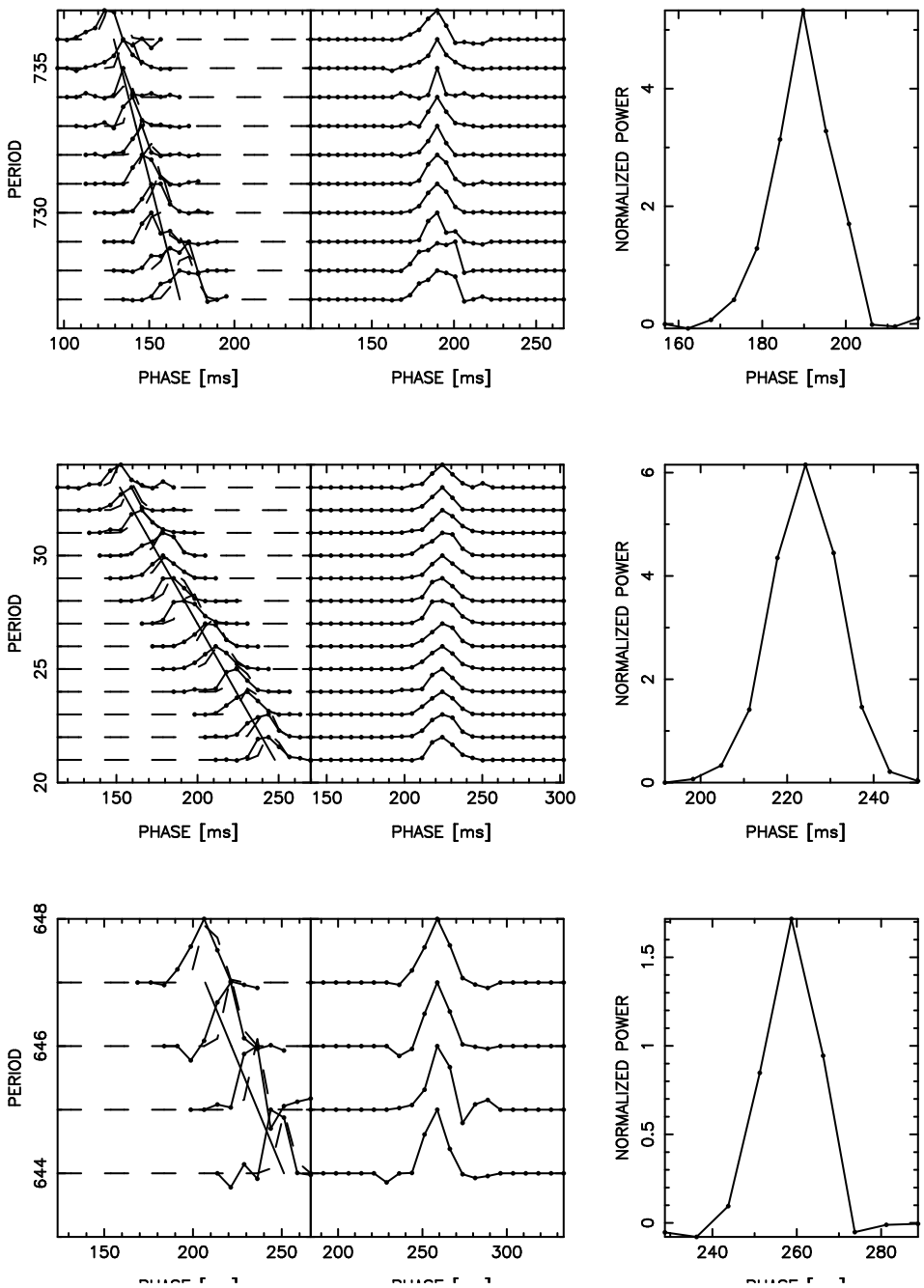

Figure 4.1: The subpulse integrated profile for individual bands. The leftmost panel in each of the three plots (top, center and bottom plots) in this figure shows the subpulse associated with a given drift band (solid line). Data falling in samples within 60 ms around each subpulse are retained for the reasons explained in the text. The aligned subpulses after shifting each subpulse to an arbitrary reference phase are shown in the adjacent panel. The rightmost panel of each of the three plots shows the integrated subpulse profile for this band. The top plot shows a typical drift band for Class A drift mode, whereas typical Class B and C drift bands are shown in the center and bottom plots

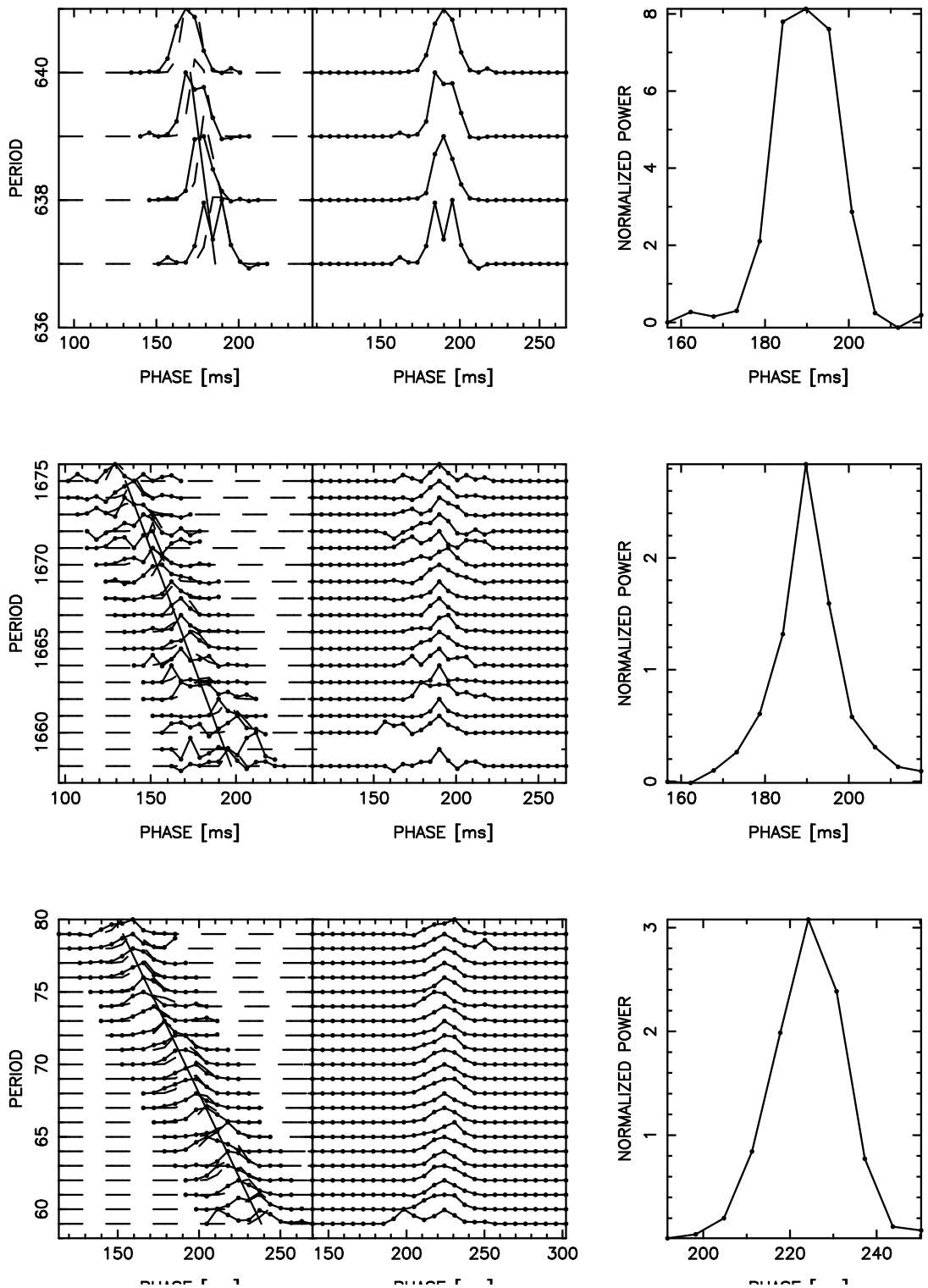

Figure 4.2: The subpulse integrated profile for individual bands as in Figure 4.1. This figure illustrates the typical variation in the integrated subpulse profile for Class A drift mode by three examples shown in the top, center and bottom plots

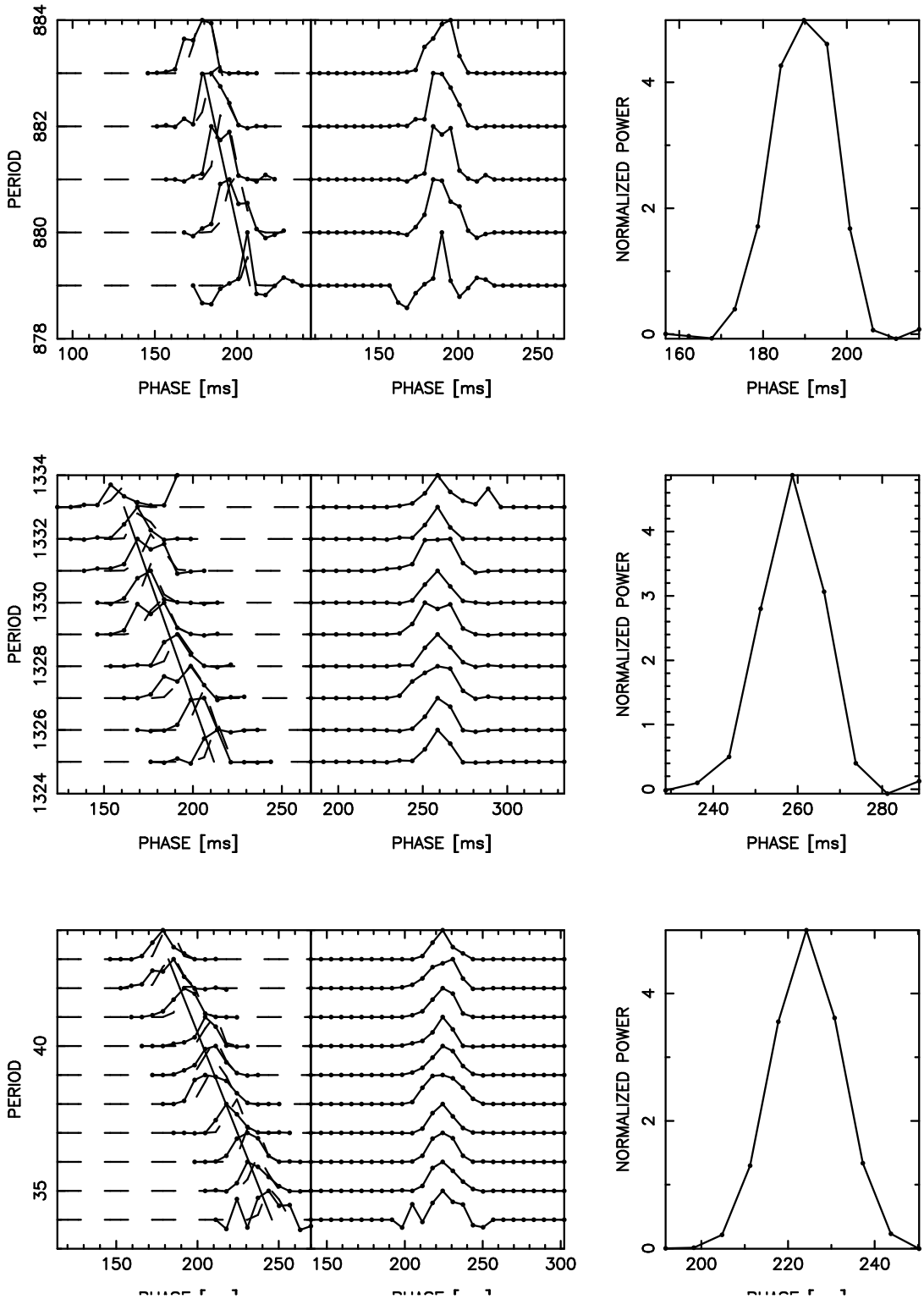

Figure 4.3: The subpulse integrated profile for individual bands as in Figure 4.1. This figure illustrates the typical variation in the integrated subpulse profile for Class B drift mode by three examples shown in the top, center and bottom plots

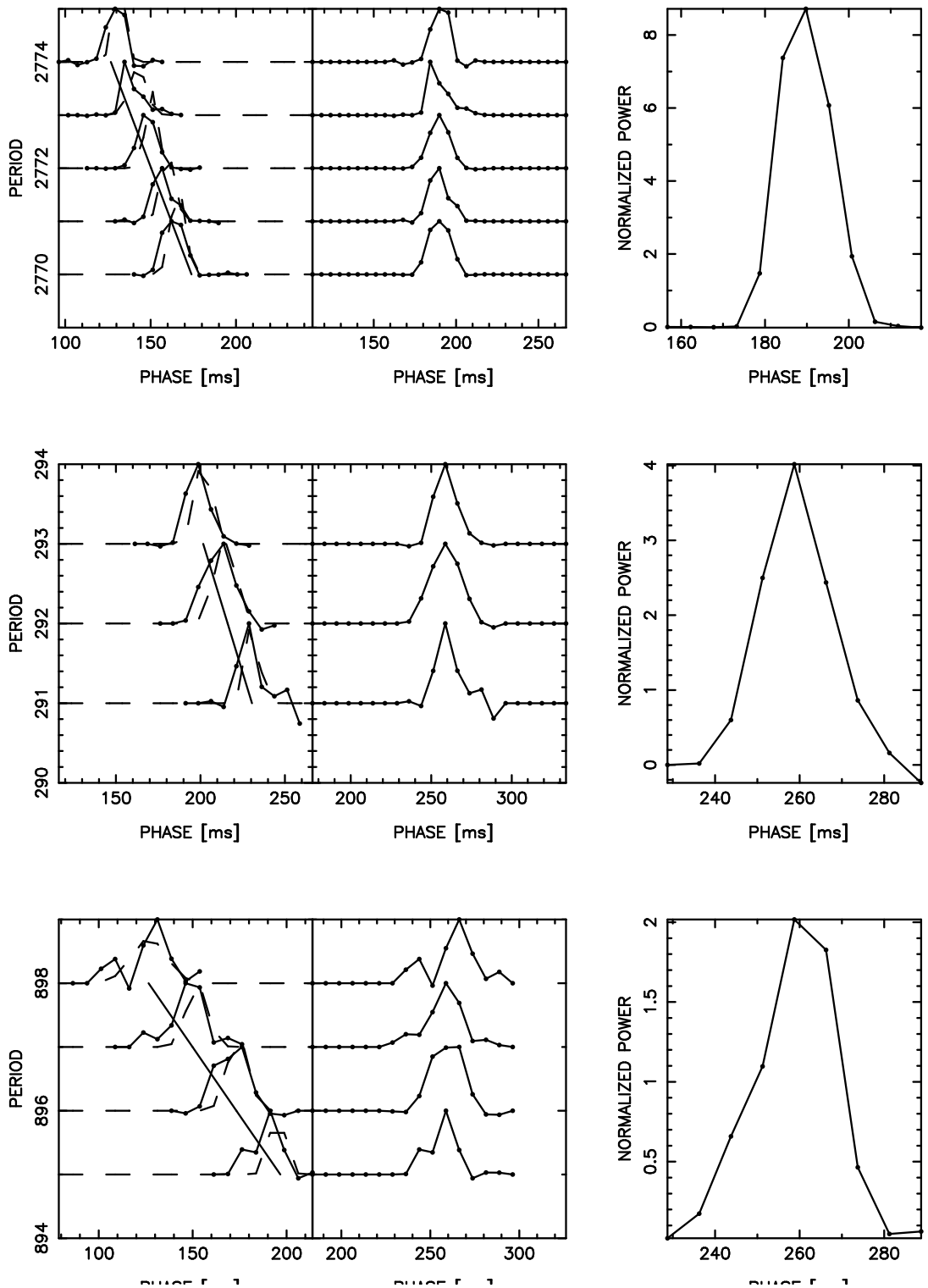

Figure 4.4: The subpulse integrated profile for individual bands as in Figure 4.1. This figure illustrates the typical variation in the integrated subpulse profile for Class c drift mode by three examples shown in the top, center and bottom plots

where,

$\overline{x}$ = $(\sum p_i x_i)/\sum p_i$, the weighted mean position of the subpulse

σ_{p_i} = the standard error on p_i, power in the i^{th} sample in the subpulse profile

A possible error in determining the phase shift required to align the subpulses can broaden the average subpulse profile of the drift band. The energy of the average subpulse is not significantly altered by such a procedure as it was estimated by adding the energies in all samples of the subpulse. However, this can contribute a random error in the estimate for the subpulse width as a small fraction of energy of the subpulse now appears in the samples at the edges of the subpulse profiles. Thus, an estimate which minimizes the contribution of these samples to the width is required. The weighted estimate of Equation 4.4 is just such an estimate and this was was used to minimize the effect of any error in the phase shift. This error is same as the error in the position of subpulse and is usually smaller than one sampling interval.

The integrated profiles of the subpulse for some selected drift bands are shown in Figures 4.1, 4.2, 4.3 and 4.4. Figure 4.1 shows typical drift bands in each of the three drift modes of this pulsar, namely Class A, B and C. The typical variation of the integrated profile for each of Class A, B and C drift mode is illustrated by three examples each in Figures 4.2, 4.3 and 4.4.

4.1.2 RESULTS AND DISCUSSION

A plot of the root mean square deviation from the mean slope, the subpulse energy and the width of subpulse as a function of drift rate for 3155 drift bands is shown in Figure 4.5. This figure should be treated with caution as there are uncertainties on the estimated α also. The mean uncertainties in both axes are indicated on the figure by crosses in the right upper corner of the figure. The subpulse has a mean energy of 0.09 ± 0.001. This energy is higher for the dominant drift mode (Class B : $-10.0 \leq \alpha < -5.4$ ms period^{-1}). Similarly, the RMS deviation in the position of the subpulse about the drift slope is larger in the dominant drift mode, its average value being 3.11 ± 0.03 ms. In contrast, the width of the subpulse seems to be independent of the drift rate with an average value of 7.44 ± 0.02 ms.

The above results can be potentially affected by several factors and a brief discussion of these is given below. The pulsar flux is affected by interstellar scintillation and this can possibly introduce an error in the estimates of the subpulse energy cited above. A bandwidth of 9 MHz was used for these observations and typically two scintles were seen in this frequency band. The diffractive interstellar scintillation (DISS) was effectively taken care of in the data reduction by using the dynamic spectra of the pulsar as mentioned in the last chapter. Moreover, the data was scaled by the average energy computed for 200 pulses around the drift band to account for any pulse amplitude variation due to refractive interstellar scintillation (RISS). Thus, our estimate is not affected by interstellar scintillation.

ORT has a single polarization, which could affect both the subpulse energy and shape. However, the polarization angle swing is small for this pulsar and the fractional polarization has a minimum

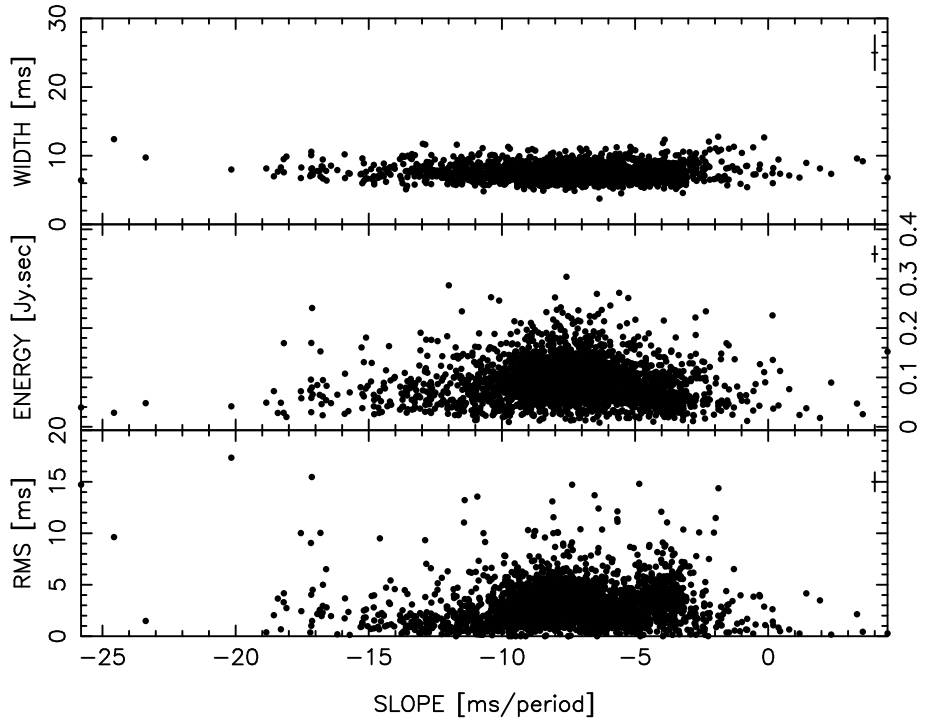

Figure 4.5: The subpulse properties as a function of drift rate. The root mean square deviation of the subpulse from the position predicted by the drift rate as a function of drift rate, α, is shown in the bottom panel. Likewise, the average subpulse energy for a drift band is plotted in the center panel, while the average width of the subpulse in a drift band is shown in the top panel

near the peak of the subpulse (Manchester, Taylor and Huguenin 1975). Hence, the estimate of the subpulse energy are affected marginally. The single polarization nature of data may introduce a systematic error in the subpulse width estimate. However, since all subpulses are likely to be affected in a similar fashion, this does not change our conclusion significantly.

The 9 MHz band of ORT was split into 32 channels in order to dedisperse the time series. The dispersion delay across each of the $\approx$ 280 kHz channel is $\approx$ 700 μsec. This is much less than the sampling interval of $\approx$ 5 ms. Hence, the dispersion smearing of the subpulse does not alter our estimates significantly.

Lastly, the apparent energy in the subpulse is a function of the phase of the subpulse in the integrated profile and is weighted by the integrated profile. Thus, the average subpulse energy can have a systematic error if the drift band in consideration samples a limited number of samples in the integrated profile. A majority of drift bands in the data span the complete integrated profile window and care was taken to include only such drift bands in the analysis.

4.2 Estimation of subpulse spacing and band spacing

Previous observations have indicated that the separation between a pair of drifting subpulse, P_2, is a very stable quantity (Page 1973; Lyne and Ashworth 1983). Since PSR B0031-07 exhibits

variable drift rate, it is interesting to estimate P_2 as a function of the drift rate, α. As the drift rate in PSR B0031−07 varies from band to band, the subpulse spacing for a pair of drift bands with significantly different drift rates varies with pulse number complicating this analysis. Thus, P_2 is meaningful only for the drift bands with consistent slopes, i.e. the bands with drift rates α_1 and α_2 which are consistent with each other within errors. A selection of such drift bands was carried out for estimation of P_2 as described in this section.

4.2.1 ANALYSIS PROCEDURE

First, the subpulses associated with the two adjacent drift bands were identified in a manner similar to the last section using the modeling carried out in the data reduction stage. The drift rates and their errors, estimated in the data reduction phase, were examined for the two drift bands in consideration. This pair of drift band was included in the analysis only if the difference in their drift rates was less than the total error,i.e, the square root of the sum of the squares of the errors on individual drift rate. Next, the number of periods common to both the drift bands was determined. A pair of drift bands with less than three common periods was rejected. A total of 277 out of the 3338 drift bands in the entire data set satisfied these two criterion and were used in the analysis of this section.

The periods common to both the drift bands were then displayed and separate straight lines were fitted in the least square sense to both the drift bands. The drift rate and the phase offset $(\alpha_1, \phi_1, \alpha_2, \phi_2)$ for each drift band was estimated from these fits. Next, a weighted average of these drift rates for the two bands was calculated. This is given by

$$\overline{\alpha} = \frac{\left(\frac{\alpha_1}{\sigma^2_{\alpha_1}} + \frac{\alpha_2}{\sigma^2_{\alpha_2}}\right)}{\left(\frac{1}{\sigma^2_{\alpha_1}} + \frac{1}{\sigma^2_{\alpha_2}}\right)} \tag{4.6}$$

The subpulse position data over all periods corresponding to each of the drift band was fitted to straight lines with the mean slope calculated above (the parameters of these lines are $\overline{\alpha}, \phi_{m1}, \overline{\alpha}, \phi_{m2}$). Two examples, illustrating this procedure, are shown in Figure 4.6 (Class A drift bands) and Figure 4.7 (Class B drift bands). The dashed lines in the right panel are the best fit slopes to each drift band corresponding to slope α_1 and α_2, whereas the fit to the mean slope $\overline{\alpha}$ to the data of both the bands is indicated by the solid lines, which are parallel by definition.

An estimate of the position of a band is given by the phase offsets obtained in these fits (ϕ_{m1}, ϕ_{m2}). The average separation between the two bands, namely P_2, is then the difference of these offsets. The error on P_2 can be obtained from the error on these offsets obtained from the fits in the usual fashion. Thus,

$$P_2 = \phi_{m2} - \phi_{m1} \tag{4.7}$$

and ,

$$\sigma_{P_2} = \sqrt{\sigma^2_{\phi_{m2}} + \sigma^2_{\phi_{m1}}} \tag{4.8}$$

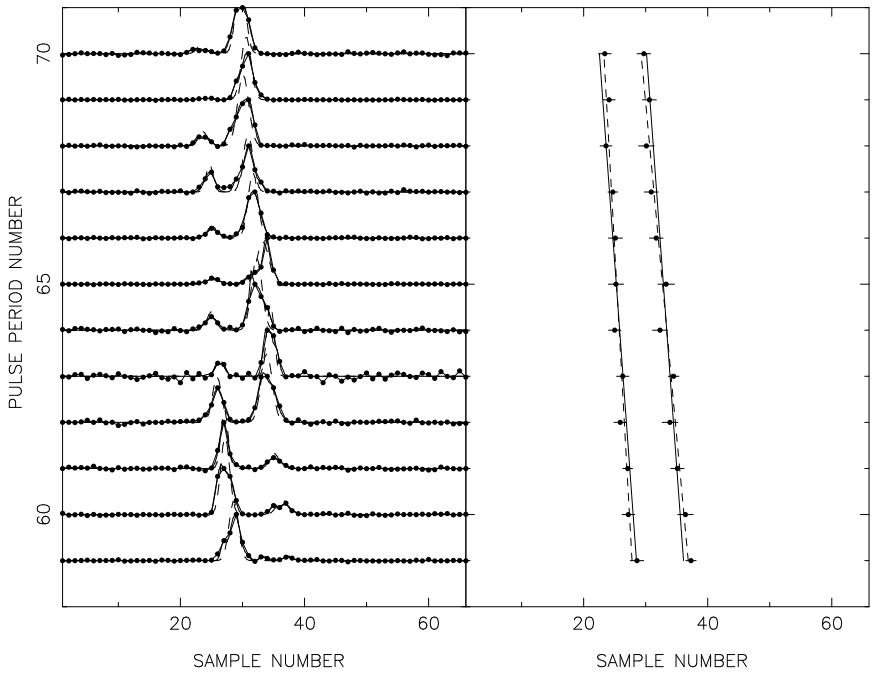

Figure 4.6: The estimation of P_2 for a pair of overlapping Class A drift bands. The left panel shows the raw data as well as the modeled subpulses for the periods common to both the drift bands. Best fit straight line for each drift band is indicated by dashed lines in the right panel for these periods. The data was then fitted to a line with a slope which is average of the slopes of the individual drift band, as explained in the text, and these are indicated by the solid lines

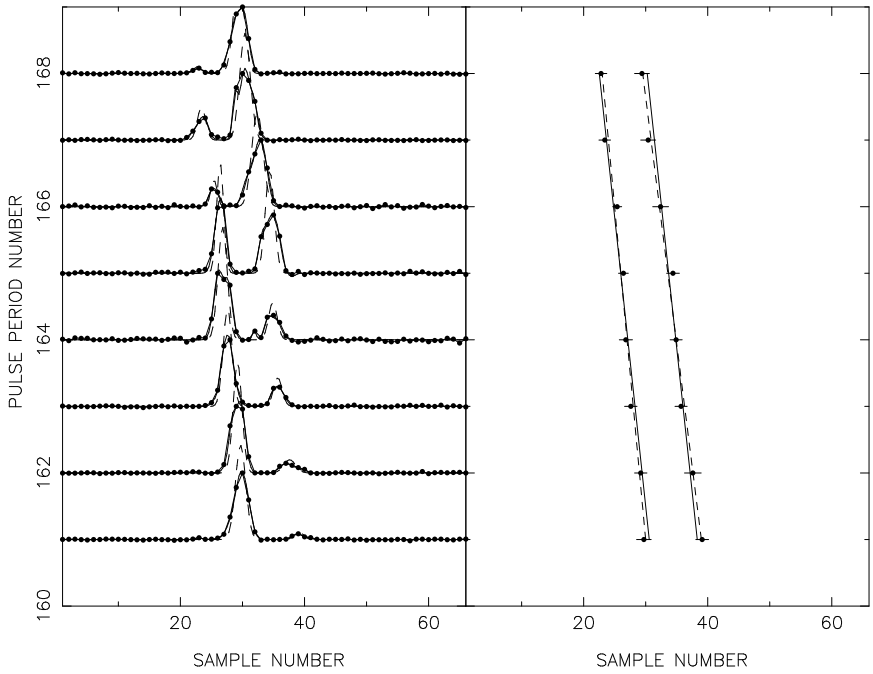

Figure 4.7: The estimation of P_2 for a pair of overlapping Class B bands

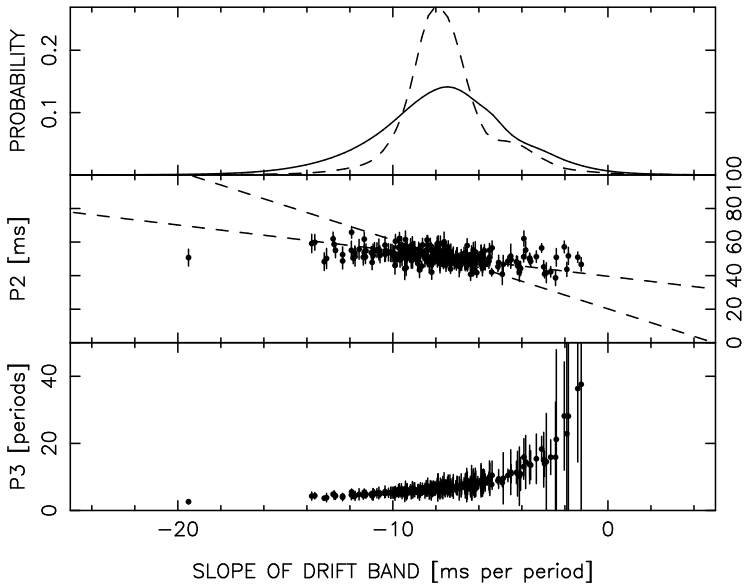

Figure 4.8: The center panel shows the subpulse separation, P_2, alongwith linear fits to the data. The line with a less steep slope indicates the fit to all data points excluding the isolated slope at $\alpha = -19.503$ ms period^{-1}, whereas the other dashed line represents the fit to the drift slopes belonging to Class B drift mode only. The inter-band spacing, P_3, is plotted in the bottom panel, while the distribution of α is shown in the top panel. The solid line in the top panel indicates the distribution of α used in this analysis, while the dashed line represents the overall distribution of α

The internband spacing, P_3, was then calculated from the mean drift rate, $\overline{\alpha}$, and P_2 and is given by

$$P_3 = \frac{P_2}{\overline{\alpha}} \tag{4.9}$$

4.2.2 RESULTS AND DISCUSSION

Figure 4.8 shows the distribution of P_2 and P_3 as a function of drift rate α along with one standard deviation errors. An increasing trend of P_2 with the magnitude of drift rate is apparent from the plot. In order to test this trend, a linear fit was carried out to the data. This fit is complicated as there are errors in both the ordinate and absicca in Figure 4.8. Let the fitted model be given by

$$P_2(\alpha) = A\alpha + B \tag{4.10}$$

The chi-square for a fit involving errors in both P_2 and α is given by

$$\chi^2(A,B) = \sum_{i=1}^{N} \frac{(P_{2_i} - A\alpha_i - B)^2}{\sigma^2_{P_{2_i}} + A^2\sigma^2_{\alpha_i}} \tag{4.11}$$

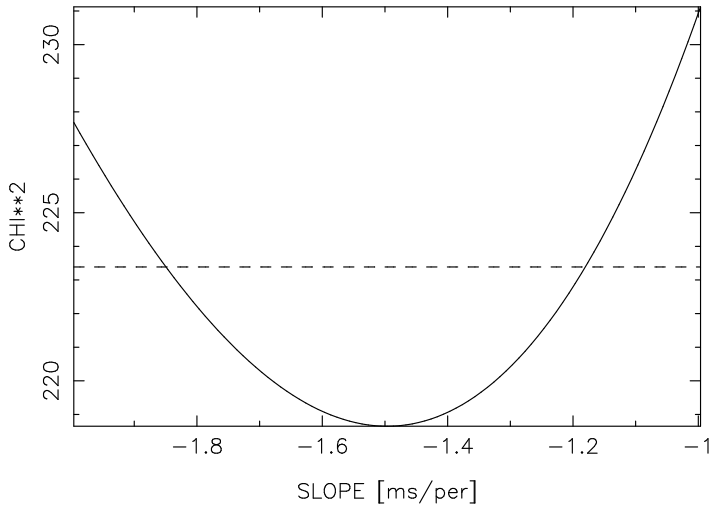

Figure 4.9: Plot of χ^2 as a function of Parameter A. The dashed line corresponds to an increase of χ^2 by one standard deviation and the range of A corresponding to the intersection of this line with χ^2 plot represents 68.3 percent confidence limit for this parameter. The error bars quoted in the text were obtained from similar curves

This expression is a modification of the definition of χ^2 given in Appendix A.1. The denominator in Equation 4.11 represents the variance of the linear combination $P_{2_i} - A\alpha_i - B$ of the two random variables P_{2_i} and α_i.

The occurrence of A in the denominator in Equation 4.11 makes the resulting equation for the derivative of χ^2 with respect to A nonlinear. A scheme to minimize the χ^2 iteratively was used to obtain fitted parameters. The χ^2 curve was plotted for different values of A and B. The confidence limits on the parameters are the values corresponding to χ^2 one standard deviation away from the minimized χ^2. As an example, the χ^2 for the fit to P_2 data is shown in Figure 4.9 for this range. The errors quoted below were estimated from such plots.

The fit to the data excluding the isolated slope at -19.503 ms period^{-1} is shown in Figure 4.8 by the dashed line with a less steep slope, where $A = -1.5 \pm 0.3$ and $B = 39.6^{+2.3}_{-2.5}$ with a χ^2 of 213 for 274 degrees of freedom. Including the isolated slope does not change the parameters significantly with the χ^2 increasing marginally to 218 for 275 degrees of freedom. The fit to 208 slopes in the Class B drift mode ($-10.0 \leq \alpha < -5.4$) gives $A = -4.1^{+0.8}_{-1.0}$ and $B = 20.2^{+5.7}_{-7.4}$ with a χ^2 of 70 for 206 degrees of freedom, which is significantly different. This fit is indicated by the dashed line with a steeper slope in Figure 4.8.

The data were also fitted to a line with zero slope. The χ^2 values change from 213, 218 and 70 to 344, 344 and 216 for the above mentioned three fits respectively indicating that these are clearly bad fits. Thus, the subpulse separation, P_2, increases monotonically with the modulus of drift rate, α.

4.3 Conclusion

The average properties of the subpulse belonging to a given drift band were investigated. While the average subpulse energy and the RMS deviation of subpulse position from that predicted by the slope of the drift band are higher for the dominant drift mode (Class B), the subpulse width is observed to be independent of drift rate. At the same time, the subpulse separation, P_2, increases monotonically with the modulus of drift rate, α, contrary to popular belief. It appears that the subpulse energy and average subpulse separation are possibly related to the process responsible for drifting subpulses, thus providing two independent constraints for the theoretical modeling of this physical process.

Chapter 5

Drift mode separated Integrated profiles of PSR B0031−07

Although the phenomenon of subpulse drifting represents the dynamics of pulsar radio emission, it is also sometimes reflected in the kinematics of the pulsar beam. Previous studies indicate that the changes in the integrated profile of some pulsars are accompanied by a change in the subpulse drifting. Although PSR B0031−07 does not show such profile changes in the canonical sense, it is interesting to examine whether the pulses corresponding to different drift rates add to different profiles. This question has been addressed in this chapter.

The integrated profile of some pulsars has two or more stable forms (Bartel et al. 1982). Such pulsars often show an alternative form of the profile for several periods before reverting to its usual stable form and this phenomenon is termed as mode-changing. Such behaviour is accompanied by changes in drift behaviour for some mode changing pulsars such as PSR B0148-06 (Biggs et al. 1985b), PSR B1822-09 (Fowler, Wright and Morris 1981) and PSR B2319+60 (Wright and Fowler 1981a). With the exception of the last pulsar, mode-changing was first recognized as a profile change in these pulsars and any changes in the subpulse behaviour were noted subsequently in the context of different profiles. On the other hand, it is quite probable that changes in the drift patterns are more fundamental and profile changes are a secondary effect as in the case of PSR B2319+60 (Wright and Fowler 1981a). In this picture, the pulses belonging to different modes of drifting are expected to add to distinct integrated profiles. This proposition has been verified only on one pulsar (PSR B2319+60) till date to the best of our knowledge.

Since the integrated profile represents the average beam of the pulsar radio radiation, a change in the shape, the width and the position of the profile indicates a reorganization of the beam. Thus, the relationship of mode-changing with drifting provides important constraints for the mechanism which organizes the beam pattern. Moreover, this relationship is a link between the dynamics and the kinematics of the pulsar radiation. Since this thesis presents a study of the dynamics of the radio radiation of PSR B0031-07, this relationship was also explored in the case of this pulsar.

A behaviour similar to PSR B2319+60 was reported qualitatively for PSR B0031-07 by Wright and Fowler (1981b). They claimed that the integrated profiles are different in the three modes and differ in their widths. However, they do not show any figure to substantiate their claim. Since data with a large number of high sensitivity pulses on this pulsar were available to us, these differences in the integrated profile for different drift modes were investigated afresh and the results, which are broadly consistent with the above mentioned study, are presented in this chapter.

5.1 Method of analysis

The drift rates for the bands, identified in Section 3.3.3, were used to obtain the integrated profile of this pulsar for the three different drift modes. In order to do this, first the periods belonging to each drift mode were identified using these drift rates. Then, separate integrated profiles were obtained for each drift mode by averaging all its periods.

Often, a drift band belonging to a given drift mode is followed by one of another drift mode. It is necessary to separate such bands so that drift bands belonging to different drift modes do not occur in the same period. Otherwise, the resultant integrated profile will have contribution from both the drift modes. The drift bands were isolated for this and the other reasons mentioned in Section 4.1.1 in a manner similar to that described there. Briefly, the off-pulse mean was estimated for each period belonging to a given drift band and this was subtracted from the calibrated data. The expected position of the subpulse in each period was estimated from α obtained from the best-fit line to the drift band in consideration. The data within 30 ms of this expected position was retained and the rest of the samples were made zero. This particular range of samples was selected for the same reason as explained in Section 4.1.1, *namely*, P_2 has an average value of 50.81 ms for this pulsar.

The data was then corrected for the variation due to ISS. The mean energy in the on-pulse samples for a block of periods (typically 200 for this pulsars) was calculated from the calibrated data. One hundred periods, on either side of the period number at the center of each drift band, were included for this purpose. The on-pulse data was then scaled by this mean energy to equalize the increase or decrease in the radio flux of this pulsar due to ISS.

Each isolated subpulse was then displayed along with the best-fit line representing the drift band. All the periods belonging to this drift band were then added to get the accumulated profile for the band. Note that this averaging was carried out without aligning the subpulses. Thus, this profile represents the overall integrated pulse profile of the pulsar unlike those shown in Figure 4.1 which are the subpulse profiles averaged over a given drift band. The second moment of power in each sample of the profile was also obtained simultaneously.

Next, the drift rate of the band was used to decide its drift mode. The profile for the band under consideration was then accumulated in the profile for the respective drift mode. This profile for the band was also added to an overall integrated profile.

The data used in this thesis were acquired in several observations with a sampling time, which was not identical for all observations. Almost two thirds of data were acquired with a sampling time of 7.5 ms, while the rest were acquired at 5.5 ms and 6.0 ms. Thus, it is not possible to form the above integrated profiles by simply adding the profiles of each individual observation. At the same time, this is desirable as it is necessary to include as many periods as possible in obtaining these profiles. It is evident from Section 3.6 that the frequency of occurrence of Class A and C modes is much less than that of Class B mode. Hence, it is difficult to obtain sufficient periods in a given observation to obtain a stable profile for Class A and C and addition of profiles of individual observations is necessitated.

The profiles obtained for all the three drift modes in the individual observations (consisting of typically 1000 periods) were resampled to a common sampling interval of 5.0 ms by linear interpolation (Appendix D.1). Finally, the three drift mode profiles were obtained by averaging the resampled profiles of each observation. The error in the estimate of power in each sample of these profiles was also estimated simultaneously in the following manner. First, the variance of the power in each sample of the profile for the individual observation was calculated from the second moment of this power. Then, the variance of the powers in the resampled profile was calculated. The linear interpolation represents a sum of appropriate fractions of the energy in the samples of the original profile. These energies can be treated as random variables and the variance on the above sum can then be calculated in a straight forward fashion.

Thus, three integrated profiles corresponding to Class A, B and C drift modes of this pulsars were obtained. An overall integrated profile consisting of all the periods in the above three profiles was also obtained. The features of these profiles are discussed in the next section.

5.2 Results and discussion

The integrated profiles of PSR B0031−07 for the three drift modes are shown in the lower panel of Figure 5.1. One standard deviation errors are also indicated on these profiles. The drift bands with drift rates on the boundary of the definition of a drift mode class were not considered. Only bands, with α plus error as well as α minus error falling within the same drift mode, were considered (Class A : $-5.4 \leq \alpha < -1.7$ ms/per; Class B : $-10.0 \leq \alpha < -5.4$ ms/per); and Class C :$\alpha < -10.0$ms/per). Hence, only 2046 drift bands, which satisfied this criteria, have been used in this figure. The number of periods included for Class A, B and C mode were 4789, 14763, and 495 periods. The top panel shows the overall integrated profile of the pulsar.

The three profiles are significantly different from each other. The position, width and the amplitude of the pulse in a given drift mode can be estimated by fitting a Gaussian to the profile (the profiles are very nearly Gaussian). Each of the profiles in Figure 5.1 was fitted with a Gaussian in the least squares sense (See A.3 and A.4). Since the aim was to obtain a good estimate of these parameters, the fit was carried out in two steps. First, unity weights were assumed and a fit was

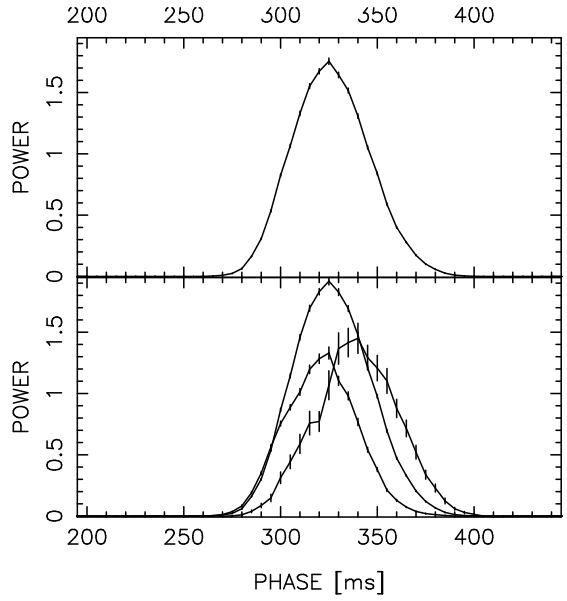

Figure 5.1: Integrated profile belonging to 2046 drift bands (top frame), and the integrated profiles separately in the three drift modes, from left to right: mode A ($-5.4 \leq \alpha < -1.7$ ms/per)); mode B ($-10.0 \leq \alpha < -5.4$ ms/per); and mode C ($\alpha < -10.0$ms/per)

S. No.	DRIFT MODE	α	L	M	N	χ^2
1.	A	-4.03 ± 0.05	1.29 ± 0.01	320.7 ± 0.2	26.6 ± 0.4	1.0
2.	B	-7.77 ± 0.04	1.93 ± 0.02	326.0 ± 0.2	28.6 ± 0.3	1.0
3.	C	-11.5 ± 0.1	1.41 ± 0.02	339.4 ± 0.4	30.6 ± 0.7	1.0

Table 5.1: Parameters of mode separated profiles from model fit

carried out. The mean square error between the data and the fitted model was then evaluated. In the second step, the inverse of this error was used as weights. A second fit was then carried out to estimate the parameters of the Gaussian. The parameters of the Gaussians in the two steps were found to be consistent for all the profiles indicating that the fits are reasonably good. At the same time, the second fit gives more realistic errors on these best fit parameters.

The parameters of best-fit Gaussian for each drift mode separated integrated profile are presented in Table 5.1. The fits themselves are shown in Figures 5.2, 5.3 and 5.4. It is once again evident from the Table 5.1 that the three profiles are significantly different.

The second point to note from Table 5.1 is that the three profiles do not arrive in phase if one considers the phase of the peak of the Gaussian as the position of the corresponding profile. This is also evident from Figure 5.1. The Class A profile arrives earlier than the Class B profile which arrives earlier than Class C profile (the phases of the peaks are $320.7 \pm 0.2 < 326.0 \pm 0.2 < 339.4 \pm 0.4$ respectively). This suggests that the pulsar beam shifts towards the trailing edge of the profile with respect to the drift mode or with increasing negative drift. A plot of this offset against the average drift rate for the drift mode is shown in Figure 5.5.

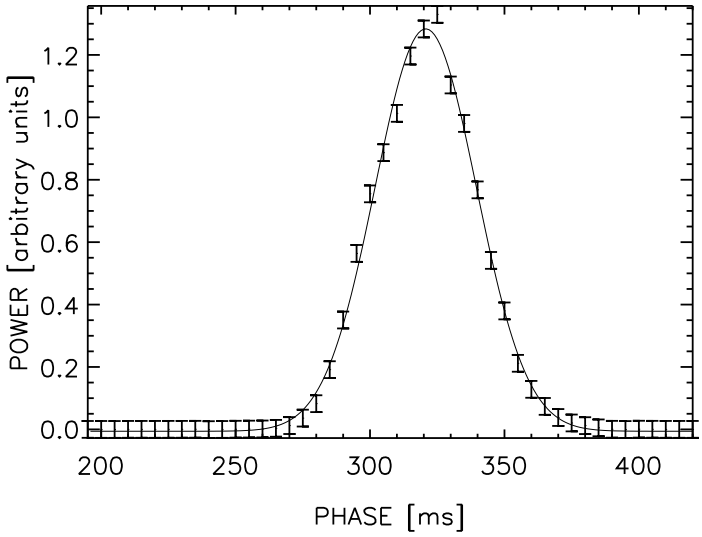

Figure 5.2: Gaussian fit to Class A ($-5.4 \leq \alpha < -1.7$ ms/per) integrated profile including 4789 periods. The error indicated are the mean square error between the data and Gaussian model, obtained in an earlier fit as explained in the text

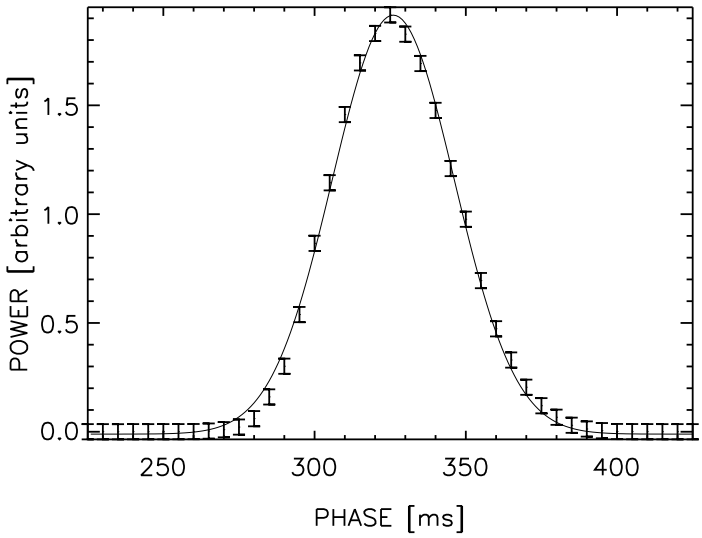

Figure 5.3: Gaussian fit to Class B ($-10.0 \leq \alpha < -5.4$ ms/per) integrated profile including 14763 periods

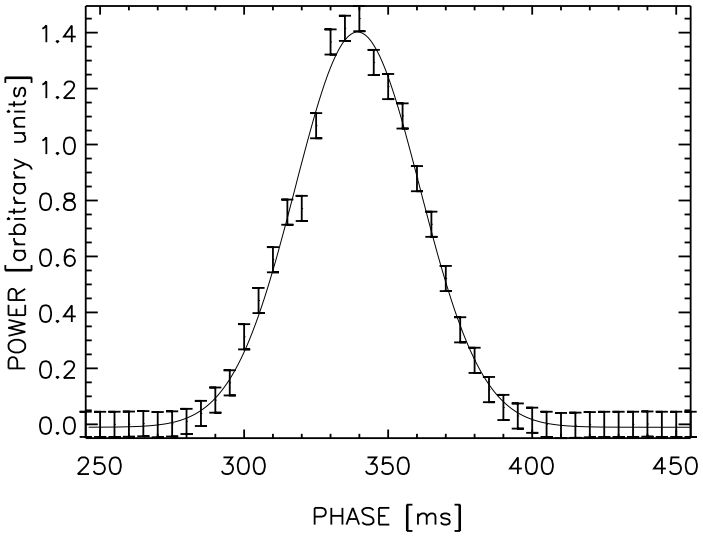

Figure 5.4: Gaussian fit to Class C ($\alpha < -10.0$ms/per) integrated profile including 495 periods

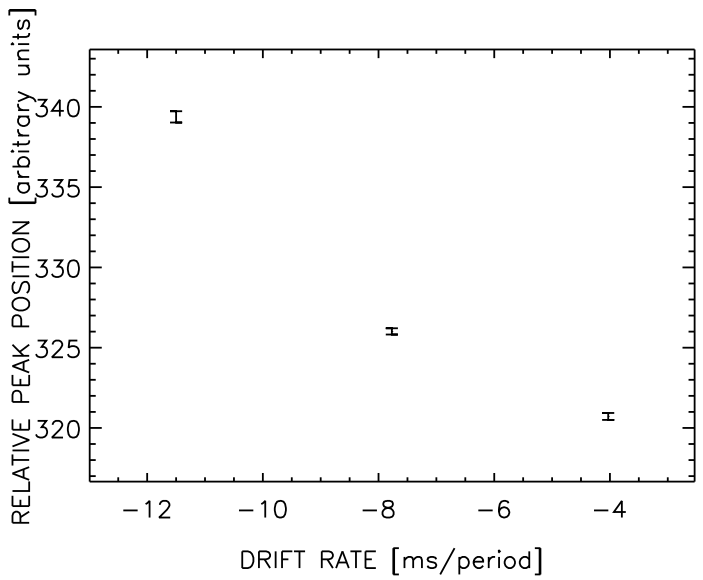

Figure 5.5: Plot of the phase offset of the peak of the mode separated profile as a function of drift rate, α

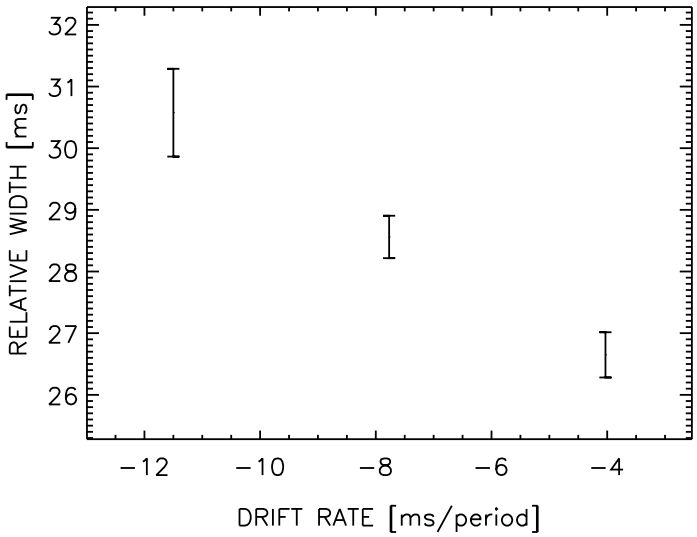

Figure 5.6: Plot of the widths of the mode separated profile as a function of drift rate, α

Not only the three profiles offset in phase, their widths are also different as can be seen from the RMS widths of the fitted Gaussians in Table 5.1. This probably explains the variation in the width of integrated profiles from one observing session to another where the drift modes are present in different proportions. The Class C profile is the widest of all followed by Class B and A profiles. The RMS widths are plotted against the average drift rate in Figure 5.6. The three profiles appear to be a scaled version of each other within the errors.

However, these results should be read with caution. ORT has a single polarization. Hence, the swing of polarization angle can potentially affect the shape of the profile. Consider a position angle sweep where the polarization of emission in the pulsar profile becomes progressively more aligned with the polarization plane of the telescope from the leading edge of the profile to the trailing edge of the profile as an example. In this case, the power in the trailing half of the profile will be larger than that in the leading half. This effect will therefore convert a truely symmetric profile to an observed asymmetric profile and will introduce systematic errors in the estimates given in Table 5.1.

However, if the polarization angle swing is independent of the drift behaviour of pulsar, the above source of error does not affect our results significantly. It is quite plausible that this is indeed the case as the polarization behaviour seems to be governed on an average by the magnetic field configuration of the polar cap. Moreover, the change of position angle is small over the entire profile in case of PSR B0031−07, so the profiles will not be significantly altered qualitatively. Lastly, these profiles were obtained by averaging individual pulses acquired over different epochs of observations. Now, the polarization of emission in the pulsar profile will have an orientation, which varies randomly with respect to the telescope for different epochs of observations due to differential Faraday rotation. Hence, a profile averaged over several observations is less likely to be affected by the single polarization nature of the data. Thus, the conclusion that the three profiles

are different is not affected strongly by this source of error. At the same time, the quantitative estimates given in Table 5.1 may not be very accurate in view of this systematic error.

5.3 Conclusion

Our analysis shows that the periods belonging to the three drift modes in PSR B0031-07 add upto different integrated profile. The three profiles appear to differ by a scaling constant. The average pulse for the three drift modes arrives progressively later in the on-pulse window from Class A to Class C drift mode. On the other hand, the RMS width of the average pulse decrease with the modulus of drift rate, α. The last two results should be interpreted with caution as our data are single polarization data.

Thus, a change in drift mode manifests itself as a modification of the overall beam pattern of this pulsar although this pulsar is not known to show distinct profile shapes unlike the usual mode-changing pulsars. These results indicate that the changes in drifting behaviour are more fundamental than the changes in the integrated profile. These results also suggest a possible change in the altitude of emission regions and this is discussed in Chapter 9.

Chapter 6

Drift independent properties of subpulse

The sequence of drifting subpulses indicate that the pulse emission of a drifting pulsar is organized in the form of a number of sub-beams within the integrated profile, which represents the average beam of the pulsar. The number and the shape of these sub-beams are important constraints on the emission mechanism of pulsars. It is also interesting to investigate the relationship between the energies of two adjacent sub-beams. The large number of high sensitivity periods enable us to carry out such a study for PSR B0031−07 and this is described in this chapter.

6.1 The sub-beam integrated profile

In this section, an integrated profile of the pair of drifting subpulses in PSR B0031−07 is obtained and the emission between the two sub-beams is investigated. The shape of the sub-beams is modeled and their average separation is determined. The data is examined to obtain evidence for more than two sub-beams. First, the method of analysis is described followed by a discussion of the results.

6.1.1 Method of analysis

The sub-beams manifest themselves in the form of drifting subpulses in a drifting pulsar. The structure of the sub-beam pattern in an averaged sense can be determined by obtaining an average profile of subpulses after removing the drift of subpulses as described in this section.

The intensity of the subpulses varies from period to period due to their phase in the integrated profile as well a due to inter-stellar scintillation (ISS), which is the dominant effect. A small degree of variation is possibly due to intrinsic pulse to pulse fluctuations also. The effect of these variations on the sub-beam pattern can be minimized by averaging the subpulse pattern over several number of periods and this was carried out after aligning the subpulse pairs for different

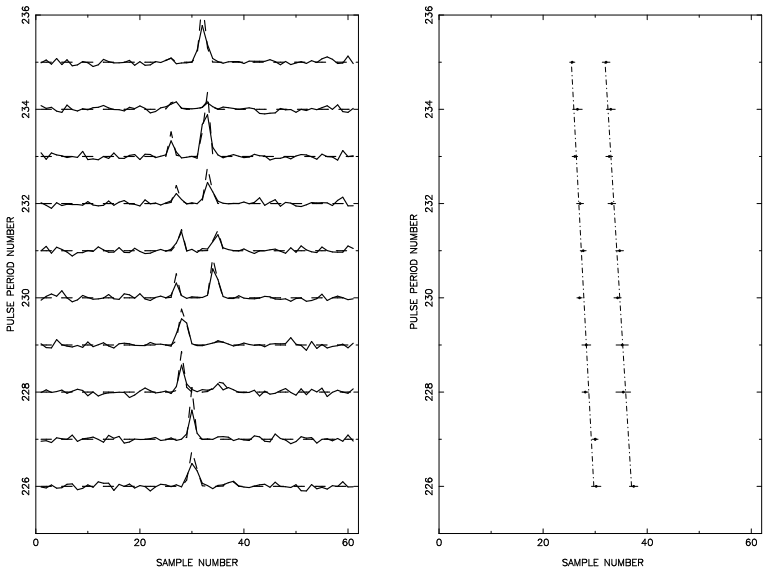

Figure 6.1: A typical pair of adjacent drift bands of PSR B0031-07 observed on 10 June 1995. The left frame shows the pairs of drifting subpulses for ten consecutive periods. The raw data is shown by the solid lines and the modeled subpulses by dashed lines. The right frame shows their mean positions along with error bars, and the best fit line (dashed) through each drift band. Data of each period were shifted so that the point midway between the dashed lines is aligned. The on-pulse window is from samples 23 to 41 (inclusive); the rest of the data belongs to the off-pulse window. The sampling interval is 7.5 ms

periods.

First, the raw data were read and the off pulse RMS and mean were calculated for every period. A sequence of periods observed on June 10, 1995 are shown in Figure 6.1 and the off pulse RMS and mean in each period correspond to the RMS and mean of the data between sample number one to twenty-two and forty-two to sixty-four. The off pulse mean was subtracted from the raw data in each period and the data in all the samples for the period were scaled by the off pulse RMS. This takes care of any gain fluctuations of the telescope from period to period. The scaled data is then equivalent to the data obtained from a telescope of constant gain.

Then the data were corrected for ISS. The pulse intensity varies due to ISS on a typical time-scale of 100 to 200 s or 150 periods for this pulsar. Therefore, the pulse energy can be equalized for different blocks in the data by scaling it with the average energy for a block of periods. This was calculated by adding the energies in the samples falling within the on-pulse window for all periods in a given block of 150 periods. The samples corresponding to the on-pulse window were then scaled by this normalizing constant for each period in the data. Note that the previous correction, which takes care of the gain fluctuations of the telescope, was applied to all the samples in a given period, whereas the above scaling is carried out on the samples corresponding to the on-pulse window only. This ISS corrected data was also used in the analysis of Section 6.2.

Then, the subpulse pairs for different periods were aligned to a reference phase. The method

of this section relies on the modeled subpulses, obtained in Chapter 3, along-with their identified drift bands to align the subpulses in the raw data. The estimate of the position of every subpulse in the raw data is given by these modeled subpulses. Further, a subpulse in the raw data can be associated with a given drift band using the identifications carried out in Chapter 3. This information was used to extract periods common to pairs of adjacent drift bands from the data and to associate the subpulses with each drift band.

Next, the periods common to each of these pairs of drift bands were displayed. An example is shown in Figure 6.1. The left panel of this figure shows a plot of common periods for two drift bands. The raw data are plotted as solid lines and the modeled subpulses are shown in this panel as dashed lines. The positions of the subpulse in each period, estimated using the modeled subpulses, are indicated along with the error bars in the right panel of this figure. In some cases, some common periods, such as period 227 in Figure 6.1, had only one subpulse. In such case, the association was decided by examining the data visually on plots such as the one shown in Figure 6.1.

All the common periods belonging to these adjacent drift bands were fitted with two lines in the weighted least squares sense using the error on the position as the weights and the slope and the offset of this line was obtained. Now, the slope of each line, indicated by dashed line in the right panel of Figure 6.1, gives the drift rate of the relevant band. For this analysis, a pair of adjacent drift bands was selected by using the following criteria

1. there be at least three periods common to the two adjacent bands
2. the drift slopes of these bands be consistent, i.e., the difference between the two values of the drift rates is less than the error on this difference

Due to this selection criteria, only 222 of 3481 drift bands in our data were included for the succeeding analysis.

Then, a midpoint between the pair of drifting subpulses was calculated for every period common to the two drift bands in the following manner. The slope and the offset of these two lines representing the respective drift bands were used to estimate the position of the two subpulses for every common period. These estimates are represented by the intersection of the fitted lines with the baseline corresponding to each period in Figure 6.1 and are given by

$$Y = C_0 + C_1 x \tag{6.1}$$

where,

C_0 = phase offset of the fitted line for the band

C_1 = slope of the fitted line for the band

x = pulse number

The phase of the midpoint between the pair of subpulses, given by half of the sum of the position of the two subpulses,

$$Z = \frac{1}{2}(Y_1 + Y_2) \tag{6.2}$$

was used for aligning the respective periods.

The data in every common period was aligned to a reference phase using a Fourier technique as described below. The phase offset of the midpoint from the reference phase was calculated for each common period. Now, a phase shift in time domain is equivalent to a multiplication by a linear phase gradient in the frequency domain. Hence, the Fourier transform of the data in each period was calculated and multiplied by the required phase gradient implied by the phase shift calculated above. The aligned pulse was then obtained by simply taking the inverse Fourier transform of this product. A mathematical description of this technique is given in Appendix B.1.

Finally, an integrated profile of the aligned pair of subpulses was obtained by adding all the periods of the selected drift bands. A total of 3909 periods were included in this analysis. Of these 2416 periods were acquired using a sampling time of 7.5 ms. The rest were acquired using a sampling time of 5.5 ms. The latter were resampled using a Fourier technique described in the Appendix B.2. Briefly, the spectrum of the data for each period belonging to the latter group was expanded by a factor of 11 by interpolation in two steps. First, the data were padded with 10 zero samples between each sample of the original data and its Fourier transform was computed. Then, the spectrum was multiplied with a low pass filter and its inverse transform was obtained. Finally, the data so obtained was decimated by 15 by picking up every 15th sample. The decimated data thus has a sampling rate of $5.5(15/11) = 7.5$ ms. The resampled periods were then accumulated in the usual fashion with periods at 7.5 ms to obtain the integrated profile of the pair of drifting subpulses.

6.1.2 RESULTS AND DISCUSSION

The drift removed integrated profile of the pair of drifting subpulses is shown in Figure 6.2. Note that this profile is very different from the usual integrated profile of the pulsar, which is shown in Figure 2.2. While the latter is a manifestation of the average beam of the pulsar, the drift removed integrated profile of the pair of drifting subpulses represents the average sub-beam pattern observed for this pulsar. In order to avoid confusion, it is called average sub-beam profile in this thesis. In this section, the features of this profiles are studied.

The profile has two prominent peaks, corresponding to the two drifting subpulses usually seen in the raw data for this pulsar. At first glance, There appears to be little evidence of a third subpulse or a fourth sample from this profile. Now, a data point of this profile is given by

$$P_i = \frac{1}{N}\Sigma_{j=1}^{N} p_{ji} \tag{6.3}$$

where, N is the total number of periods (3909) used to obtain the integrated profile, i is the i^{th} sample in a given period and p_{ji} are the powers in each period. The RMS of the off-pulse samples, *i.e.*, samples one to twenty-two and samples forty-two to sixty-four, was normalized to 1.0 for every period as described in the last section. Hence, the RMS of off-pulse data for the sub-beam profile is expected to be $1/\sqrt{3909} = 0.016$. The data in the off-pulse samples in Figure 6.2 has a

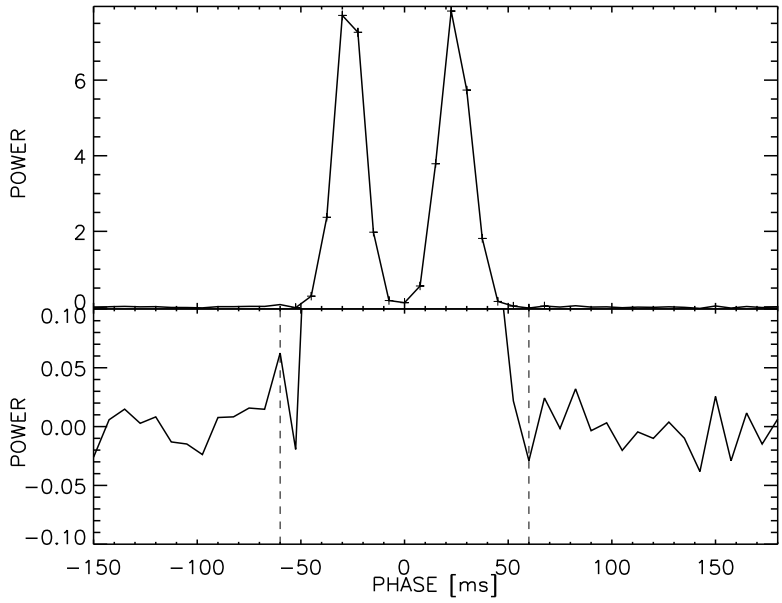

Figure 6.2: Top frame shows the average sub-beam profile of the drift removed subpulses, aligned such that the mid point between the two drift bands falls at the phase 0.0. The bottom frame is an enlarged version of the former, focusing on the noise in the wings

mean value of 0.0002, while its RMS deviation is 0.016 as expected. The highest and the second highest values in the off-pulse samples occur at sample 42 and 51 respectively. These are 0.03 and 0.026 respectively which are of the order of the RMS deviation cited above indicating the absence of additional subpulses.

The average sub-beam profile in Figure 6.2 within the dashed lines (phases between -60.0 ms to +60.0 ms) was fitted to different functional forms to study the shape and separation of the sub-beams. These data are best fit to a model of the following form

$$f(x) = A \exp\left(-\left[\frac{x-B}{C}\right]^2\right) + D \exp\left(-\left[\frac{x-E}{F}\right]^2\right) + G \tag{6.4}$$

This function represents a model comprising of two distinct Gaussians and a constant. Such a fit is non-linear in nature and the technique used for such model fitting is briefly reviewed in Appendix A.3 (See also Appendix A.4). For details on the fitting algorithm, see Press et al. (1992).

The fitted curve is shown in Figure 6.3 and the fitted parameters along with their errors are summarized in Table 6.1. The χ^2 for the fit was 17 for 10 degrees of freedom.

The position of the two peaks are given by the parameters B and E and these were used to predict the position of additional subpulses in the wings of the profile. The consistency of these numbers was verified by two methods. Firstly, the profile was fitted to another model given by

$$f(x) = \frac{A}{[(x-B)^2 + C^2]^k} + \frac{D}{[(x-E)^2 + F^2]^k} + G \tag{6.5}$$

where k is a fixed constant and is not a parameter for the fit. The value of k used was 4.6, which was determined by fits to subpulse profile. This function represents a model comprising

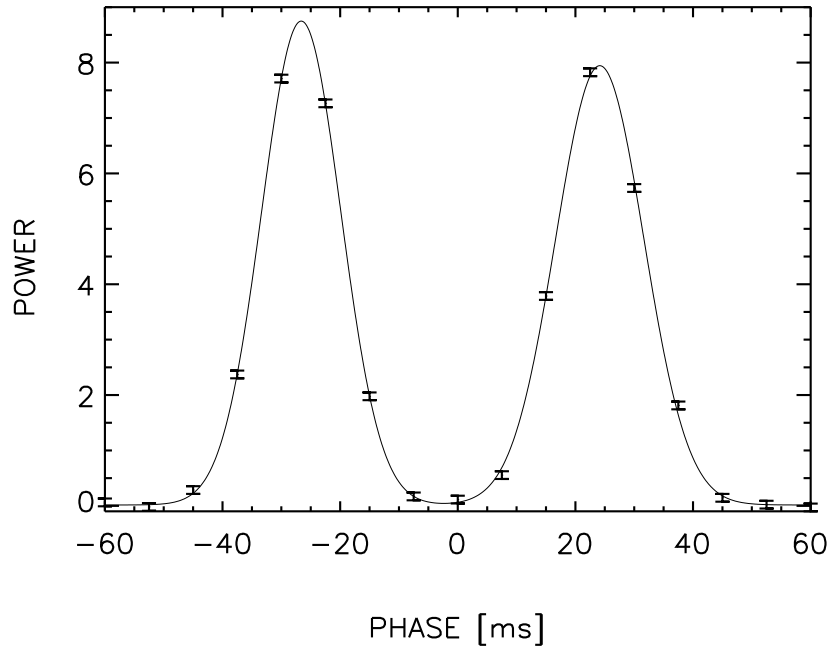

Figure 6.3: Fit to a Gaussian model, given by Equation 6.4, for the average sub-beam profile of the drift removed subpulses is shown by the solid line. The errors on the data were estimated by a similar fit with unity weights as explained in the text

PARAMETER	VALUE
A	8.7 ± 0.07
B	-26.62 ± 0.06
C	9.5 ± 0.1
D	7.93 ± 0.07
E	24.14 ± 0.07
F	10.6 ± 0.1
G	0.02 ± 0.03

Table 6.1: Parameters of Gaussian Model fit to average sub-beam profile

of two distinct Lorentzians and a constant. The χ^2 for the fit was 17 for 10 degrees of freedom and the values of the parameters B and E were -26.61 ± 0.08 and 24.2 ± 0.1 respectively, which are consistent with the values obtained from the earlier fit. Secondly, the value of the midpoint between the two subpulses is $1/2 \times (-26.6 + 24.1) = -1.24 \pm 0.09$, consistent with the absicca of the minimum of a parabola (-0.9 ± 0.3), which is fitted to the data between the two peaks in the profile of Figure 6.2 later in this section.

The average sub-beam separation, given by the difference of the positions of the two subpulses in the profile, is 50.81 ± 0.09. Hence, the third or fourth subpulses are likely to be found at the phase -77.38 and 74.9 ms. It has already been shown earlier that the energy in these samples is of the order of the RMS fluctuation of the off-pulse samples. One way to improve the sensitivity of detection is to add the energies in a few samples near the predicted phase of likely subpulses. The energies of likely third and fourth subpulses obtained by adding four adjacent samples near sample number 17 and 45 are 0.00 ± 0.01 and 0.007 ± 0.008 respectively, which are not statistically significant. Thus, there exists at least two sub-beams in this pulsars, but there is no evidence in an average sense for additional beams.

This result does not preclude the existence of such subpulses and it is probably due to a very low weighting of a subpulse at the edges of the integrated profile of the pulsar. Every period in the raw data was examined visually to look for additional subpulses. A third drifting subpulse was noticed in few periods in the raw data. Two examples are shown in Figures 6.4 and 6.5. The first figure shows four drift bands that commence and end at the period pairs (602, 611), (606, 619) (611, 624), and (618, 624), the last band continuing beyond period number 624. Periods 613 and 619 clearly show three subpulses. In period 619 the subpulse at sample 32, belonging to the principal drift band, has become weak, while the two adjoining subpulses have shown up stronger. The subpulses at samples 22 and 40 are the hitherto unseen subpulses; it is not surprising that such subpulses are difficult to notice, since they occur at the edge of the integrated profile. This data is not included in Figure 6.2 due to the stringent selection criterion.

Similarly, Figure 6.5 shows another example where three subpulses are evident. Again, the subpulse at sample 31, belonging to the principal drift band, has become weak, while the two adjoining subpulses have shown up stronger in period numbered 1314. This period was also not included in Figure 6.2 due to the stringent selection criterion. A handful of periods such as that exemplified by period 613 in Figure 6.4 were found after a careful scrutiny of almost 30,000 periods of data.

The peaks in the average sub-beam profile appear to be well separated with little emission between them. This emission can be estimated by modeling the curve between the two peaks. The seven data between the two subpulses were modeled by a function of the following form

$$y = a_0 + a_1 x + a_2 x^2 \tag{6.6}$$

A weighted generalized polynomial least squares fit was performed to obtain the values of the parameter a_0, a_1 and a_2 and their errors (See Appendix A.2 for details of least squares fit).

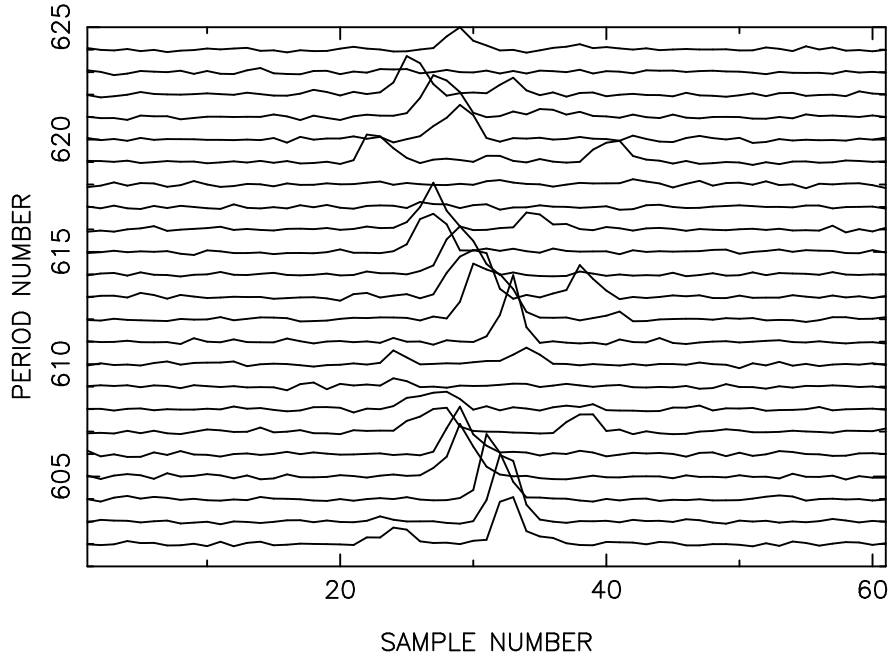

Figure 6.4: Data for twenty three periods of PSR B0031−07 obtained on 5 Dec 1993, using a sampling interval of 5.5 ms. The periods numbered 613 and 619 show three subpulses. The period number 619 illustrates the concept of competing drifting subpulses. The on-pulse window is from samples 18 to 42 (inclusive)

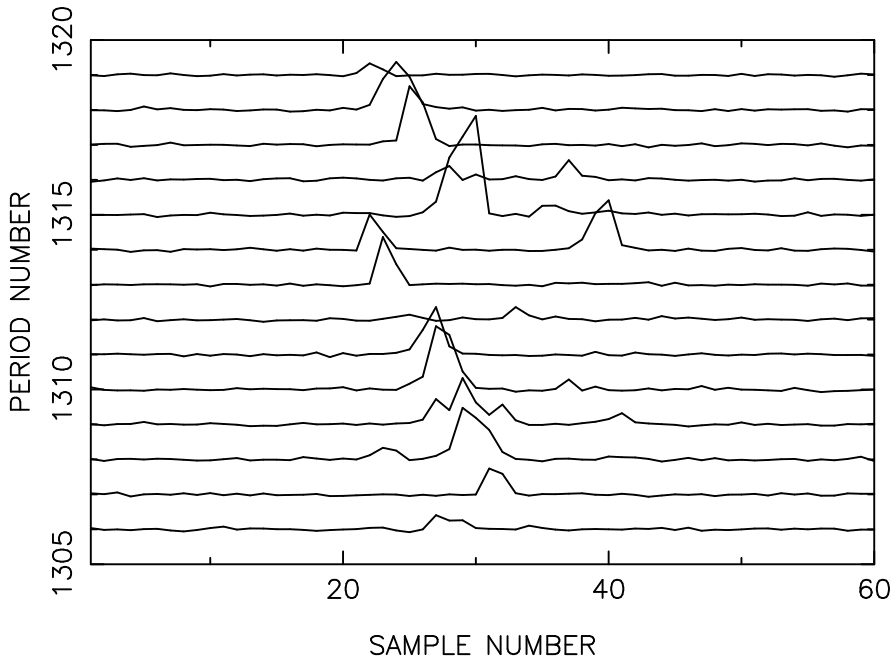

Figure 6.5: Data for fourteen periods of PSR B0031-07 obtained on 25 Oct 1992, using a sampling interval of 5.5 ms. The period numbered 1314 shows subpulse behaviour similar to period 619 of Figure 6.4. The on-pulse window is from samples 19 to 44 (inclusive)

The weights for this fit were determined as follows. For each data point in the profile, P_i, given by Equation 6.3, the RMS variation, σ_{P_i} over all the periods was also computed. At the same time, the energy in each sample of the profile can vary by an extent given by the RMS variation over the off-pulse samples in the profile. Thus, another estimate for the error on each data point is given by this RMS σ_P. Hence, the actual error cannot be greater than the square root of the quadratic sum of these two estimates, which was used initially to obtain the weights. However, the fits with these weights gave very large values of χ^2. This indicates that a second order polynomial is not a very good model. At the same time, the number of degree of freedoms limits a choice of a higher order model. Since the objective behind modeling the curve was to estimate the magnitude of the minimum between the peaks with its error, a second degree polynomial fit was forced nonetheless. However, the weights were calculated from the errors estimated using the model fit itself in the following manner. First the fit was carried out using unity weights. The mean square error between the model and the data for all samples was calculated from this fit and inverse of this value was used as weights. Finally, a second fit was carried out with these weights to obtain the parameters, a_0, a_1 and a_2. This procedure not only gives a more realistic fit to an *approximate* model, it also gives estimates of model parameter with a larger and conservative error bars. These conservative error bars in turn provide more cautious constraints on the emission between the two peaks given by the minimum of the parabola .

The data along with the fitted curve are shown in Figure 6.6. The errors shown in this figure have been obtained from the first fit as described in the last paragraph. The absicca and the ordinate of the minimum of this parabola, given by the expressions derived in Appendix C.1, are -0.9 ± 0.3 and -0.4 ± 0.2 respectively. The minimum of parabola is $0.4/0.2 = 2.0$ standard deviation away from the mean values of the off-pulse samples (0.002). These numbers are, therefore, not very inconsistent suggesting that there is no emission between the sub-beams. However, the error on the minimum value of the parabola, 0.2, is much larger than the RMS in the off-pulse samples, 0.016. Hence, this conclusion must be read with caution. In any case, the minimum value of the parabola is unlikely to be greater than the estimated value by three times standard deviation, which is $-0.4 + 3.0 \times 0.2 = 0.2$. On the other hand, this value is at least one-thirtieth of the peak value, which is 7.8. Thus, we conclude that the emission from the two subpulse is well separated, at least at the level of one thirtieth of the peak energy in the subpulses.

Thus, it appears that there exists at least three sub-beams in the pulsed emission of PSR B0031−07. These beams are separated on an average by 50.81 ± 0.09 ms in phase. The sub-beam shape can be represented either by a Gaussian or a Lorentzian beam. The sub-beams are well separated with the emission falling by at least a factor of thirty between the beams.

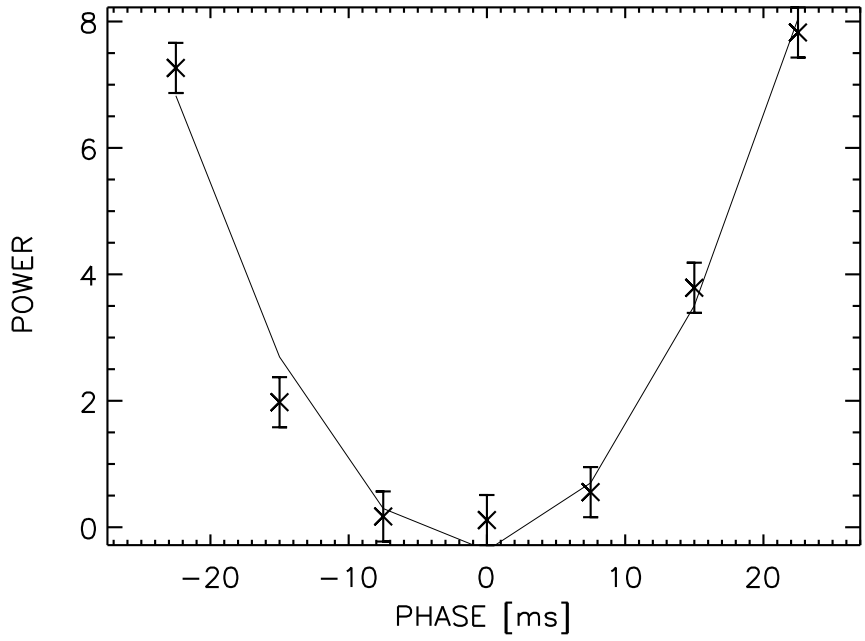

Figure 6.6: A second order polynomial fit to the data between the two peaks in the average subbeam profile of the drift removed subpulses is shown by the solid line. The errors on the data were estimated by a similar fit with unity weights as explained in the text

6.2 THE COMPETING SUBPULSES

One of the pair of drifting subpulse sometimes becomes stronger at the expense of the adjacent subpulse in this pulsar. This is evident from the period number 619 in Figure 6.4 as pointed out in the last section. The subpulse at sample 32 in this period is associated with the principal drift band and occurs at almost the center of the integrated profile. Yet, it has become weak, while the two adjoining subpulses in the wings of the profile are stronger. The period numbered 1314 in Figure 6.5 shows a similar subpulse behaviour suggesting that adjacent subpulses compete with each other. The above two examples were found after a careful scrutiny of almost 30,000 periods of data. This idea of competing subpulses is studied in greater detail in this section. The procedure followed for this analysis is described first followed by a discussion of the results.

6.2.1 METHOD OF ANALYSIS

The observed subpulse energies appear anti-correlated on a visual examination of several periods showing two subpulses. As a subpulse enters the trailing edge of the on-pulse window defined by the integrated profile of the pulsar, it is weaker in comparison with the preceding subpulse occuring at the center of the window. As the former shifts towards the center of the profile in the following periods, it gains in energy. At the same time, the latter weakens as it moves towards the leading edge of the on-pulse window due to its drifting motion. Thus, the observed subpulse energies are naturally anti-correlated due to the weighting of the integrated profile and depend on the phase

of the respective subpulse in the integrated profile of the pulsar. This is an observational selection effect which needs to be taken into account while studying the competing subpulses. The observed subpulse energy is normalized by the integrated profile weight associated with the subpulse for this purpose as described in this section.

The pulsar flux also varies due to inter-stellar scintillation as mentioned in Section 6.1.1. Apart from affecting the subpulse energy in different periods, this changes the energy in the integrated profile for different observing sessions. Thus, both the observed subpulse energies and the associated weights will vary over several periods due to ISS. Since the objective of this analysis was to compare the energies of the adjacent subpulses for a large number of pulses drawn from over 30,000 periods, it is also necessary to correct for this ISS related fluctuation.

First, the raw data were read and the off-pulse mean and RMS were calculated for each period. The mean was subtracted from the data and these were then scaled by the off-pulse RMS to take care of any gain fluctuations of the telescope as described in Section 6.1.1. Then, a correction for ISS variations was carried out by scaling the data samples in the on-pulse window by the average energy for a block of 150 periods. An ISS corrected integrated profile of the pulsar was then obtained by averaging the individual pulses over all periods in a given observation. As the ISS related variations have been removed, this profile is scaled to a fixed energy across several data files.

Then, this ISS corrected profile was used for calculating the weights for subpulse energy in the following manner. A pair of adjacent drift bands were selected based on the criteria of Section 6.1.1. The modeled subpulses obtained in Chapter 3.3.3 were used to estimate the position of the subpulses in the raw data for every period common to the selected adjacent drift bands. In general, this value lies between two samples, whereas the ISS corrected profile is known at the sampling instants only. Hence, the value of the integrated profile at the estimated phase of the subpulse was obtained by a linear interpolation between the adjacent samples. If the powers in the adjacent samples in the pulsar integrated profile are P_i and P_{i+1} and the phase of the subpulse is ϕ, then the interpolated weight is given by

$$w = [(i+1) - \phi]\, P_i + [\phi - i]\, P_{i+1} \tag{6.7}$$

As mentioned before, these weights are highly anti-correlated.

Next, the energies of the two adjacent subpulses were determined for every common period in the selected drift bands. The pair of subpulses in every common period was aligned at a reference phase as described in Section 6.1.1. The extent of each subpulse around the reference phase, which now represents the mid-point between the two subpulses (phase 0.0 ms), was noted from the average sub-beam profile of the Section 6.1.2. Thus, each subpulse in Figure 6.2 is defined by the samples between the phase 0.0 and the respective dashed line. The energy of each subpulse was then calculated by adding the energy in all the samples between these limits and multiplying the resulting number by the appropriate sampling time.

Finally, the energies for the two subpulses, e_1 and e_2, in every selected period were normalized

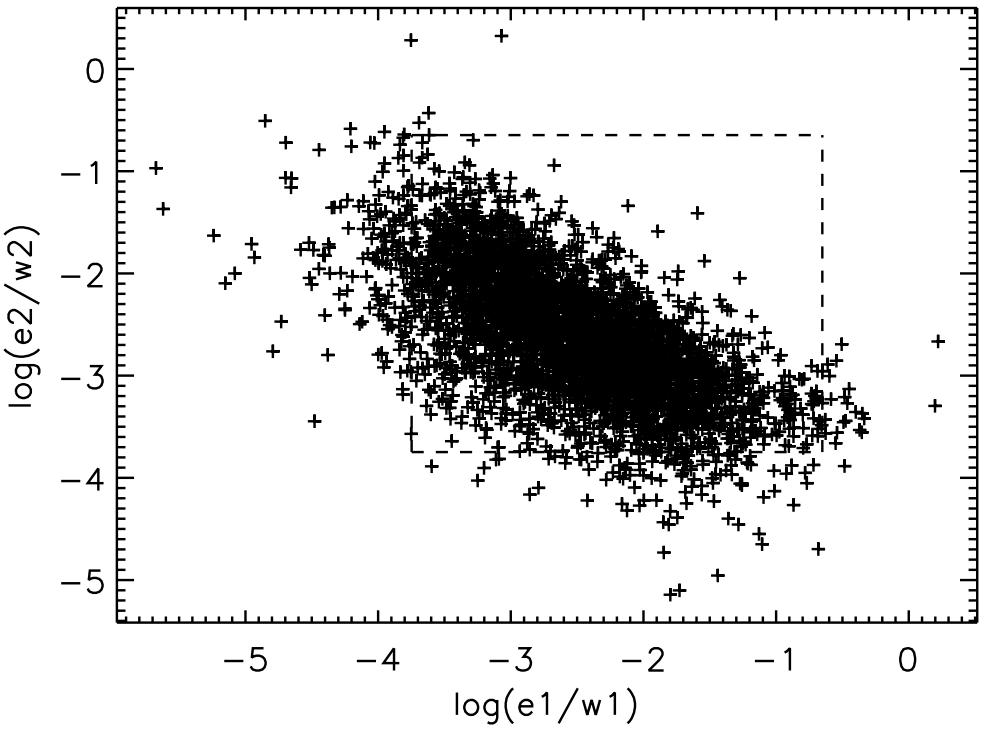

Figure 6.7: Plot of $\log_{10}(e2/w2)$ against $\log_{10}(e1/w1)$ for 3867 out of the 3905 periods of Figure 6.2. The box with dashed lines excludes some extreme data

by dividing it by its respective integrated profile weights, w_1 and w_2. The pairs of normalized subpulse energies, $(e_1/w_1, e_2/w_2)$, were then examined for anti-correlation as explained in the next section.

6.2.2 THE ANTI-CORRELATION OF SUBPULSE ENERGIES

A plot of the normalized subpulse energies, e_1/w_1, for the first subpulse versus that for the second subpulse, e_2/w_2, is shown in Figure 6.7 for 3867 periods. Logarithmic axes are used in this plot to highlight the anti-correlation, which is apparent in this scatter plot. Thus, the anti-correlation exemplified by the period number 619 in Figure 6.4 is exhibited by individual pulses on an average.

The normalized correlation coefficient, ρ, defined as

$$\rho = \left\langle \frac{\left[\frac{e1}{w1} - \left\langle\frac{e1}{w1}\right\rangle\right]\left[\frac{e2}{w2} - \left\langle\frac{e2}{w2}\right\rangle\right]}{\sigma_1\sigma_2} \right\rangle, \tag{6.8}$$

where $\langle ... \rangle$ is the mean value and σ_1 and σ_2 are the standard deviations of $\frac{e1}{w1}$ and $\frac{e2}{w2}$, respectively. It is -0.037 ± 0.023 for the entire data of Figure 6.7 (The error on ρ is derived in Appendix C.2). The dashed box in Figure 6.7 excludes 307 points (about 8% of the data) which are in the extremes. It is chosen by the criterion that both $\left[\frac{e1}{w1} - \left\langle\frac{e1}{w1}\right\rangle\right]/\sigma_1$ and $\left[\frac{e2}{w2} - \left\langle\frac{e2}{w2}\right\rangle\right]/\sigma_2$ be less than 4.5 in absolute value, and that both $\log_{10}(e2/w2)$ and $\log_{10}(e1/w1)$ be greater than -3.75; the value of ρ is not sensitive to small changes in these parameters. The ρ for the data within the box is -0.163 ± 0.023, which is significantly less than zero. Clearly the above anti correlation is not due to

the extreme data in Figure 6.7. In fact, ρ for the data outside the box turns out to be -0.08 ± 0.07, which means that the extreme data are actually reducing the absolute value of ρ. These numbers have been carefully verified. For example, by excluding merely four extreme data, ρ changes from -0.037 to -0.114, mainly because σ_1 changes from 0.049 to 0.033 and σ_2 changes from 0.049 to 0.019. The Spearman's rank correlation coefficient was -0.66 for the data in the box in Figure 6.7, while the Kendall rank correlation coefficient is -0.51. The data within the dashed box sampled at 5.5 ms gives $\rho_{5.5} = -0.231\pm0.033$, while that sampled at 7.5 ms gives $\rho_{7.5} = -0.137\pm0.031$. Thus the anti correlation $\rho = -0.163\pm0.023$ in the entire data is a genuine feature.

An important source of possible error in this section is the strong anti correlation of the weights themselves. If an error has been made in estimating the weights, could a residual small anti correlation remain in the normalized subpulse energies For example, an error in estimating the mean position of the subpulses could result in erroneous weights. This was investigated by simulations using the actual integrated profile of PSR B0031−07. The conclusions are that (a) random errors in positions of the subpulses will not result in the observed anti correlation of pulse energies, as is intuitively obvious, and (b) even by making a systematic error of one sample in estimating the RELATIVE subpulse positions, (which is highly unlikely) the ρ expected is $+0.03$, and it continues to be positive for several samples of error.

Hence, it is concluded that the energies of the pairs of drifting subpulses in PSR B0031−07 are indeed anti correlated.

6.3 CONCLUSIONS

The drift independent properties of the subpulses have been presented in this Chapter. The average sub-beam profile, obtained by averaging subpulse pattern over several periods after removing the subpulse drift, shows two prominent peaks. There is no evidence of any significant additional peaks in this profile. But, individual periods in the data exhibit at least three sub-beams indicating larger number of sub-beams within the pulsar beam.

The sub-beams represented by the two peaks in the average sub-beam profile are well separated. The emission between the sub-beams drops by at least a factor of thirty. This probably an upper limit as the errors in our estimation are much larger than the system noise. However, it is plausible that this emission is of the order of the system noise with the energy declining by a factor of 500. The average separation between two sub-beams is 50.81 ± 0.009.

The shape of an average subpulse can be modeled either as a Gaussian or a Lorentzian, both of which give reasonable χ^2. This validates the use of Gaussians to model the subpulses in Chapter 3.3.3. The error-bars on the average sub-beam profile do not permit a distinction between these two models.

The data exhibit few remarkable examples of competition between subpulse energies in individual pulses. Detailed analysis reveals that the energies of the adjacent subpulses normalized by the

respective integrated profile weights are significantly anti-correlated with a normalized correlation coefficient, ρ, of -0.16 ± 0.02.

These results provide useful constraints for pulsar emission models and are further discussed in Chapter 9.

Chapter 7

Variation of drift rate within the Integrated profile

Previous studies have indicated that the drift rate does not remain constant across the window defined by the integrated profile. Its variation appears to depend upon the geometrical arrangement of the emission regions and is useful in constraining it. This variation is best studied in pulsars which show organized drift such as PSR B0031-07 and such a study is presented in this chapter.

A variation in the drift rate as a function of phase or longitude within the integrated profile was first reported in pulsars such as PSR B1237+25, and B1919+21 by Backer (1973). He obtained the path of the drifting subpulses in these pulsars using Fourier analysis and concluded that these are S-shaped curves. Using a similar technique, Krishnamohan (1980) reported that the drift rate increases at the edges of the integrated profile in PSR B0031-07. Similar variation has been reported for PSR B0809+74 (Davies et al. 1984). All these investigations, except the last one, relied on fluctuation spectra which is an indirect method of inferring the drift path. This limitation was imposed by the lower sensitivity of the single pulse data available at that time. This also restricts the longitude range over which the drift rate variation can be studied. Moreover, these studies were based on a small number of pulses on each pulsar. In contrast, our high sensitivity data enables us to study the drift variation at the edges of the integrated profile and the shape of the drift band directly from the single-pulse data as described in this chapter.

Krishnamohan (1980) claimed that the observed variation with longitude is inconsistent with the polar cap model of the pulsar based on his data on PSR B0031-07. This interpretation of data was later contested by Wright (1981). He also related the geometry of the polar cap region to the observed variation, which can be used in principle to determine various parameters for this geometry. However, the measurements reported by Krishnamohan (1980), which were used by Wright (1981), had rather large error bars. Hence, this issue is examined afresh in this chapter with a view to obtain better constraints.

7.1 Two dimensional auto-correlation of the drift band

The variation in drift rate across the integrated profile in this pulsar can in principle be studied directly by modeling the shape of the drift band, as obtained from the positions of the subpulses belonging to it, by a higher order polynomial. In practice, this method does not yield significant results. Hence, an alternative method, based on an averaged two dimensional auto-correlation (TDACF) of drift bands, was used. This method, followed by the results obtained, is explained in the following section.

The TDACF method is superior to a direct modeling of the drift bands by a higher order polynomial because of the following three reasons. Firstly, at least eight to ten subpulses in a drift band are required to obtain a reasonable fit to a third order polynomial in the latter method, which reduces the number of drift bands which can be used in this method. On the other hand, majority of the drift bands in the data were used in TDACF method.

Secondly, the subpulses at the edges of the integrated profile are usually very weak. This limits the latter method to a range of phase in the integrated profile where subpulses with reasonable SNR are available. This range of phases can be extended by using an autocorrelation method. Any weak subpulse like structure is enhanced by an autocorrelation while it does not affect the noise. Thus, TDACF method is more sensitive to much smaller correlated flux buried in the noise at the edges of the integrated profile.

A third limitation of the polynomial fitting method is the poor sampling of the integrated profile window. As mentioned before, a typical band has seven to ten pulses which are just sufficient to model a cubic polynomial. Most of these are located in the central part of the window where the drift band is more or less linear. This leaves a much smaller degree of freedoms to model a non-linear curve, which is expected at the edges of the window. This limitation can also be overcome in an autocorrelation method by averaging the auto-correlation over several bands. Now, the subpulses provided by a large number of bands are distributed randomly in the integrated profile window. Hence, a much better phase coverage is obtained in the averaged auto-correlation over all these bands. Similar averaging is not possible in the polynomial fitting method.

7.1.1 Analysis procedure

This method uses the calibrated data, resampled to a common sampling interval. First the data associated with each drift band were isolated as a function of period number and phase in the window. Then, a two dimensional auto-correlation (TDACF) was obtained for this data. The drift mode for each band was identified and TDACF was adjusted to the average slope of the drift mode. Finally, adjusted TDACF was averaged over all the drift bands belonging to a given drift mode.

The first step in the analysis was resampling the calibrated data. The sampling time used in different observations varied from 5.0 ms to 7.5 ms. Since the variation of drift rate at the

edges is likely to be small, it was desirable to use as much data as possible for this analysis. This meant combining observations with different sampling times. Hence, the data was resampled to a common sampling time of 5.0 ms. Such resampling was carried out in an earlier chapter too (Section 5.1) and the same method of linear interpolation was used here (See Appendix D.1 for details on linear interpolation).

Next, the samples in the on-pulse window were extracted. It may be recalled that this range of samples was identified in the first phase of the data reduction (Section 3.3.2). The resampled data generally had larger number of samples than the calibrated data. Hence, the range of samples in the on-pulse window was appropriately scaled for the resampled data. The data within this range were retained for this analysis.

Then, the identifications of drift band carried out in the second phase of the data reduction (Section 3.3.3) were used to obtain the extent of each drift band in phase as well as in period number. The extent of the band in longitude or phase was defined by assuming that each drift band is spread over all the samples in the on-pulse window. In this way, the samples at the edge of the profile, which were of special interest for this analysis, are also included. The extent of the band in period number was then determined by using the slope or drift rate of the band estimated in Section 3.3.3. The period number at the start and the end of the band is given in terms of the drift rate, α , by

$$P_b = (\phi_e - \phi_o)/\alpha \tag{7.1}$$

and

$$P_e = (\phi_s - \phi_o)/\alpha \tag{7.2}$$

where,

P_b = period number at the start of the drift band

ϕ_e = last sample of the on-pulse window

ϕ_o = phase offset of the best-fit line for the drift band

α = slope of the best-fit line for the drift band

P_e = period number at the end of the drift band

ϕ_s = first sample of the on-pulse window

For clarity, these symbols are also indicated in Figure 7.1, where a drift band is schematically represented by the sloping dashed line.

The data samples corresponding to the phase and the period number identified above were extracted and the drift band in consideration was isolated in these samples. In this pulsar, a typical period consists of two subpulses. Thus, there often exists two drift bands in the same period. Since the primary aim of this analysis was to study the average shape of a *single* drift band, it was desirable to isolate each drift band in consideration. This was carried out using a method similar to the one used in Section 4.1.1 and 5.1, *namely*, retaining samples lying within

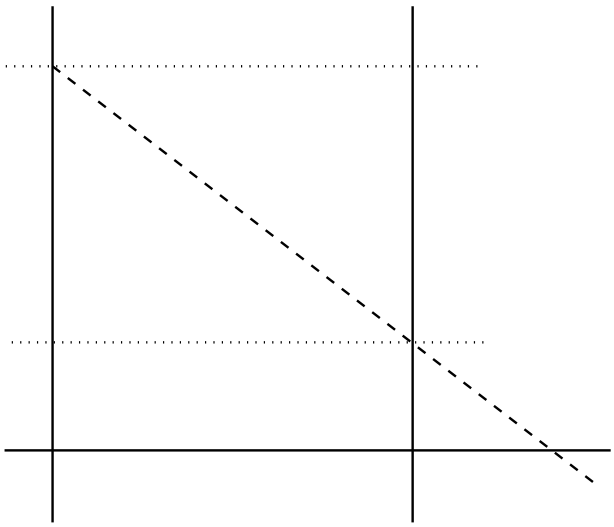

a

Figure 7.1: This figure illustrates the nomenclature used in the text in context of Equations 7.1 and 7.2. The two solid vertical lines represent the on-pulse window. The horizontal solid line represents the period number zero. The dashed sloping line is a schematic representation of a drift band. Its extent is defined by the solid vertical lines in phase and by the horizontal dotted lines in period number

22.5 ms of the expected position of the subpulse[a] from the calibrated data and making the rest of the samples zero.

The data in the isolated drift band were centered in a sixty-four by sixty-four point matrix by zero padding any location beyond those containing data points. This was desirable for two reasons. Firstly, the two dimensional autocorrelation uses the FFT algorithm. The length of the data array, for which the FFT algorithm works most efficiently, should be an integral power of two. Since a majority of drift band had typically ten to twenty pulses and typically thirty to fifty samples, the most convenient dimensions for the two dimensional data were sixty-four by sixty-four. Secondly, zero-padding the data around the centered drift band helps in reducing the influence of the edge effects of FFT algorithm on the TDACF.

This centered data for each of the drift band was displayed as a two dimensional phase - period number contour plot. Typical examples are shown in the leftmost panel of Figures 7.2, 7.3 and 7.4. The measured drift rate α for this band was also displayed by superposing it on the contour plot. The increase in drift rate at the edges of the on-pulse window is already evident from these plots. Each of the 3338 drift bands in the data were then examined visually to make a selection

[a]this position is obtained using the slope and the offset of the best-fit line for the drift band as explained in Section 4.1.1

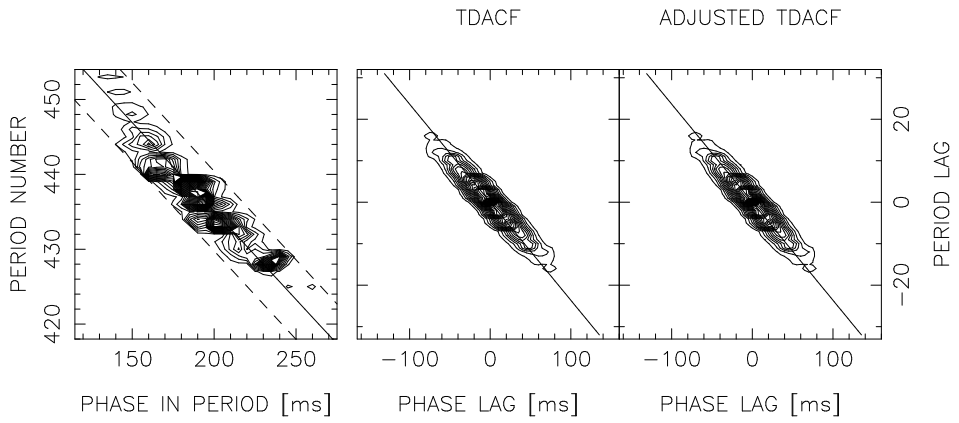

Figure 7.2: This figure illustrates the analysis procedure for a Class A drift band observed on March 11, 1996. The estimated drift rate for the band is -4.23 ms-period^{-1}. (a) The leftmost panel shows a contour plot of intensity as a function of phase in the integrated profile and period number. (b) The TDACF of this drift band is shown as a contour plot in the middle panel, where the phase lags and the period lags are along the X and Y axes respectively. (c) The rightmost panel shows the TDACF adjusted to the mean slope of the drift mode ($\overline{\alpha} = -4.05$ ms-period^{-1}) as described in the text

for this analysis. A drift band was selected if

1. the succeeding or the preceding drift band is not closer than the average subpulse separation, P_2.
2. there be at least seven periods in the drift band
3. the drift rate of the band along with its error lies within the drift rate limits for the drift mode in consideration

These criteria are elaborated further in the following paragraph.

There were instances in the data when the separation between two drift bands for some periods was much smaller than the nominal P_2 of 50.81 ms. In some cases, the two subpulses in a couple of periods, belonging to the two drift bands, were close enough to introduce spurious features in the auto-correlation. This usually happens when the pulsar makes a transition from one drift mode to another, such as a Class A to Class B transition. It is difficult to isolate such drift bands and these were ignored. Secondly, it was necessary that the subpulses in the drift band sample the on-pulse window sufficiently. In other words, there should be enough number of points in order to obtain a reliable shape of the drift band. The second criteria above enforces this by including only those drift bands which have at least seven periods. Finally, the shape of the drift band was studied separately for Class A and Class B drift modes by selecting the bands belonging to the respective mode. Class C bands usually have less than seven periods, so these were not included in this analysis because of the second condition. For the other two modes, drift bands lying on the boundary of a given drift modes were also not considered. This was ensured by including only

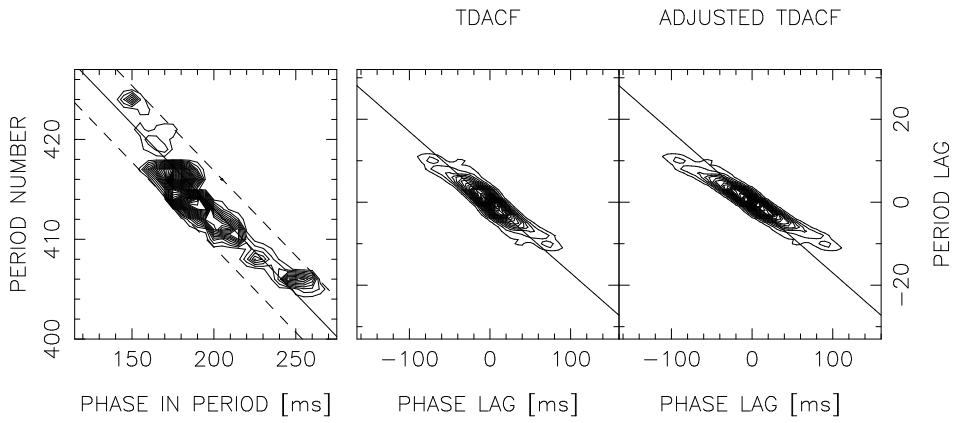

Figure 7.3: This figure depicts the contour plots similar to Figure 7.2 for a Class B drift band observed on March 11, 1996. The estimated drift rate for the band is -5.87 ms-period^{-1}. The mean drift rate,$\overline{\alpha}$, for this drift mode is -7.78 ms-period^{-1}

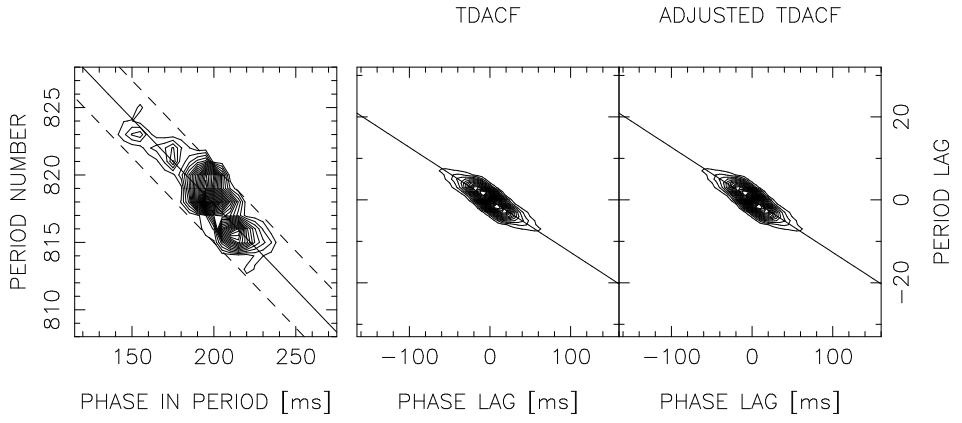

Figure 7.4: This figure depicts another set of contour plots similar to Figure 7.2 for a typical Class B drift band observed on March 11, 1996. The estimated drift rate for the band is -7.89 ms-period^{-1}. The mean drift rate,$\overline{\alpha}$, for this drift mode is -7.78 ms-period^{-1}

those drift bands for which $\alpha \pm \sigma_\alpha$ was within the following limits : (1) Class A - $-1.7 \leq \alpha < -5.4$ ms period^{-1}; (2) Class B - $-5,4 \leq \alpha > -10.0$ ms period^{-1}.

Next, the TDACF for the selected drift bands was obtained as described below. First, the mean of the two dimensional data was estimated and subtracted from the data. This removes a large peak at the zero period - phase lag, or the origin of the period number-phase lag plot. Then, a two dimensional hamming window, given by

$$W_{ij} = \left(0.54 - 0.46cos\left[\frac{2\pi i}{N}\right]\right)\left(0.54 - 0.46cos\left[\frac{2\pi j}{M}\right]\right) \tag{7.3}$$

was applied to the data. The application of this window improves the spectral estimation by reducing leakage from one frequency bin to other (Oppenheim and Schafer 1989). A good spectral estimation is important as it is used for obtaining the eventual TDACF. A two dimensional 64 point by 64 point discrete-time Fourier transform (DFT) of the windowed data was then calculated using a two dimensional FFT routine. Now, the DFT of the auto-correlation of a function is given by

$$F_{ac} = F_d F_d^* \tag{7.4}$$

where, F_{ac} and F_d are the two dimensional DFT of the auto-correlation and the function respectively, and * represents the conjugate of the transform. Therefore, DFT of TDACF was calculated from the above formula using the 64 by 64 DFT of the windowed data. The auto-correlation was then recovered by simply taking the inverse DFT. The TDACF of the typical drift bands, shown in Figures 7.2, 7.3 and 7.4, are shown in the center panels of these figures as contour plots of TDACF, plotted against the phase lags along the x-axis and the period lags along y axis.

Since the drift rate of each band is different, any nonlinearity in its shape in the auto-correlation will be wiped out by averaging this TDACF over all drift bands. Hence, TDACF of each selected drift band for a given drift mode was scaled by the average drift rate of the mode in the following manner. In principle, TDACF of each band can be rotated to match the average drift rate α for the corresponding drift mode. However, such a rotation changes the auto-correlation along both the period number and phase axis. If the slope of TDACF changes as a function of the phase lag, such a rotation does not preserve the magnitude of its change with respect to the phase lag. Since the goal of this analysis was to determine this change without distortions in an averaged sense, this method was not followed. Instead, TDACF was adjusted in phase lag by the difference in phase between the observed slope for the band in consideration and the average slope of the drift mode for every period number lag in the TDACF. This was accomplished by first sliding the coordinate point, (X_i, P_i) along the phase lag axis to (X_i', P_i) by this difference in phase, Δx, which was calculated from the observed position of the subpulse, x_o, and the position expected from the average slope of the drift mode, x_{me}, for every period number lag as given below

$$\Delta x = (\alpha_m - \alpha_o)\, P_{lag}(i) \tag{7.5}$$

where,

α_m = average drift rate for a drift mode (Class A / B)

α_o = observed drift rate for the drift band in consideration, .i.e, the slope of the best-fit line to the drift band

$P_{lag}(i)$ = i^{th} period number lag

The scaled TDACF for each period number lag at the required phase offset, Δx, was then determined at the new coordinate (X_i', P_i), by carrying out a spline interpolation in the old T-DACF. The method of spline interpolation is briefly reviewed in Appendix D.2. The original and the adjusted TDACF for the typical drift band, shown in Figures 7.2, 7.3 and 7.4, are plotted in the center and the rightmost panels of these figures respectively.

Finally, the adjusted TDACF of all bands belonging to a given drift mode were added to obtain the average TDACF for the drift mode. The locus of the peak of this averaged TDACF represents the average shape of the drift band for the given drift mode as a function of the phase lag. Any departure from linearity in this locus can be interpreted as a variation of drift rate and this is discussed in the next section.

7.1.2 Results and discussion

The average TDACF for Class A and B drift modes is shown in Figure 7.5. These figures have been obtained from 1930 drift bands in the data. Superposed on TDACFs are two lines corresponding to the average slopes for each of the drift modes as estimated in Section 3.3.3. The departure of the locus of peak of TDACF from these linear slopes is very evident for both the drift modes confirming that the drift rate increases at the edges of the integrated profile.

The average TDACF shown in Figure 7.5 was obtained from the calibrated data. Although the non-linearity of the drift band is evident qualitatively, it is difficult to carry out quantitative analysis on this TDACF as it suffers from two limitations. Firstly, the drift path indicated by it is less sharp at the edges than at the center. This limitation is obviously because the subpulses are weaker at the edges than in the center. The sensitivity of this method decreases at large phase lags especially since TDACF is expected to decrease at these phase lags by definition. Secondly, its quality is affected by pulse to pulse intensity fluctuation although some of this effect is taken care of by the process of averaging over several drift bands.

These limitations were taken care of by using the modeled subpulses as data instead of the calibrated data in the following sense. Every subpulse in the data was modeled as a Gaussian in Section 3.3.3 and the subpulse position was estimated from the centroid of this Gaussian. This information was used to create synthetic data in which the subpulses in every observed period were replaced by the modeled Gaussians at their estimated position. The effect of intensity and width variation in the data was eliminated by using Gaussians of unit amplitude and mean width of the subpulse (7.0 ms). Moreover, the off-subpulse samples were made zero in every period. In this way, a new data set, which preserves the subpulse positions while minimizing amplitude and width variations, was constructed from the calibrated data. Such modified data is better while using the

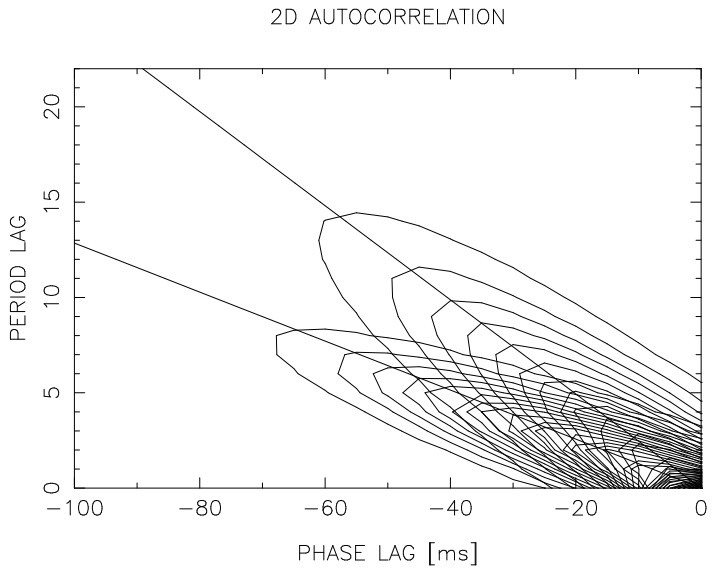

Figure 7.5: The averaged TDACFs for the calibrated data are shown as a function of phase lag and period number lag. The two families of contours represent the TDACF for Class A (265 drift bands) and Class B (1665 drift bands) modes. Class A contours have a smaller modulus of drift slope as compared to those corresponding to Class B mode

TDACF to probe the edges of the integrated profile. On the other hand, it might lose some details in the TDACF due to missing weak subpulses, which could not be modeled. The procedure of the last section was repeated on this synthetic data set to obtain its averaged TDACF, which is shown in Figure 7.6.

The essential result presented in this TDACF is similar to the one obtained from the observed (un-modified) pulsar data except that it is sharper than the latter. At the same time, it is more suitable to carry out the quantitative analysis described below. Hence, any reference to the TDACF in the following paragraphs implies the average TDACF of the *synthetic* data.

The coordinates for the peak of the TDACF in Figure 7.6 were obtained by fitting a Gaussian to the curve for each period number lag. These peaks, given by the centroid of the corresponding Gaussian, are plotted by crosses in Figure 7.7 for Class A drift bands and in Figure 7.8 for Class B bands. The curves traced by these points represent the average path of the drift band for the respective drift mode. A third order polynomial of the form

$$\phi = a_0 + a_1 P + a_2 P^2 + a_3 P^3 \tag{7.6}$$

was fitted to the data in these figures and these fits are shown as the superposed curves in these figures. The fitted coefficients are presented in Table 7.1.

It is evident from the figures and the table that the degree of nonlinearity is small, although significant at least in Class B drift bands. This is expected as the trajectory of the observer's line of sight is supposed to intersect the pulsar's emission cone tangentially. It is interesting to note that the coefficient of the cubic term is not significantly larger than its error for Class A drift

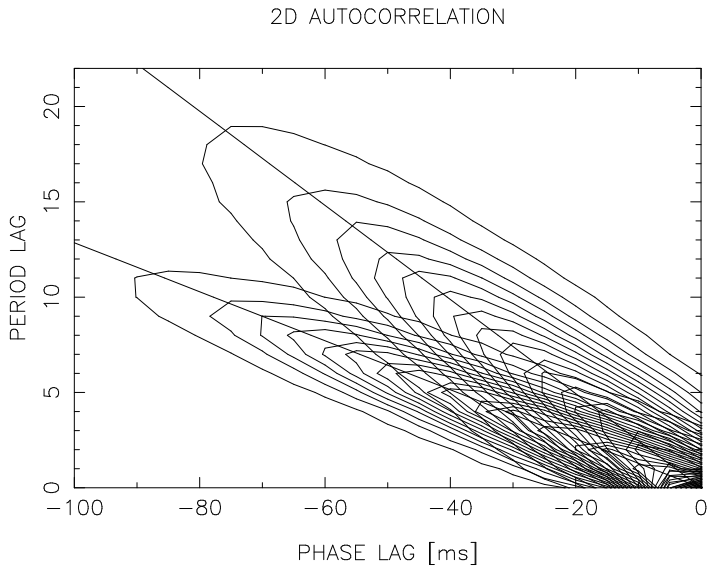

Figure 7.6: The averaged TDACFs for the data set obtained by modeling the subpulses by Gaussians of unit amplitude and constant widths located at the subpulse position as described in the text. These plots use the identical number of drift bands as in Figure 7.5

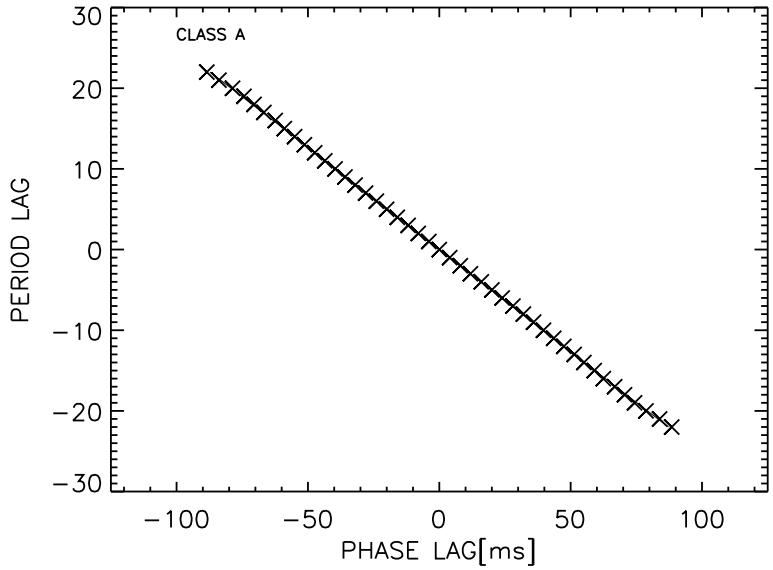

Figure 7.7: The average drift path for Class A drift bands obtained by fitting Gaussians to TDACF at each period number lag. The position of the peak of the fitted Gaussians are indicated by crosses. The superposed curve was obtained by a least squares fit to a third order polynomial to the data in the figure

Drift Mode	a_0	a_1	a_2	a_3	χ^2	DOF
Class A	0.0 ± 0.1	-3.93 ± 0.02	0.0 ± 0.0	$-7.2 \pm 4.4 \cdot 10^{-5}$	42	41
Class B	0.0 ± 0.2	-7.41 ± 0.05	0.0 ± 0.0	-0.0023 ± 0.0005	22	21

Table 7.1: Parameters for third order polynomial fits for drift path

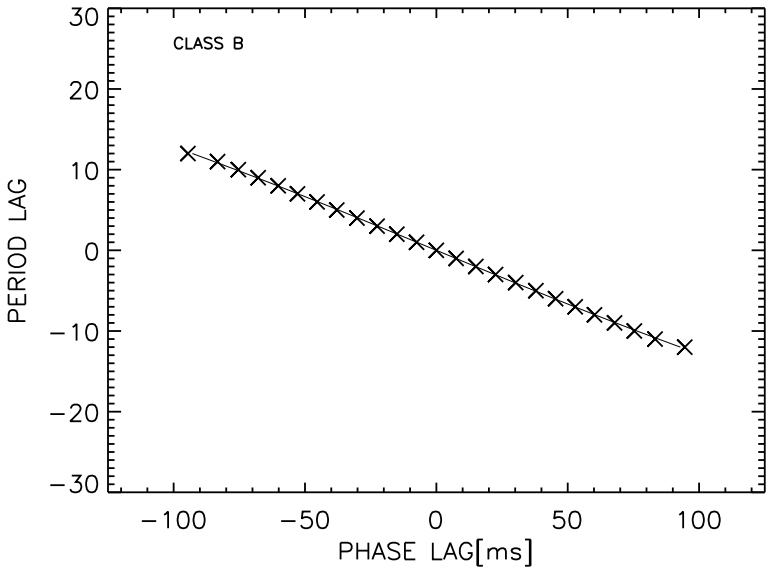

Figure 7.8: The average drift path for Class B drift bands obtained by fitting Gaussians to TDACF at each period number lag in a manner similar to Figure 7.7

bands, while that for the Class B bands is at least four times its error. Thus, the variation in drift rate across the on-pulse window appears to be larger for Class B mode than for Class A mode.

7.2 Conclusions

It was demonstrated in this Chapter that the shape of a drift band in PSR B0031-07 deviates from linearity at the edges of its integrated profile, where the drift rate appears to increase. The path of a drifting subpulse seems to be consistent with at least a third order polynomial for Class B drift bands whereas it is more or less linear for Class A bands.

This drift behaviour was shown to be consistent with Ruderman and Sutherland (1975) model by Wright (1981) and our results further support the geometrical arrangement of conal emission beams proposed in this model. A similar picture has recently been proposed by Gil and Sendyk (2000) based on independent arguments. These results are further discussed in the concluding chapter.

Chapter 8

The relationship between pulse nulling and drifting

The connection between the phenomena of "mode-changing" and "subpulse drifting" was examined in Chapter 5. In this chapter, the relationship between "drifting" and "pulse nulling" is explored. It has been reported in the past that the subpulse drifting is affected in a characteristic manner by nulling, although this has not been established unequivocally. These phenomena have been studied in a small subset of the total population of around 1300 discovered pulsars. Only a handful of these pulsars exhibit both drifting and significant pulse nulling. PSR B0031-07 is one such pulsar, which exhibits organized drifting as well as a significant degree of pulse nulling. Here, a study of the interaction between these phenomena in this pulsar is presented.

The best candidate for such a study is PSR B0809+74, which exhibits the most stable drifting among the observed drifters. This pulsar also exhibits nulls of duration ranging from one to forty pulses. Hence, this pulsar has been studied extensively in the past and the following is a brief account of the results of these studies. A significant reduction in the subpulse drift rate was observed in this pulsar immediately after a null (Cole 1970; Page 1973). Further investigations revealed that a phase jump occurs across each null; its magnitude is proportional to the duration of the null, implying that the subpulse ceases drifting during the null (Unwin et al. 1978). A later study indicated that, contrary to the above, some drifting does occur during a null; a sudden change of drift rate occurs at the start of a null, followed by an exponential relaxation to the normal drift rate, with the burst restarting when a fixed fraction of recovery has taken place (Lyne and Ashworth 1983). The magnitude of these events is proportional to the null duration. Thus, these studies indicated that the state of the process responsible for subpulse drifting is remembered across the null although this process is in some way disrupted by the onset of a null. Such studies may provide clues to the cause of pulse nulling phenomenon itself.

Another good candidate for such a study is PSR B1944+17. Although this pulsar does not exhibit a very organized subpulse drifting, it exhibits a large number of nulls as more than sixty

percent of its pulses are nulled pulses. Null durations themselves range from one to four hundred periods. Thus, it is a good candidate for a study of subpulse phase correlation across short as well as long nulls. However, the observations of this pulsar revealed a lack of correlation between turn-off and turn-on phases (the phase of the subpulse in the last period before the null and that in the first period after the null, respectively), implying no memory of subpulse phases across nulls contrary to the behaviour of PSR B0809+74 (Deich et al. 1986). Thus, the two pulsars, for which such a study was possible until recently, showed contradictory behaviour.

PSR B0031-07 presents the best combination of the behaviour of PSR B0809+74 and PSR B1944+17. It is the only other known pulsar apart from PSR B0809+74 which exhibits well organized drifting. It also nulls for about 45 per cent of time with durations ranging from one to several periods (Vivekanand 1995) and is similar to PSR B1944+17 in its nulling behaviour. Thus, it is an ideal candidate where a study of the interplay between nulling and drifting for a large number of null transitions[a] is possible.

An ideal way to study null-drift interaction in PSR B0031−07 would have been to repeat the procedure used by Lyne and Ashworth (1983) for PSR B0809+74. Since the latter pulsar has a very stable drift rate, the drift independent phase of the subpulse could be obtained by unwinding the effect of the drift using a fixed drift rate and a fixed P2[b]. PSR B0031−07 has a much more variable drift rate as well as a drift rate dependent P2 (Section 4.2). Therefore, the null-drift interaction in this pulsar has been investigated in the following sections using other methods.

In the next section, a study of the correlation of subpulse phases across nulls is presented and its dependence on the null duration is investigated. Then, the total drift during a null in this pulsar is discussed for the two drift modes.

8.1 Correlation of Turn-off and Turn-on subpulse phases across short nulls

A visual examination of data indicates alignment of drift bands across short nulls[c] implying some form of correlation between the turn-off and turn-on phases (Vivekanand and Joshi 1995) as is evident from Figure 8.1. However, the drift across nulls in this pulsar shows a lot more variation from one null transition to another unlike than in the case of PSR B0809+74. So, it is not possible to relate these phases by a deterministic relation for all null durations as was done in that pulsar. Instead, the distributions of these phases and their combination were examined statistically to test for a correlation between them.

The method followed to measure the turn-off and turn-on phases is described first in the next section. Then a description of the statistical analysis of these measurements is presented followed

[a] A null transition is defined as a change from burst to null state and vice versa

[b] P2 is the average phase difference between the pairs of drifting subpulses.

[c] Nulls of duration 1 to 4 periods are considered as short nulls while those with more than 4 periods are referred to as long nulls

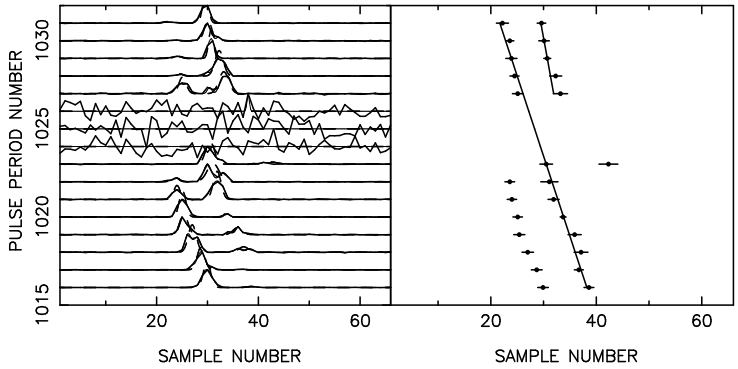

Figure 8.1: A burst-null-burst transition of PSR B0031−07, observed on 1996 March 11 suggesting phase correlation across a short null. The left frame shows pairs of drifting subpulses for 16 consecutive periods. The right frame shows their mean positions along with error bars, and the best fit line through each drift band (see Section 3.3.3 for details). The on-pulse window is from samples 19 to 41 (inclusive); the rest of the data belongs to the off-pulse window. The sampling interval is 6.5 ms. The power in null periods 1024 to 1026 appears enhanced in the left frame as the maximum powers in both null and burst periods have been scaled to unity.

by the results of this analysis.

8.1.1 Method of analysis

The correlation of subpulse phase across a null was obtained in three steps. First, the null and the burst pulses were identified in the calibrated data. For each null transition, the phase of the subpulse in the last period before a null (turn-off phase) and that of the subpulse in the first period after a null (turn-on phase) were determined. Finally, their correlation was examined using statistical methods.

The identification of null and burst period was carried out in the pre-analysis described in Section 3.3.2. Briefly, the on-pulse and the off-pulse energies[d] were obtained for all periods. Those periods with on-pulse energy below a threshold, defined as the sum of the mean off-pulse energy and 5 times its standard deviation, were considered as nulled periods. The rest were labelled as burst periods. These identifications were used in this analysis to extract pulses belonging to burst-null-burst transitions from the calibrated data for each observation. Two examples of burst-null-burst transitions are shown in Figures 8.1 and 8.2.

The drift behaviour of this pulsar is complicated due to the existence of three drift modes. Hence, it is desirable to select the null transitions on the basis of drift mode. Now, the mode of a null transition can be defined by the drift rate of the subpulses in the preceding burst. In Section 3.3.3, associations of subpulses, forming drift bands across several burst periods, were identified visually and straight lines were fit to these bands. The slopes of these lines give the drift rates of the bands in the burst preceding a null. These were used to decide the mode of the corresponding

[d]These are defined in Section 3.3.2

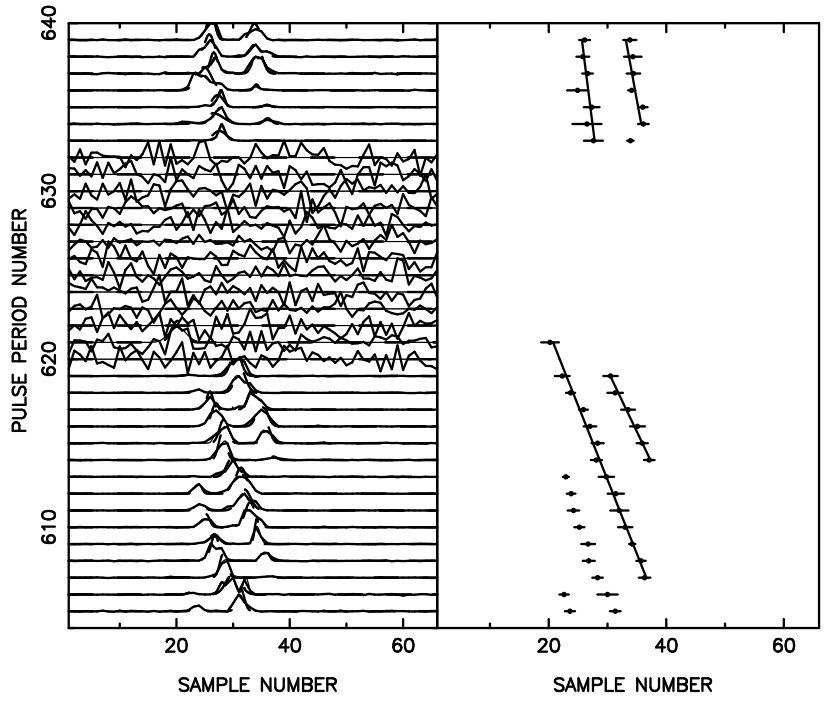

Figure 8.2: Another example of burst-null-burst transition of PSR B0031−07, observed on 1996 March 11. This figure is similar to Figure 8.1 and shows pairs of drifting subpulses for 35 consecutive periods

null transition and a selection was carried out as described below.

In this analysis, the null transitions in the two dominant drift modes (Class A : –4.0 ms period^{-1}; Class B -7.8 ms period^{-1}) were only considered as the third mode occurs rarely (Section 3.6). Some of these transitions were hybrid transitions in the sense that the drift rate in the preceding burst belonged to a drift mode different than that in the succeeding burst and this complicates the analysis. Hence, only those null transitions, which occur within the same mode, were included in this analysis. These transitions, constituting approximately 80 percent of the total transitions, were separated on the basis of the drift mode in the burst and are called Class A and Class B null transitions in this chapter. The phase correlation was then investigated separately for the two sets of transitions.

For each of these selected null transitions, the period number for the last burst period before the null as well as that for the first burst period after the null was noted. The turn-off and turn-on subpulses were identified in these periods in the following manner. First, all the periods in each burst-null-burst transition were displayed . Now, each period usually consists of a pair of drifting subpulses in this pulsar. If the turn-off and turn-on periods both have two subpulses for a null transition, there can exist four possibilities of choosing the turn-on and turn-off subpulse pairs. For short nulls, the slope of the drift band preceding the null or the phase of the subpulse in the turn-off period can be used to identify the correct pair of turn-on and the turn-off subpulses. However, there can be an ambiguity in correctly identifying this pair for long nulls during which

several drift bands could have occurred in principle. Hence, no a priori assumption about drift across nulls was imposed and subpulses entering the pulse window from the trailing edge for such nulls were also considered. All four possibilities were tried and it was observed that all give similar results. Hence, the rest of discussion refers to only one of the combinations in which the earliest subpulses in the turn-on and the turn-off period have been chosen. Although the typical drift in this pulsar is negative, the phase wrapping for long nulls implied in this procedure is reflected by some positive values for the total drift in our analysis.

Then, the phase of the turn-off and turn-on subpulses were obtained. As may be recalled, each burst period was modeled by one or more equivalent Gaussians representing its subpulses as described in Section 3.3.3, and each nulled period was represented by the absence of subpulses. The position of the turn-off and turn-on subpulses was obtained from the centroid of the Gaussians representing these subpulses in the modeled data and the RMS width of the Gaussian as the RMS error on this position.

These positions are in terms of the sample number of data in the integrated profile window. Now, observations on different days were carried out with different sampling intervals, which varied from 5.0 ms to 7.5 ms. Moreover, the integrated profiles of these observations are not aligned in general due to the limitations of data acquisition. Hence, the phase measurements in terms of absolute sample numbers cannot be combined over different observations. On the other hand, the number of null transitions are limited in an individual observations and it is desirable to club the measurements from all observations for the statistical analysis. Hence, these absolute position measurements in sample numbers need to be converted to phase measurements in units of time with respect to some fiducial point in the integrated profile.

This conversion was accomplished as described below. The peak of the integrated profile is usually considered a reliable fiducial point in pulsar literature, especially for pulsars such as PSR B0031-07 which exhibit a nearly Gaussian profile. Therefore, this point was taken as zero degree longitude or zero ms phase and all subpulse positions were measured relative to this reference point. First, the integrated profile for each observation, with typically 1200 pulses, was obtained by averaging all its pulses in the usual fashion. Then, the subpulse position in sample number, estimated from its modeled Gaussian above, was subtracted from the sample number of the peak of this integrated profile. Finally, these positions were converted to units of time (ms) by multiplying it by the sampling time for the observation.

These measurements of the turn-off and turn-on phases were then used to study the correlation between them using statistical methods as described in the next section.

8.1.2 Results and discussion

The observed distributions of turn-on and turn-off subpulse phases, obtained from the measurements described in the last section, are shown in Figure 8.3, where null transitions for all null durations of a given Class are considered together. The distributions for Class A and Class B

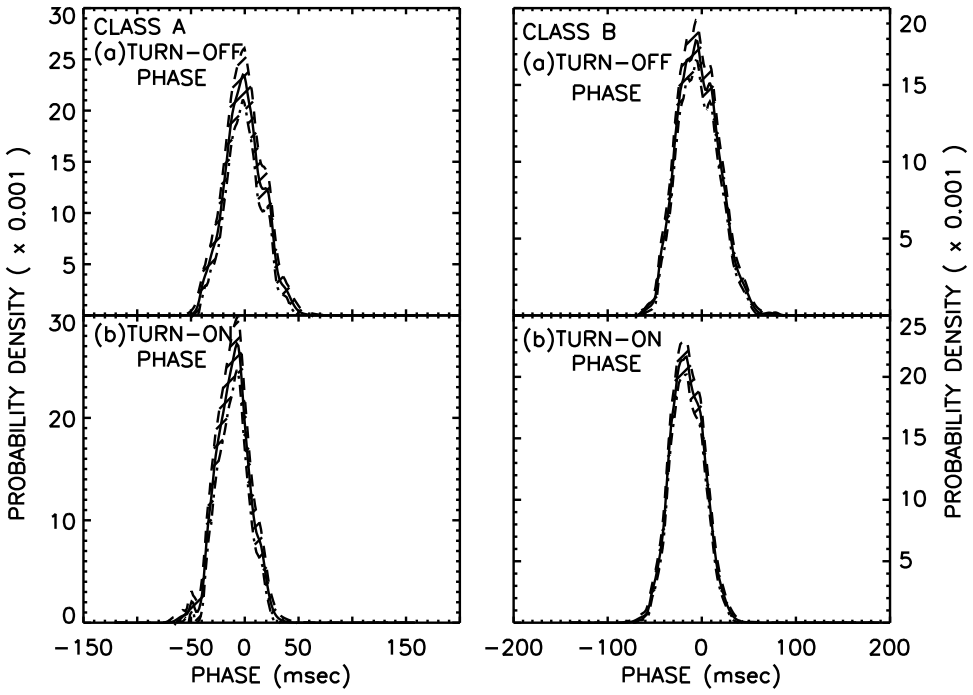

Figure 8.3: The figure shows observed distributions of turn-off and turn-on phase separately for the Class A and Class B null transitions. The distributions for the turn-off and turn-on phases for Class A transitions are shown in the top and the bottom frames respectively in the left half of the figure and those for Class B transitions are shown in the right half. The absicca of these figures have been scaled as indicated for better display. The cross hatched area indicates one standard deviation from the mean curve

transitions are shown separately in this figure. A total of 159 transitions were used to obtain the Class A distributions whereas the Class B transitions were obtained from 519 transitions. These distributions were then used to disprove the hypothesis that the turn-on and turn-off phases are not correlated as explained below.

Let the turn-on and turn-off phases be denoted by variables Y and X respectively and their respective probability density distributions by $P_Y(Y)$ and $P_X(X)$. The total drift across a null is given by

$$Z = Y - X \tag{8.1}$$

and its distribution is given by the joint distribution

$$P(Z) = P_{XY}(X, Y) \tag{8.2}$$

If there exists no correlation of the subpulse phases across nulls, the turn-on and turn-off phases can be considered to be independent random variables. In this case, Equation 8.2 reduces to

$$P(Z)\,dZ = \int_{-\infty}^{\infty} P_X(Y - Z) P_Y(Y)\,dY \tag{8.3}$$

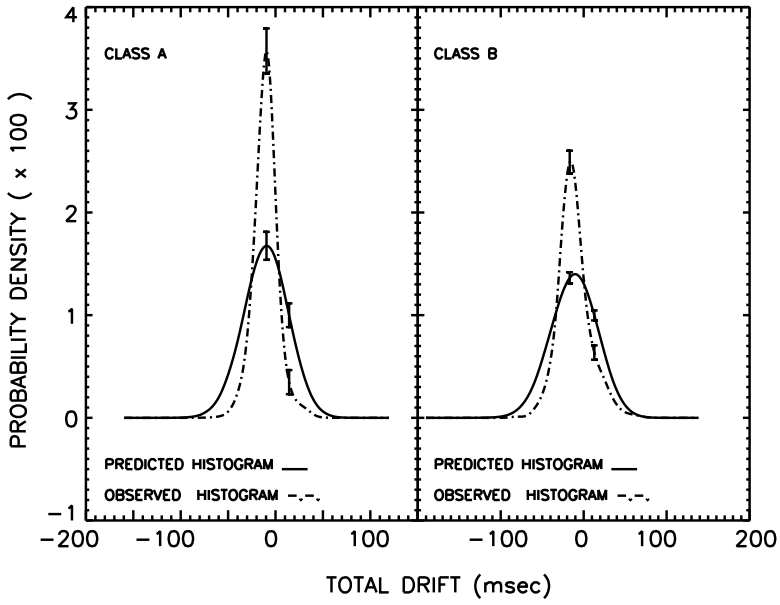

Figure 8.4: Probability density of total drift across null, i.e., difference of turn-on and turn-off phase(dashed dotted line) for the Class A (left frame) and Class B (right frame) null transitions. The predicted distribution, assuming there is no "phase correlation", is shown as solid line. One standard deviation errors for two points of worst case disagreement are also indicated. The distributions are peaked to the left of the origin as the total drift is negative.

Thus, the distribution of the total drift across the null is given by the cross-correlation[e] of the distributions of turn-on and turn-off phases in this hypothesis. Since the latter distributions were available from the data (Figure 8.3), the expected distribution for the total drift was obtained from these.

At the same time, the total drift across the null can be measured using Equation 8.1 from the measurements of the turn-on (Y) and turn-off (X) phases. The expected distribution obtained in the last paragraph can then be compared with the distribution of the measurements of total drift obtained using Equation 8.1. If these distributions are inconsistent, then the hypothesis used in deriving Equation 8.3, namely that there exists no correlation of the subpulse phases across nulls, stands disproved.

The expected distribution for total drift is shown in Figure 8.4 (solid line) alongwith that of the observed total drift (dashed line) for Class A and Class B transitions. The errors for these distributions are derived in Appendix C.5 and C.6. The two distributions differ significantly (the errors for two points, where the distributions differ the most, are indicated in the figure) for both the modes. The hypothesis that the two distributions are the same was rejected at high significance for both the modes when a Kolmogorov - Smirnov test was carried out. Thus it can be concluded that there is some correlation of the subpulse phases across nulls.

A second feature of the curves presented in Figure 8.4 is the non-zero mean drift across nulls.

[e]This is not a convolution since one is considering the difference, and not the sum, of two random variables.

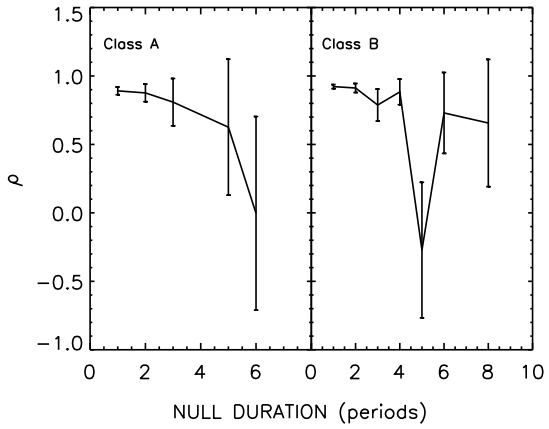

Figure 8.5: Plot of normalized correlation coefficient, ρ (as defined in Equation 8.4), for null durations 1 to 6 in Class A (left frame) and for null durations 1 to 8 in Class B (right frame) null transitions. One standard deviation errors on the correlation are also indicated.

The peak of the observed distribution for total drift across nulls is at -10.0 ms period^{-1} indicating that substantial drift takes place during the null. The drift behaviour during a null is described in greater detail in the next section.

The analysis presented in Figure 8.4 includes null transition with all null durations. It was observed that the correlation implied in this analysis varied with null durations; a strong correlation was observed for short nulls whereas there was insignificant correlation for long nulls. This dependence is best illustrated by computing the normalized correlation coefficient, which is defined as

$$\rho = \left\langle \frac{[\phi_{on} - \langle\phi_{on}\rangle]\,[\phi_{off} - \langle\phi_{off}\rangle]}{\sigma_{\phi_{on}}\sigma_{\phi_{off}}} \right\rangle \tag{8.4}$$

where ϕ_{on} and ϕ_{off} are the turn-on and turn-off phase respectively.

Figure 8.5 shows the normalized correlation coefficient ρ, between the turn-off and turn-on phases as a function of null duration for the two modes. The errors on ρ were computed using the derivation given in Appendix C.2. These are inversely proportional to the square root of the number of transitions used in calculating ρ. It is evident from the figure that significant correlation exists up-to null durations ≈ 4 periods, although it appears to decrease for longer nulls. However, the correlation coefficient for long nulls is calculated from sparse data and this should be kept in mind while interpreting Figure 8.5.

8.2 Drift during short nulls

It is evident from Figure 8.4 that the subpulse drifting continues during nulls (at least for short nulls). To study this further, the average drift during short nulls, for which the subpulses at the turn-off and turn-on periods could be identified unambiguously, was investigated. This study was

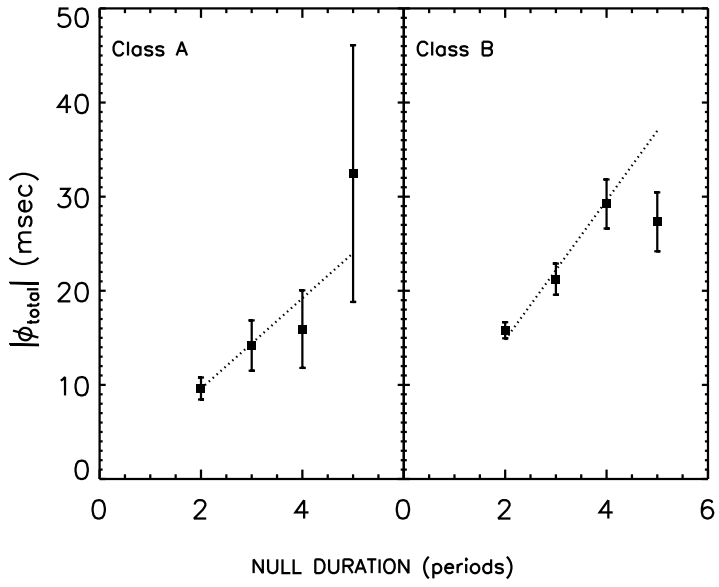

Figure 8.6: The modulus of the total drift across nulls, $\mid \phi_{total} \mid$, for null durations 1 to 4 in Class A (left frame) and Class B (right frame) null transitions alongwith $\pm\sigma$ errors. The dotted line corresponds to a constant drift rate across nulls.

carried out for short nulls only as (1) the correlation is significant for such nulls and (2) the long nulls are rare in this pulsar (Vivekanand 1995).

The total drift across nulls, i.e. $\phi_{total} = (\phi_{on} - \phi_{off})$, was determined for each null duration and this is shown in Figure 8.6 for the two dominant modes. These were then fitted to three possible models, *viz.*, (1) total cessation of drift,i.e, $\phi_{total} = 0.0$; (2) a constant drift rate $\phi_{total} = \alpha_0 n$; and (3) $\phi_{total} = \alpha_0 n + \alpha_1 n^2$, where n is the null duration. The fits were carried out using chi-squares weighted with the error on each data point. The fitted parameters, for null durations 1 to 4, and the chi-square for the fits in case of Class A transitions are shown in Table 8.1 and those for Class B transitions are shown in Table 8.2.

It can be seen from the tables that the first model, which assumes total cessation of drift during a null, i.e., turn-on phase equal to turn-off phase, is clearly a bad fit; thus some drift does occur during short nulls. A constant drift rate (model 2) is adequate to explain the drift across short nulls for Class A transitions as is evident from Figure 8.6 and Table 8.1. However, the fit to the data for Class B transitions is poor for a constant drift rate (model 2). Here, the drift appears to decrease with null duration (model 3).

8.3 Discussion

These results show the existence of subpulse phase correlation across short nulls in PSR B0031-07. A significant correlation exists between the turn-on and turn-off phase up-to null durations ≈ 4 periods for the two dominant drift modes, although it decreases for longer nulls. This implies

	Model	Parameters (ms / period)	χ^2	Degree of freedom
1	$\phi_{total} = 0$	-	116	4
2	$\phi_{total} = \alpha_0 n$	$\alpha_0 = -4.8 \pm 0.2$	1	3
3	$\phi_{total} = \alpha_0 n +$ $\alpha_1 n^2$	$\alpha_0 = -5.0 \pm 0.9$ $\alpha_1 = 0.1 \pm 0.3$	0.9	2

Table 8.1: Fitted Parameters for Class A null transitions.

	Model	Parameters (ms / period)	χ^2	Degree of freedom
1	$\phi_{total} = 0$	-	709	4
2	$\phi_{total} = \alpha_0 n$	$\alpha_0 = -7.4 \pm 0.2$	10	3
3	$\phi_{total} = \alpha_0 n +$ $\alpha_1 n^2$	$\alpha_0 = -9.4 \pm 0.5$ $\alpha_1 = 0.8 \pm 0.1$	2	2

Table 8.2: Fitted Parameters for Class B null transitions.

a time-scale for phase correlation in this pulsar. Some drift occurs during the nulls, but the drifting behaviour for the two classes of null transitions is different. While the drift rate appears to be constant for Class A transitions, it appears to decrease with the null duration for Class B transitions. These results, together with the reported behaviour of PSR B1944+17 and PSR B0809+74, seem to imply that there exist different time scales for phase correlation in different pulsars (PSR B0809+74 : $10 \sim 20$ periods; Lyne and Ashworth (1983), PSR B0031-07 : $4 \sim 5$ periods and PSR B1944+17 : less than a period; Deich et al. (1986)).

It is interesting to consider the impact of null duration on the analysis of Section 8.1 in view of the results of Section 8.2. The difference in the drift behaviour during the nulls for the two classes of null transitions affects the correlation in Figure 8.4, where all null durations have been considered. The correlation will be effectively reduced for Class B transitions due to the non-linear dependence of its drift rate on null duration. Hence, these transitions appear more random than Class A transitions in this figure. The results of Figure 8.4 provide sufficient but not necessary conditions for phase correlation. A study of the phase correlation for individual null durations, as in Figure 8.5, is also required. We could not compute the correlation coefficients for longer nulls as very few null transitions for *individual null durations* were available despite our large data set.

A correlation between the turn-off and turn-on phases implies that the state of the process responsible for drifting is memorized during a null. In the case of PSR B0809+74, such a correlation is due to a cessation or a characteristic reduction of subpulse drift. Here, the entity causing a subpulse somehow survives and its position is remembered. This has been referred to as phase memory (Page 1973; Unwin et al. 1978; Lyne and Ashworth 1983) in this pulsar. Alternatively,

the subpulse drift may continue during a null at more or less the same rate as in a burst and this may be called as memory of drift rate. The memory for short nulls in case of PSR B0031-07 appears to be of the latter type.

On the other hand, an absence of such a correlation implies total destruction of the entity responsible for a subpulse drift at the onset of a null. The drifting process starts afresh for such a case at a random location in the pulsar beam and is independent of nulling behaviour of pulsar. This appears to be the case in PSR B1944+17. Our results together with the results reported earlier suggest a time-scale over which the process causing subpulse drift is disrupted totally. These issues are discussed later in the last chapter.

Chapter 9

Summary and Discussion

A detailed study of "subpulse drifting", "nulling" and "mode-changing" phenomena in PSR B0031−07 is presented in this thesis. The connection between these phenomena have been explored using high sensitivity data consisting of more than 40,000 single pulses on this pulsar obtained with Ooty Radio Telescope. This study clearly demonstrates that these phenomena are related with each other. These data were also used to study the properties of subpulse, which is regarded as a probable unit of emission, as a function of drift rate. Quantitative measurements of these properties and the distribution of drift rates were obtained, which will be useful in the elaboration of pulsar models.

Our results are broadly consistent with Ruderman and Sutherland (1975) model. This is borne out by the drift rate dependence of the subpulse properties presented in this thesis. The variation of drift rate at the edges of the integrated profile also appears to be consistent with the conal geometry implied by Ruderman and Sutherland model for this pulsar. These results should provide the necessary motivation for fundamental theoretical work to revive this model, which has been plagued with theoretical inconsistencies.

Our data confirms that this pulsar shows three different drift modes. Two kinds of nulls are also observed - (1) short nulls of one to three pulses durations (Type II) and (2) long nulls with durations ranging from few pulses to several hundred pulses (Type I). The three drift modes appear to be interlaced with the latter type of nulls. The phase of the subpulse before and after a Type II null appears to be correlated. This study demonstrates that the integrated profile for each mode is different. These results suggest that the above three phenomena are observational manifestation of different modes of the same physical process operating in pulsars.

The main results of this work are summarized below

1 Measurements of drift rates for 3338 drift bands are presented in this thesis. The drift rate varies from band to band in this pulsar and a distribution from 0 ms period^{-1} to -18 ms period^{-1} is inferred from the data. Three drift modes can be inferred from the observed distribution centered at -4.05 ms period^{-1} (Class A), -7.78 ms period^{-1} (Class

B) and -11.46 ms period^{-1} (Class C). The former two are dominant modes for this pulsar occurring in 15.6 % and 81.8 % of pulses whereas the last mode occurs rarely. These results are consistent with the values quoted by Huguenin, Taylor and Troland (1970).

2 Both type I and type II nulls are observed in this pulsar. The spectrum of nulling pattern for the pulsar was obtained and it shows a significant broad line feature suggesting that the nulling pattern in this pulsar is quasi-periodic. The time scale corresponding to this line feature is of the order of 80 periods. This spectral feature is consistent with a much weaker feature reported by Huguenin, Taylor and Troland (1970).

3 The average subpulse properties were obtained as a function of drift rates. The average value of the subpulse width is 7.44 ms and is independent of the drift rate. The subpulse energy is higher in the dominant drift mode (Class A), but no correlation is apparent with drift rate otherwise. On the other hand, the average spacing P_2 between the two drifting subpulses increases monotonically with the modulus of drift rate, contrary to the belief held so far. These measurements have been reported for the first time and the drift dependence of P_2 is a new result of the thesis.

4 The pulses belonging to the three drift modes for this pulsar add upto three integrated profiles, which are significantly different. This result demonstrates a possible connection between drifting and mode-changing and is consistent with a qualitative result reported earlier (Wright and Fowler 1981b). The three profiles are being reported for the first time. The average pulse for the Class A mode arrives earlier than that for Class B mode. There is a similar shift in longitude between Class B and Class C. The RMS width of the profile decreases progressively from Class C mode to Class A. However, the last two results should be treated with caution as our data are single polarization data.

5 An integrated profile for the pair of drifting subpulses was obtained after aligning these by removing the drift. The two subpulses in this profile are well separated. More than two subpulses are sometimes seen consistent with the existence of several sparks marching around the polar cap implied by Ruderman and Sutherland model. The energies of adjacent subpulses are anti-correlated and this suggest a competition between the subpulses.

6 The shape of a drift band is linear to a first order. However, significant departure from linearity is observed at the edges of the integrated profile, where the drift rate appears to increase. The path of a drifting subpulse seems to be consistent with at least a third order polynomial for Class B drift bands whereas it is more or less linear for Class A bands.

7 The data imply a phase correlation across nulls which decreases with null duration. The drift rate during the short nulls appears to be constant for Class A drift mode transitions, whereas it decreases with null duration for Class B transitions. These results suggests a relationship between drifting and nulling in this pulsar.

These results are discussed in the context of the main scientific objectives of this work, enumerated in Section 2.5, in the rest of the chapter.

9.1 Discussion

A discussion of the Ruderman and Sutherland model and its subsequent modifications was presented in Section 1.3.4. In this section, the results of this study are examined in the context of this model. This is followed by a discussion on the connection between "drifting", "nulling" and "mode-changing" phenomena in pulsars indicated by our results.

9.1.1 Implications for Ruderman and Sutherland model

The most remarkable feature of Ruderman and Sutherland model is the idea of well separated localized "sparks". To quote Curtis Michel (1991) ".. it suggests that the subpulse continues to exist outside of the viewing window! Thus in Ruderman and Sutherland (1975) we have the concept of a full series of unseen subpulses marching around the polar caps. It would be interesting if this view could be tested somehow". The subpulse properties that are drift independent have been studied in this thesis in this context. As discussed in chapter 6, there are several instances of a third subpulse in a single period in the data suggesting at least three sub-beams or "sparks", which is a confirmation of the above. This view is further supported by observations of PSR B0826-34, where five drifting sub-beams were reported (Biggs et al. 1985a). Our observations are the only other direct observations of more than two sub-beams. More recently, a system of 20 sub-beams has been reported in PSR B0943+10, which was inferred indirectly by a Fourier analysis of data on this pulsar (Deshpande and Rankin 1999). Thus, our results are consistent with a system of sparks proposed in the Ruderman and Sutherland model.

The average sub-beam pattern of PSR B0031-07, obtained after removing the drift, shows two well separated peaks. Our results indicate that the emission in the saddle region is much less than one thirtieth of the peak value. In Ruderman and Sutherland model, the formation of a spark at a point in the gap is expected to inhibit another spark within a distance comparable to gap height. If the radio emission region are locked to the sparks, this implies that there will be little detectable radio emission between the subpulses. Thus, our results are consistent with this expectation.

Equations 1.8 and 2.1 connect the drift speed of a spark v and the gap height h in the Ruderman and Sutherland model. As stated in the last paragraph, two sparks are likely to be separated by a distance comparable to h. This implies that the separation between two subpulses is related to h as well and should in general depend on the drift rate. This observational implication was not stated explicitly in this model or its subsequent modifications. On the other hand, observations of PSR B0809+74 indicated that the average subpulse separation, P_2, is a stable quantity for this pulsar and it appears that this was assumed to be the case in all drifting pulsars. However, it must be noted that this pulsar has a very stable drift rate and is therefore likely to have a constant P_2.

Thus, the relation between P_2 and drift rate has not been tested so far.

This study demonstrates that P_2 is indeed related to drift rate, contrary to the belief held so far and increases monotonically with the modulus of drift rate. Thus, this result is in agreement broadly with Ruderman and Sutherland model. At the same time, its details have no explanation in this model, which needs an elaboration. A simplistic view of this result suggests that P_2 is proportional to the square of gap height h. This is plausible as the exact theoretical relationship between P_2 and the gap height may be complicated because it should take into account the connection between the "sparks" and the radio emission region and the geometry of the field lines. These details have not been provided in the original model or its subsequent modifications. Clearly, a new theoretical initiative is required.

Alternatively, the dependence of P_2 on drift rate can be explained by assuming that the altitude of radio emission regions increases with the magnitude of drift speed within Ruderman and Sutherland framework. The emission regions translate in altitude along the dipolar field lines, so the above assumption implies that the radius of the conal beam increases with drift rate. If the number of sparks remain the same with increasing drift rate, this implies an increase in the separation between the sparks, or equivalently the emission regions, with the modulus of drift rate. This explanation is also consistent with the different widths of the integrated profiles for three modes and is entirely plausible. Again, the exact relationship needs to be worked out theoretically.

It is difficult to rule out either of the explanation based on our data currently. It is more likely that the observed dependence is due to both the explanations proposed above. Nevertheless, this result provides motivation and direction for the refinement of Ruderman and Sutherland model. Thus, this is an important new result of this thesis.

The geometry of emission regions, implied by Ruderman and Sutherland model in case of organized drifters such as PSR B0031-07, is that of a hollow cone. Oster and Sieber (1976) showed that the average drift path for a hollow cone geometry in case of a tangential traverse of observer's line of sight will be an S-shaped curve. This implies that the *apparent* drift rate increases at the edges of the integrated profile. This is indeed confirmed by the analysis presented in this thesis.

In this context, it should be noted that the result concerning the average drift path for Class A mode appears to be inconsistent with the expectation. As the drift rate for this mode is smaller than that for Class B mode, a better sampling of the on-pulse window is possible for these drift bands. Thus, the detection of any drift rate variation is expected to be better in this case. However, this result can still be reconciled with the hollow cone geometry if it is assumed that the radiation cone for this mode has shrunk in solid angle around the magnetic axis. Such an assumption is consistent with the relative widths of the Class A and Class B profiles reported in this thesis and as discussed later. A reference to Figure 4 of Oster and Sieber (1976) indicates that our results are consistent with the hollow cone geometry if the radiation cone geometry changes from a "central passage" for Class B mode to a "below-center passage" for Class B mode. Thus, these results are not only consistent with Ruderman and Sutherland model, but also indicate that the size of

emission cone is different for the two modes. It is to be noted that a similar conclusion was arrived at independently while considering the dependence of P_2 on the drift rate.

While the results discussed above are consistent with Ruderman and Sutherland model, a refinement of this model is suggested by the other results of this thesis. The observed distribution of drift rates indicates three drift modes in this pulsar. The drift rate also varies from one drift band to another. No explanation for this variability has been proposed in Ruderman and Sutherland model. The distribution obtained in this research work provides a tight constraint for any theoretical explanation. Secondly, the quantitative measurements of subpulse energy and width as a function of drift rate provide tight constraints for the emission mechanism responsible for the subpulse emission. Lastly, this study demonstrates that the pair of adjacent drifting subpulses compete with each other. This is an entirely new idea which has been proposed for the first time. This result has implication for the breakdown mechanism of the acceleration zones or vacuum gap proposed in Ruderman and Sutherland (1975) model as well as for the growth rates of the spark discharge.

It is concluded that our results support the basic Ruderman and Sutherland model and suggests directions for its further evolution.

9.1.2 The drifting, nulling and mode-changing phenomena

One of the main objectives of this thesis was to investigate the connection between "drifting", "nulling" and "mode-changing". Our results show that these phenomena are not independent of each other and this dependence is discussed below.

Three drift modes were seen in this pulsar. The pulses belonging to each drift mode add upto significantly different integrated profiles. In this sense, this pulsar shows mode-changing. It must be noted that this pulsar has a single component integrated profile, which makes it difficult to see this mode-changing behaviour in the canonical sense unlike multiple component profiles. Moreover, a given drift mode lasts for a few tens of periods, particularly for Class A and Class C modes, making such profile changes less dramatic. This is in contrast with pulsars such as PSR B0329+54, where a mode may last for several hundred periods. A time-scale of the order of 60 minutes for the abnormal mode is reported for this pulsar (Bartel et al. 1982). This is probably the reason why PSR B0031−07 has not been classified as a classical mode-changer. Clearly, the issue is of time-scale between mode transitions in different pulsars and the morphological appearance of the integrated profile. Nevertheless, such short time scales for profile changes are not uncommon in other mode-changers. An example is PSR B1737+13, in which bursts of two different modes occur for a few tens of periods (Rankin, Wolszczan and Stinebring 1988). Thus, we conclude that the profile changes in this pulsar are indeed mode-changes in the classical sense.

This provides a possible model for mode-changes. In this context, it is relevant to refer to an idea suggested by Wright and Fowler (1981a), where they stated "all pulsars whose subpulse drift behaviour undergoes sudden changes could be considered mode-changing pulsars. Mean

profile changes and jumps in P_3 may be two observational aspects of the same phenomenon". Our results are certainly consistent with this idea. Thus, a change in subpulse pattern may be more fundamental in nature, which provides a mechanism to unify these two phenomena.

Equally important are our results regarding the relative amplitude and the width of the profiles for the three different modes. Although these results should be treated with caution due to single polarization nature of the data, such changes in width have been reported earlier for classical mode-changers. A decrease in the separation between the peaks of the outer components has been reported for PSR B1926+18 by Ferguson et al. (1981). These changes can be interpreted as a shift in the emission altitude. An increase in this altitude leads to an increase in the radius of the emission cone and its observational implication is an increase in the width of the profile. A similar interpretation of the profile changes in PSR B1926+18 has been suggested by Nowakowski (1994).

It is remarkable that our results indicate the same conclusion from three different points of view. Firstly, a possible change in emission altitude is suggested by the relationship between P_2 and the drift rate. Secondly, the different contours for the average drift path obtained by us require a similar interpretation. Finally, the analysis of the relative widths of the integrated profile for different modes appears to be consistent with this hypothesis. Thus, it is quite plausible that the radial distance of the emission region does change in different modes of operation of a pulsar.

Long nulls may probably be an extreme form of profile change. Data indicate that the profile mode-changes are often interlaced with Type I nulls. Moreover, there is evidence for quasi-periodicity in the nulling pattern which seems to be associated with Type I nulls. Such nulls usually have very different distributions (Backer 1970c; Vivekanand 1995) from Type II nulls, which additionally show a correlation of subpulse phase across them as demonstrated be our analysis. Hence, it is plausible to consider burst-null-burst transitions of this type as a mode-change.

The analysis presented in this thesis also shows that the subpulse drift is affected by nulling at least for short or Type II nulls, which usually occur between bursts of similar drift mode. There is evidence for a phase correlation across such nulls which decreases with null duration. This result, together with the reported behaviour of PSR B1944+17 and PSR B0809+74, , seem to imply that there exist different time scales for phase correlation in different pulsars (PSR B0809+74 : $10 \sim 20$ periods; Lyne & Ashworth 1983, PSR B0031-07 : $4 \sim 5$ periods and PSR B1944+17 : less than a period; Deich et al. 1986).

The drift rate measured across nulls for Class B transitions suggests that the onset of a null affects the process responsible for the subpulse drift in a manner similar to that reported by Lyne and Ashworth (1983) in case of PSR B0809+74. However, it is difficult to understand the result obtained for Class A mode, where the drift rate across nulls appears to be similar to that in the burst.

Nulling and its interaction with drifting was not accounted for by Ruderman and Sutherland model. A hot-spot produced by the heating of polar cap by the backward flowing relativistic electrons of the Sturrock cascade was proposed in a later modification of the basic model (Cheng

and Ruderman 1980). The phase memory in PSR B0809+74 could be interpreted in terms of this hot-spot although some theoretical arguments against such hot-spot has been reported (Filippenko and Radhakrishnan 1982). The phase correlation time-scale indicated by the results of this study can be related to the cooling time-scale of this hot-spot. This is not possible in the alternative model proposed by Filippenko and Radhakrishnan (1982). However, the explanation of drift across nulls as well as a qualitative theory for nulling are attractive features of the latter model. The drift behaviour across nulls indicated by our study are more in accord with the latter explanation.

In summary, the results presented in this thesis show that PSR B0031-07 operates in three modes. These three modes are characterized by different fluctuation properties as well as different integrated profiles. The radial distance of the emission region from the star appears to be different in different modes of the pulsar. Our results appear to suggest the existence of distinct time-scales over which the pulsar radiation changes in a characteristic fashion and drifting, nulling and mode-changing seem to be observational manifestations of such time scales. The different modes of the pulsar may be associated with changes in the properties of vacuum gap in the Ruderman and Sutherland framework. Thus, these result indicate that drifting, nulling and mode-changing may find a common explanation by elaborating the basic Ruderman and Sutherland model.

9.1.3 Conclusion

A detailed study of single pulses in PSR B0031-07 was presented in this thesis discussing drifting, nulling and mode-changing phenomena in this pulsar. The results suggest that these phenomena are related and may have a common origin within the framework of Ruderman and Sutherland model. Many of the results are consistent with and support this model. These results also motivate the further development of this model and provide observational constraints for such modifications.

It is appropriate here to mention two new models proposed recently, which deal with some issues related to the dynamics of pulsar emission. A model was recently proposed to explain nulling and drifting as well as the phase memory observed in PSR B0809+74 (Kazbegi et al. 1996). The basic assumptions for this model are different from Ruderman and Sutherland model. No vacuum gap is envisaged and particle extraction from the surface is assumed as in the slot-gap model (Arons 1981b). The model has an explanation for the reduction of drift rate at the onset of null. It also suggests a distribution of null durations as seen in PSR B0031-07 and other pulsar. However, the variability of drift rates in pulsars have not been explained in this model. There is also no mechanism for different modes of a pulsar as is evident in PSR B0031-07.

A very recent model extending the basic hollow cone Ruderman and Sutherland model has been proposed by Gil and Sendyk (2000). This model retains the spark picture of the basic model and incorporates a quasi-central spark, which gives rise to the core emission. The authors have argued that the main advantage of their model is that it removes some theoretical inconsistencies which have plagued Ruderman and Sutherland model and it explains the core emission. Since the observational implications of this model are similar to that of the Ruderman and Sutherland

model for conal single pulsars, our results are consistent with it. However, this model still needs to be modified to take into account the different modes of the pulsar.

An attempt has been made in this direction by Zhang et al. (1997) to understand the various modes of operation of the pulsar inner gap. Our results cannot be directly compared with this model as the details of the observational implications of different modes were not stated explicitly. On the other hand, our results do indicate that the mode-changes may be related to different modes of pulsar inner gaps and are in qualitative agreement with a similar prediction made by these authors.

Lastly, the basic assumption of Ruderman and Sutherland model regarding the ion work function is no longer accepted (Hillebrandt & Muller 1976;Michel 1974; Fawley, Arons& Scharlemann 1977). An interesting suggestion to lift this inconsistency has recently been proposed invoking strange stars (Xu, Qiao and Zhang 2000). It is not yet clear whether pulsars are strange stars, but our results do point out towards a genuine need to reinvestigate the basis of Ruderman and Sutherland model, perhaps by using unconventional ideas.

Appendix A

Numerical Methods for model fitting

A brief description of the mathematical expressions and the methods useful for modeling the data is presented in this Appendix. These methods are described in detail in Press et al. (1992).

A.1 Chi-square fitting

All modeling of data involves minimization of a figure of merit function, which measures the agreement between the data and the model. The most commonly used figure of merit function is the "chi-square" function, given by

$$\chi^2 \equiv \sum_{i=1}^{N} \left(\frac{y_i - y(x_i : a_1, \ldots, a_m)}{\sigma_i} \right)^2 \tag{A.1}$$

where,

y_i = observed data

y = modeled data

σ_i = measurement errors on the observed data

The distribution for χ^2 is the "chi-square" distribution, which results from the sum of squares of N normally distributed quantities. The probability of a χ^2 value obtained in a given fit gives a measure of the goodness of fit. A typical χ^2 value for a good fit is of the order of $P = N - M$, where N is the number of data points and M is the number of the parameters of the model. P is usually referred as degrees of freedom in the fit.

A.2 General weighted linear least squares fit

The general form of a linear-in-parameter model is given by

$$y(x) = \sum_{k=1}^{M} a_k X_k(x) \tag{A.2}$$

where $X_1(x), \ldots, X_M(x)$ are arbitrary functions of x. These functions are also referred as basis functions. The χ^2 for this model is then given by

$$\chi^2 = \sum_{i=1}^{N} \left[\frac{y_i - \sum_{k=1}^{M} a_k X_k(x_i)}{\sigma_i} \right]^2 \tag{A.3}$$

The minimum of χ^2 occurs when its derivative with respect to all M parameters a_k vanishes. Taking the derivative of Equation A.3, we obtain the following M equations

$$0 = \sum_{i=1}^{N} \frac{1}{\sigma_i^2} \left[y_i - \sum_{j=1}^{M} a_j X_j(x_i) \right] X_k(x_i) \quad k = 1, \cdots, M \tag{A.4}$$

These can be written as a matrix equation

$$(\mathbf{A}^T \cdot \mathbf{A}) \cdot \mathbf{a} = \mathbf{A}^T \cdot \mathbf{b} \tag{A.5}$$

where, $\mathbf{a}$ is a M vector whose components are the parameters to be fitted and the components of the matrices $\mathbf{A}$ and $\mathbf{b}$ are defined as

$$A_{ij} = \frac{X_j(x_i)}{\sigma_i} \tag{A.6}$$

$$b_i = \frac{y_i}{\sigma_i} \tag{A.7}$$

Equations A.5 are often called as the normal equations. These can be solved by using the usual methods of solving linear algebraic equations such as Choleksy decomposition, Gauss-Jordan elimination or Singular value decomposition and the best fit estimate for the parameters are obtained from the solutions.

The uncertainties in the best fit parameters are obtained from the covariance matrix $\mathbf{C}$, which is given by

$$\mathbf{C} = (\mathbf{A}^T \cdot \mathbf{A})^{-1} \tag{A.8}$$

The diagonal elements of this matrix are the variances of the best-fit parameters while the off-diagonal elements are the covariances between the respective parameters.

A.3 Nonlinear Model fit

Many useful models required in this thesis are not linear-in- parameter. The most common example in this thesis is the Gaussian model for the subpulse. No exact solution can be obtained for such models unlike the case of generalized weighted least squares scheme described above. However, an approach similar to this method can be used for obtaining reasonable fits to such model. Again, a χ^2 merit function is defined and this is minimized iteratively till the decrease in χ^2 becomes smaller than a desired limit.

Let the model to be fitted be

$$y = y(x, \mathbf{a}) \tag{A.9}$$

and the χ^2 be given by Equation A.1. Minimization of χ^2 can be achieved by one of the standard methods of function minimization. One of the popular methods is the method of steepest gradient. In this method, the gradient of χ^2, which is a vector of the first partial derivatives of χ^2 with respect to the parameters, is used to find the direction of the steepest descent in the M-dimensional parameter space. A single dimensional minimization is then carried out in this direction and this two step procedure is repeated till the minimum is sufficiently close.

Sufficiently close to the minimum, χ^2 can be approximated by the following quadratic form

$$\chi^2(x;\mathbf{a}) = \chi^2(x,\overline{\mathbf{a}}) + \sum_i \frac{\partial \chi^2}{\partial a_i} a_i + \frac{1}{2}\sum_{i,j} \frac{\partial^2 \chi^2}{\partial a_i \partial a_j} a_i a_j + \cdots \tag{A.10}$$

where the higher order terms can be neglected sufficiently close to the minimum. This can be written in vector notation as

$$\chi^2(\mathbf{a}) \approx \gamma - \mathbf{d}\cdot\mathbf{a} + \frac{1}{2}\mathbf{a}\cdot\mathbf{D}\cdot\mathbf{a} \tag{A.11}$$

where $\mathbf{d}$ refers to the vector with first order partial derivative of χ^2 and $\mathbf{D}$ refer to a matrix with the second order partial derivative of χ^2 as components. The minimum of χ^2 function can be reached in this M dimensional parameter landscape by modifying $\mathbf{a}$ in the following fashion

$$\mathbf{a}_{min} = \mathbf{a}_{cur} + \mathbf{D}^{-1}\left[-\nabla\chi^2(\mathbf{a}_{cur})\right] \tag{A.12}$$

This equation is actually a set of M linear equation as can be recognized by rewriting it in the following manner

$$\mathbf{D}\cdot\delta\mathbf{a} = \mathbf{d} \tag{A.13}$$

Here, $\mathbf{D}$ is also known as Hessian or curvature matrix.

Thus, χ^2 can be minimized by a combination of the above two methods. Such a combination was proposed by Marquardt (1963) and the method is known as Levenberg- Marquardt method. Here, the method of steepest descent is used far away from the minimum to approach the local minimum of the χ^2 landscape. Near the local minimum, a single step using Equation A.13 is taken to reach the minimum. The method involves repeated evaluation of gradient and Hessian matrix and is iterative in nature. Most often, a value of χ^2 sufficiently close to the minimum is reached and subsequent iterations only provide a χ^2 that oscillates close to this minimum.

The diagonal components of the Hessian matrix provide an order of magnitude estimate of the extent of the steepest gradient. The direction of this gradient is itself given by $\mathbf{d}$. The modified steepest descent formula used in this method can be written using the above information as

$$\delta a_k = \frac{1}{\lambda \alpha_{kk}}\beta_k \tag{A.14}$$

where δa_k and β_k are the k^{th} component of $\delta\mathbf{a}$ and $\mathbf{d}$ matrices respectively and α_{kk} is the diagonal component of the Hessian matrix. λ is an arbitrary constant. Marquardt (1963) proposed that

Equation A.14 can be incorporated in Equation A.13 by the following re-definition of the curvature matrix **D**

$$\alpha'_{kk} \equiv \alpha_{kk}(1+\lambda) \tag{A.15}$$

$$\alpha'_{jk} \equiv \alpha_{jk} \qquad j \neq k \tag{A.16}$$

$$\tag{A.17}$$

In this way, a steepest descent is carried out when λ is large, whereas direct minimization of Equation A.13 takes place for its small values.

Once the minimum has been reached, the best fit parameters for the model are given by **a** and the standard errors on the parameters are given by the diagonal elements of the inverse of the curvature matrix.

A fit involving any non-linear model can be carried out using this method which is also numerically very robust. The method requires an evaluation of the model at the values of the independent variable and the derivatives of the model function with respect to the parameters of the model. The latter are then used in this method to obtain the gradient and Hessian matrix. The model and its derivatives are usually supplied by a user defined function which is called repeatedly by the main fitting procedure. Some example models used in this thesis and their derivatives are listed in the next section.

A.4 Commonly used functions in squares fit

A.4.1 Two Gaussians plus a Constant

The fitting function is given by

$$f(x) = A\exp\left(-\left[\frac{x-B}{C}\right]^2\right) + D\exp\left(-\left[\frac{x-E}{F}\right]^2\right) + G \tag{A.18}$$

and its derivatives are

$$\frac{\partial f}{\partial A} = \exp\left(-\left[\frac{x-B}{C}\right]^2\right) \tag{A.19}$$

$$\frac{\partial f}{\partial B} = \frac{2A(x-B)}{C^2}\exp\left(-\left[\frac{x-B}{C}\right]^2\right) \tag{A.20}$$

$$\frac{\partial f}{\partial C} = \frac{2A(x-B)^2}{C^3}\exp\left(-\left[\frac{x-B}{C}\right]^2\right) \tag{A.21}$$

$$\frac{\partial f}{\partial D} = \exp\left(-\left[\frac{x-E}{F}\right]^2\right) \tag{A.22}$$

$$\frac{\partial f}{\partial E} = \frac{2D(x-E)}{F^2}\exp\left(-\left[\frac{x-E}{F}\right]^2\right) \tag{A.23}$$

$$\frac{\partial f}{\partial F} = \frac{2D(x-E)^2}{F^3}\exp\left(-\left[\frac{x-E}{F}\right]^2\right) \tag{A.24}$$

$$\frac{\partial f}{\partial G} = 1 \tag{A.25}$$

A.4.2 One "modified" Lorentzian plus a constant

The fitting function is given by

$$f(x) = \frac{A}{\left[(x-B)^2 + C^2\right]^D} + E \tag{A.26}$$

and its derivatives are

$$\frac{\partial f}{\partial A} = \frac{1}{\left[(x-B)^2 + C^2\right]^D} \tag{A.27}$$

$$\frac{\partial f}{\partial B} = \frac{2AD(x-B)}{\left[(x-B)^2 + C^2\right]^{(D+1)}} \tag{A.28}$$

$$\frac{\partial f}{\partial C} = \frac{-2ACD}{\left[(x-B)^2 + C^2\right]^{(D+1)}} \tag{A.29}$$

$$\frac{\partial f}{\partial D} = \frac{-A\log\left[(x-B)^2 + C^2\right])}{\left[(x-B)^2 + C^2\right]^D} \tag{A.30}$$

$$\frac{\partial f}{\partial E} = 1 \tag{A.31}$$

A.4.3 Two "modified" Lorentzian plus a constant

The fitting function is given by

$$f(x) = \frac{A}{\left[(x-B)^2 + C^2\right]^k} + \frac{D}{\left[(x-E)^2 + F^2\right]^k} + G \tag{A.32}$$

where k is a fixed constant and is not a parameter for the fit. Its derivatives are

$$\frac{\partial f}{\partial A} = \frac{1}{\left[(x-B)^2 + C^2\right]^k} \tag{A.33}$$

$$\frac{\partial f}{\partial B} = \frac{2Ak(x-B)}{\left[(x-B)^2 + C^2\right]^{(k+1)}} \tag{A.34}$$

$$\frac{\partial f}{\partial C} = \frac{-2ACk}{\left[(x-B)^2 + C^2\right]^{(k+1)}} \tag{A.35}$$

$$\frac{\partial f}{\partial D} = \frac{1}{\left[(x-E)^2 + F^2\right]^k} \tag{A.36}$$

$$\frac{\partial f}{\partial E} = \frac{2Dk(x-E)}{\left[(x-E)^2 + F^2\right]^{(k+1)}} \tag{A.37}$$

$$\frac{\partial f}{\partial F} = \frac{-2DFk}{\left[(x-E)^2 + F^2\right]^{(k+1)}} \tag{A.38}$$

$$\frac{\partial f}{\partial G} = 1 \tag{A.39}$$

Appendix B

Fourier Techniques used in the data analysis

The data analysis carried out in this thesis relied on use of Fourier techniques. A brief review of these techniques is presented in this appendix.

B.1 Time Shift of sampled data

Consider a finite length sequence $x[n]$ of length N samples such that $x[n] = 0$ outside the range $0 \leq n \leq N-1$. We can always associate a periodic sequence $\tilde{x}[n]$ with this finite length sequence given by

$$\tilde{x}[n] = \sum_{k=-\infty}^{\infty} x[n + kN] \tag{B.1}$$

This original sequence can be visualized as a part of the periodic sequence $\tilde{x}[n]$. Now, $\tilde{x}[n]$ can also be represented by a Fourier series given by

$$\tilde{X}[l] = \sum_{m=0}^{M-1} \tilde{x}[n] e^{-j(2\pi/M)lm} \tag{B.2}$$

where M is the period of the periodic sequence. A fundamental property of this periodic sequence is the time-shift property which follows from the time shifting property for Fourier Transform. This property states that the discrete Fourier series of time shifted version of the periodic sequence $\tilde{x}[n]$ is given by

$$\tilde{X}_1[l] = e^{-j(2\pi/N)lp} \tilde{X}[l] \tag{B.3}$$

where p is the required time shift. The corresponding periodic time sequence is given by

$$\tilde{x}_1[n] = \tilde{x}[n - p] \tag{B.4}$$

The shifted finite sequence is then obtained by extracting one period (length = N) from $\tilde{x}_1[n]$ and corresponds to a circular shift or a rotation of the sequence in the interval $0 \leq n \leq N-1$.

It can be shown that Discrete Fourier transform (DFT) corresponds to a period of the periodic Fourier series for a periodic sequence (Oppenheim and Schafer 1989). This suggests the following method for carrying out time-shift of finite length sequence using Fast Fourier transform (FFT), which is an implementation of DFT.

First, the DFT of the finite sequence is obtained. It is multiplied by the phase gradient implied by the required shift in time as in Equation B.3. Finally, the shifted time sequence is recovered by taking inverse DFT.

This method is rigorously valid for integer samples only. A number of simulations were carried out to test its validity for shifts by non-integer samples. Impulse function, sine waves with different periodicity and actual pulsar data were used for these simulations. These test signals were shifted by carrying out time domain interpolation using SINC functions as well as by using the DFT technique described above.

The residual between the results of two methods were plotted to check for any artifact introduced by the DFT method. The errors in the center of the of the window defining the finite sequence were insignificant. However, the errors increased to a one percent level at the edge of the window.

It is worthwhile to discuss these errors in the context of the data. The relevant data in each period of the pulsar corresponds to the subpulses as is evident from the discussion of 6.1.1. These are centered in the window of the finite sequence being shifted. The data at the edges of the window corresponds to off-pulse samples. Thus, the method of shifting does not affect the subpulse data, while the off-pulse samples are corrupted to the extent of one percent.

B.2 Fractional resampling of sampled data

A continuous-time signal $x_c(t)$ can be represented by a discrete- time signal consisting of a sequence of samples

$$x[n] = x_c(nT) \tag{B.5}$$

and its discrete-time Fourier transform is given by

$$X(e^{j\omega}) = \frac{1}{T}\sum_{k=-\infty}^{\infty} X_c\left(j\frac{\omega}{T} - j\frac{2\pi k}{T}\right) \tag{B.6}$$

where, X_c, is the continuous time Fourier transform of $x_c(t)$.

It is often necessary to change the sampling rate of a discrete-time signal, i.e., to obtain a new representation of the underlying continuous time signal of the form

$$x'[n] = x_c(nT') \tag{B.7}$$

by resorting to discrete-time operations alone. The discrete-time Fourier transform of this signal is given by Equation B.6 with T replace by T'. In this section, the change of sampling rate by a non-integer ratio $T'/T = M/L$ is considered. It is shown that the sampling rate can be changed by a non-integer factor by combining interpolation and decimation. Interpolation is a discrete-time operation, which increases the sampling rate of a sampled data signal by filling in the missing values between the two samples of the original signal. Decimation, on the other hand, reduces the sampling rate of a given signal. Thus, an interpolator, that decreases the sampling period from T to T/L, followed by a decimator, which increases the sampling period by M, produces an output sequence $\tilde{x}_d[n]$, that has an effective sampling period of $T' = TM/L$. By choosing L and M appropriately, a non-integer change is sampling rate can be effected.

Interpolation is carried out in two steps. First, the data is padded with L - 1 zero samples between each sample of the original data. Then, this sequence is low pass filtered. The discrete-time Fourier transform of the zero padded series, $x_e[n]$,

$$x_e[n] = \begin{array}{ll} x[n/L], & n = 0, \pm L, \pm 2L, \ldots, \\ 0, & \text{otherwise.} \end{array} \tag{B.8}$$

is given by

$$X_e(e^{j\omega}) = \sum_{k=-\infty}^{\infty} x[k]e^{-j\omega Lk} = X(e^{j\omega L}) \tag{B.9}$$

Thus, the Fourier transform of the output is a frequency scaled version of the Fourier transform of the input with L copies of the original spectrum.

The low pass filter removes the multiple copies from the spectrum as well as band-limits the spectrum to prevent aliasing in the decimation operation. It has a gain of L and a cut-off of π/M. Its discrete-time Fourier transform is given

$$H_{lp}(e^{j\omega}) = \begin{array}{ll} L, & 0 \leq \omega \leq \pi/M \\ 0, & \pi/M < \omega \leq \pi \end{array} \tag{B.10}$$

The discrete-time Fourier transform of the output of the low pass filter, for $\pi/M < \pi/L$, is therefore,

$$X_{lp}(e^{j\omega}) = \begin{array}{ll} (L/T)\sum_{k=-\infty}^{\infty} X_c\left(j(\omega L/T) - j(2\pi kL/T)\right), & 0 \leq \omega \leq \pi/M \\ 0, & \pi/M < \omega \leq \pi \end{array} \tag{B.11}$$

The signal is then decimated by an integer factor M. Now, consider the two discrete-time signals, $x_1[n]$ and $x_{lp}[n]$. Let these be two representations of the same continuous-time signal $x_c(t)$. Then, these can be written as

$$x_{lp}[n] = x_c(nT'') \tag{B.12}$$

$$x_1[n] = x_c(nT') \tag{B.13}$$

where, $T' = MT''$. Thus, $x_1[n]$ is a decimated version of the signal $x_{lp}[n]$ and is usually obtained by picking Mth sample of x_{lp}. Then it can be shown that

$$X_1(e^{j\omega}) = \frac{1}{M}\sum_{q=0}^{M-1} X_{lp}(e^{(j\frac{\omega}{M} - j\frac{2\pi q}{M})}) \tag{B.14}$$

Recognizing $x_{lp}[n]$ in Equations B.12 and B.14 as the output of the low pass filter, which has a discrete-time Fourier transform given in Equation B.11, we get

$$X'(e^{j\omega}) = \frac{1}{M}\sum_{q=0}^{M-1}\frac{L}{T}\sum_{k=-infty}^{\infty} X_c\left(j\frac{\omega L}{MT} - j\frac{2\pi qL}{MT} - j\frac{2\pi kL}{T}\right) \tag{B.15}$$

Letting $p = q + kM$, we finally get

$$X'(e^{j\omega}) = \frac{L}{MT}\sum_{p=-\infty}^{\infty} X_c\left(j\frac{\omega L}{MT} - j\frac{2\pi PL}{MT}\right) \tag{B.16}$$

This is nothing but the discrete-time Fourier transform of the desired resampled signal of Equation B.7 as can be recognized by substituting $T' = MT/L$ in Equation B.6. Thus, fractional resampling can be achieved by an integer interpolation followed by low pass filtering and decimation.

B.3 One and Two dimensional Fourier transform

The discrete-time Fourier transform of a sampled data $f(k)$ is defined as

$$F(n) \equiv \sum_{k=0}^{N-1} \exp(2\pi ikn/N) f(k) \tag{B.17}$$

The inverse DFT is similarly defined by

$$f(k) \equiv \frac{1}{N}\sum_{n=0}^{N-1} \exp(-2\pi ikn/N) F(n) \tag{B.18}$$

The only difference between the two formulae given above is the change of sign in the exponential term and a division by N in Equation B.18. Hence, the two transforms can be calculated using the same computer programs.

The DFT is usually evaluated using an algorithm known as Fast Fourier Transform (FFT). In this algorithm, DFT is calculated by a decomposition of N point data array to smaller portions recursively. This decomposition ends at a single data point and the FFT of a single data point is itself. Then, 2 point, 4 point and the higher order DFTs can be computed by appropriate

weighted sum of such decomposed units to finally yield the transform in Equation B.17. These computations are aided by a feature of the algorithm where the final sum can be obtained directly from the data points arranged in a bit-reversed order.

The two dimensional discrete-time Fourier transform (TDFT) is given by

$$F(n_1, n_2) = \sum_{k=0}^{N_2-1} \sum_{l=0}^{N_1-1} \exp(2\pi i k n_2/N_2) \exp(2\pi i l n_1/N_1) f(k, l) \tag{B.19}$$

This can be carried out by performing a series of one- dimensional FFT on the rows of the two dimensional matrix followed by FFT on the column.

Appendix C

DERIVATIONS OF MATHEMATICAL FORMULAE USED IN THESIS

Some useful formulae used in this thesis have been derived in this Appendix.

C.1 MINIMUM OF A PARABOLA

A general parabola is given by

$$y = a_0 + a_1 x + a_2 x^2 \tag{C.1}$$

Its derivative with respect to the independent variable x vanishes at the minimum of the parabola. Hence, the absicca of the minimum is given by

$$x_{min} = \frac{-a_1}{2a_2} \tag{C.2}$$

and the ordinate is given by

$$y_{min} = a_0 - \frac{a_1^2}{2a_2} \tag{C.3}$$

The errors on the absicca and the ordinate in terms of the uncertainties of the fitted parameter are given by,

$$\sigma_{x_{min}} = \sqrt{\frac{1}{4a_2^2}\sigma_{a_1}^2 + \frac{a_1^2}{4a_2^4}\sigma_{a_2}^2} \tag{C.4}$$

$$\sigma_{y_{min}} = \sqrt{\sigma_{a_0}^2 + x_{min}^2\sigma_{a_1}^2 + x_{min}^4\sigma_{a_2}^2 + (a_1 + 2x_{min}a_2)^2\sigma_{x_{min}}^2} \tag{C.5}$$

where, the parameters a_0, a_1, a_2 and x_{min} have been assumed to be uncorrelated.

C.2 STANDARD DEVIATION OF ρ

Let x and y be Gaussian random variables. Then

$$\rho = \frac{1}{N}\sum_i \frac{(x_i - \langle x\rangle)(y_i - \langle y\rangle)}{\sigma_x \sigma_y}, \tag{C.6}$$

where

$$\begin{aligned} \langle x\rangle &= \tfrac{1}{N}\textstyle\sum_i x_i, \quad \sigma_x^2 = \tfrac{1}{N}\textstyle\sum_i (x_i - \langle x\rangle)^2, \\ \langle y\rangle &= \tfrac{1}{N}\textstyle\sum_i y_i, \quad \sigma_y^2 = \tfrac{1}{N}\textstyle\sum_i (y_i - \langle y\rangle)^2. \end{aligned} \tag{C.7}$$

For small changes in x_i and y_i, the change in ρ will be given by

$$\begin{aligned} \tfrac{\delta\rho}{\delta x_i} &= \tfrac{1}{N}\tfrac{1}{\sigma_x}\left[\tfrac{y_i - \langle y\rangle}{\sigma_y} - \rho\tfrac{x_i - \langle x\rangle}{\sigma_x}\right] \\ \tfrac{\delta\rho}{\delta y_i} &= \tfrac{1}{N}\tfrac{1}{\sigma_y}\left[\tfrac{x_i - \langle x\rangle}{\sigma_x} - \rho\tfrac{y_i - \langle y\rangle}{\sigma_y}\right] \end{aligned} \tag{C.8}$$

Now,

$$\begin{aligned} d\rho &= \textstyle\sum_i \left[\tfrac{\delta\rho}{\delta x_i}\delta x_i + \tfrac{\delta\rho}{\delta y_i}\delta y_i\right] \\ \Rightarrow \langle d\rho^2\rangle &= \textstyle\sum_i \left[\left\langle\left(\tfrac{\delta\rho}{\delta x_i}\delta x_i\right)^2\right\rangle + \left\langle\left(\tfrac{\delta\rho}{\delta y_i}\delta y_i\right)^2\right\rangle + 2\left\langle\tfrac{\delta\rho}{\delta x_i}\tfrac{\delta\rho}{\delta y_i}\delta x_i\delta y_i\right\rangle\right] \end{aligned} \tag{C.9}$$

since

$$\langle \delta x_i \delta y_j\rangle = 0;\ \langle \delta x_i (x_j - \langle x\rangle)\rangle = 0;\ \langle \delta y_i (y_j - \langle y\rangle)\rangle = 0;\ \text{etc. for } i \neq j. \tag{C.10}$$

By straightforward algebra, and using $\langle \delta x_i^2\rangle = \sigma_x^2$, $\langle \delta y_i^2\rangle = \sigma_y^2$, and $\langle \delta x_i \delta y_i\rangle = \rho\sigma_x\sigma_y$, one obtains:

$$\begin{aligned} \textstyle\sum_i \left\langle\left(\tfrac{\delta\rho}{\delta x_i}\delta x_i\right)^2\right\rangle &= \tfrac{1}{N}\left(1-\rho^2\right) \\ \textstyle\sum_i \left\langle\left(\tfrac{\delta\rho}{\delta y_i}\delta y_i\right)^2\right\rangle &= \tfrac{1}{N}\left(1-\rho^2\right) \\ \textstyle\sum_i \left\langle\tfrac{\delta\rho}{\delta x_i}\tfrac{\delta\rho}{\delta y_i}\delta x_i\delta y_i\right\rangle &= -\tfrac{1}{N}\rho^2\left(1-\rho^2\right). \end{aligned} \tag{C.11}$$

Using these three terms one gets the standard deviation of the correlation coefficient:

$$\sigma_\rho = \sqrt{\langle d\rho^2\rangle} = \sqrt{\frac{2}{N}}\left(1-\rho^2\right). \tag{C.12}$$

C.3 Error on standard deviation

The standard deviation or RMS deviation is given by

$$\Delta x = \left(\frac{1}{N}\sum_{i=1}^{N}(x_b - x_{si})^2\right)^{\frac{1}{2}} \tag{C.13}$$

Now, if

$$y = z^2 \tag{C.14}$$

the variance on z is given by

$$\sigma_z^2 = \frac{\sigma_y^2}{4\overline{y}} \tag{C.15}$$

Let,

$$\overline{y} \quad = \overline{a}^2 \quad = \tfrac{1}{N}\sum(x_b - x_{si})^2 \quad = \tfrac{1}{N}\sum y_i \tag{C.16}$$

$$\sigma_y^2 = \frac{1}{N}\sum(x_b - x_{si})^4 - \frac{1}{N^2}\left[\sum(x_b - x_s i)^2\right]^2 \tag{C.17}$$

Substituting Equation C.17 in Equation C.15, we get the desired expression

$$\sigma_{\Delta x} = \left(\frac{\frac{1}{N}\Sigma(x_b - x_{si})^4 - (\frac{1}{N}\Sigma(x_b - x_{si})^2)^2}{\frac{4}{N}\sum(x_b - x_{si})^2}\right)^{\frac{1}{2}} \tag{C.18}$$

$$\sigma_{\Delta x} = \left(\frac{\Sigma(x_b - x_{si})^4 - \frac{1}{N}(\Sigma(x_b - x_{si})^2)^2}{4\sum(x_b - x_{si})^2}\right)^{\frac{1}{2}} \tag{C.19}$$

C.4 Error on RMS width of subpulse

The RMS width was defined in Section 4.1.1 as

$$W = \left(\frac{\sum p_i x_i^2}{\sum p_i} - \left[\frac{\sum p_i x_i}{\sum p_i}\right]^2\right)^{\frac{1}{2}} \tag{C.20}$$

Let, $y = W^2$. Then, the variance of y is given by

$$\sigma_y^2 = \sum\left(\frac{\partial y}{\partial p_i}\right)^2 \sigma_{p_i}^2 \tag{C.21}$$

Now, it can be shown that

$$\frac{\partial y}{\partial p_i} = -\left[\frac{x_i(x_i - 2\overline{x})}{\sum p_i^2}\right] \tag{C.22}$$

Substituting Equation C.22 in Equation C.21 and then using the formula in Equation C.15, we get

$$\sigma_w = \left[\frac{\sum\left(\frac{x_i(x_i - 2\overline{x})}{(\sum p_i)^2}\right)^2 \sigma_{p_i}^2}{4W^2}\right]^{\frac{1}{2}} \tag{C.23}$$

C.5 Error on Histogram of measurements

An observed distribution for a measurable quantity can be obtained from its measurements by summing the individual contributions of normalized Gaussians representing individual measurements. Such a histogram, given by the following expression

$$\begin{aligned} H(x) &= \frac{1}{N}\sum_{k=1}^{N}\frac{1}{\sqrt{\pi}\sigma_{a_k}}\exp\left[-\left(\frac{x-a_k}{\sigma_{a_k}}\right)\right] \\ &= \frac{1}{N}\sum_{1}^{N}G_k(x) \end{aligned} \tag{C.24}$$

have been used in this thesis. Here, a_k is the k^{th} measurement of the quantity under consideration and σ_{a_k} is its error. The absicca x spans the range of possible values for the quantity being measured. The error on each point of this curve can be obtained from the measurement errors σ_{a_k} as described below.

From the theory of errors, the variance $V(y)$ on a function $y(a)$ is given by

$$V(y) = \left(\left.\frac{\partial y}{\partial a}\right|_{a=\overline{a}}\right) \tag{C.25}$$

Hence,

$$\begin{aligned} V(H) &= \frac{1}{N^2}\sum_{k=1}^{N}\left(\frac{\partial G_k}{\partial a_k}\right)^2\sigma_{a_k}^2 + \frac{1}{N^2}\sum_{k=1}^{N}\left(\frac{\partial G_k}{\partial \sigma_{a_k}}\right)^2\sigma_{err_k}^2 \\ &= \frac{1}{N^2}\sum_{k=1}^{N}\left(p_k\sigma_{a_k}^2 + q_k\sigma_{err_k}^2\right) \end{aligned} \tag{C.26}$$

where, G_k is as defined in Equation C.24 and σ_{err_k} is the error on the error in a_k. The latter is given by

$$\sigma_{err_k}^2 = \frac{\sigma_{a_k}^2}{2} \tag{C.27}$$

assuming that the measurement a_k is distributed normally. It has been assumed that the a_k and σ_{a_k} are not correlated in arriving at the expression in Equation C.26. The coefficients p_k and q_k are given by

$$p_k = \left(2\left[\frac{x-a_k}{\sigma_{a_k}^2}\right]G_k(x)\right)^2 \tag{C.28}$$

$$q_k = \left(\left[\frac{-1}{\sigma_{a_k}} + \frac{2}{\sigma_{a_k}^3}(x-a_k)^2\right]G_k(x)\right)^2 \tag{C.29}$$

These expressions can be evaluated on any point x on the histogram curve using the measurements and its error to obtain the error on the histogram values.

C.6 Error on cross-correlation of histograms of two quantities

In Chapter 8, the expected distribution of the total drift is obtained by cross correlating the distributions of the turn-off and turn-on phases. The expressions for the error on such a cross-correlations are presented in this section.

The cross-correlation of two histograms of the form given in Equation C.24 is

$$\begin{aligned}\rho(t) &= \int_{-\infty}^{\infty} H_1(x-t)H_2(x)dx \\ &= \int_{-\infty}^{\infty} \frac{1}{N}\sum_{k=1}^{N} \frac{1}{\sqrt{\pi}a_k} \exp\left[-\left(\frac{x-t-b_k}{a_k}\right)^2\right] \times \frac{1}{N}\sum_{j=1}^{N} \frac{1}{\sqrt{\pi}c_j} \exp\left[-\left(\frac{x-d_j}{c_j}\right)^2\right] dx\end{aligned} \tag{C.30}$$

where, H_1 and H_2 refer to the two histograms for the measurements b_k and d_j respectively. The respective errors on the measurements are a_k and c_j. After some algebraic manipulations, the above expression reduces to

$$\begin{aligned}\rho(t) &= \frac{1}{N^2}\sum_{j=1}^{N}\sum_{k=1}^{N} \frac{1}{\sqrt{\pi(a_k^2+c_j^2)}} \exp\left[\frac{-(d_j-b_k-t)^2}{a_k^2+c_j^2}\right] \\ &= \frac{1}{N^2}\sum_{j=1}^{N}\sum_{k=1}^{N} G_{jk}(t)\end{aligned} \tag{C.31}$$

The error on the above expression is given by a straightforward application of Equation C.25, where the cross-correlation between any two measurement or their errors has been ignored. Hence,

$$\begin{aligned}V(\rho) &= \sum_{k=1}^{N}\left[\left(\frac{\partial\rho}{\partial a_k}\right)^2\sigma_{a_k}^2 + \left(\frac{\partial\rho}{\partial b_k}\right)^2\sigma_{b_k}^2\right] + \sum_{j=1}^{N}\left[\left(\frac{\partial\rho}{\partial c_j}\right)^2\sigma_{c_j}^2 + \left(\frac{\partial\rho}{\partial d_j}\right)^2\sigma_{d_j}^2\right] \\ &= \sum_{k=1}^{N}\left[p_k^2\sigma_{a_k}^2 + q_k^2\sigma_{b_k}^2\right] + \sum_{j=1}^{N}\left[r_j^2\sigma_{c_j}^2 + s_j^2\sigma_{d_j}^2\right]\end{aligned} \tag{C.32}$$

The coefficients, p_k, q_k, r_j and s_j are given by

$$p_k = \frac{1}{N^2}\sum_{j=1}^{N}\left[\left(\frac{-a_k}{(a_k^2+c_j^2)} + \frac{2a_k(d_j-b_k-t)^2}{(a_k^2+c_j^2)^2}\right)G_{jk}\right] \tag{C.33}$$

$$q_k = \frac{1}{N^2}\sum_{j=1}^{N}\left[\left(\frac{2(d_j-b_k-t)}{(a_k^2+c_j^2)}\right)G_{jk}\right] \tag{C.34}$$

$$r_j = \frac{1}{N^2}\sum_{k=1}^{N}\left[\left(\frac{-c_j}{(a_k^2+c_j^2)} + \frac{2c_j(d_j-b_k-t)^2}{(a_k^2+c_j^2)^2}\right)G_{jk}\right] \tag{C.35}$$

$$s_j = \frac{1}{N^2}\sum_{k=1}^{N}\left[\left(\frac{-2(d_j-b_k-t)}{(a_k^2+c_j^2)}\right)G_{jk}\right] \tag{C.36}$$

In all the expressions above, G_{jk} are as defined in Equation C.31. It should be noted that σ_{a_k} and σ_{c_j} are the errors on the measurement errors a_k and c_j. These can be obtained in a way similar to that used in Appendix C.5 by using the expression given in Equation C.27. The rest of the terms in the above expressions are just the measurements and the respective errors. These are then used to obtain the desired distribution and the error on this curve.

Appendix D

Interpolation

Often the values of a function $f(x)$ are known at a set of points $x_1, x_2, \ldots, x_N$ although its analytic expression is unknown. The process of estimation of $f(x)$ for an arbitrary $x$in between the smallest and largest of x_i by drawing a smooth curve through x_i is called interpolation. This process models the function by some plausible functional form. Some of the interpolation methods used in this thesis are briefly reviewed in this Appendix. A good description of many schemes for interpolation and extrapolation is given in Press et al. (1992).

D.1 Linear Interpolation

A function $f(x)$, given at N points, can be modeled by an interpolating polynomial of degree $N-1$. This polynomial is given by Lagrange's formula

$$G(x) = \frac{(x-x_2)(x-x_3)\cdots(x-x_N)}{(x_1-x_2)(x_1-x_3)\cdots(x_1-x_N)}y_1 + \frac{(x-x_1)(x-x_3)\cdots(x-x_N)}{(x_2-x_1)(x_2-x_3)\cdots(x_2-x_N)}y_2 + \cdots + \frac{(x-x_1)(x-x_2)\cdots(x-x_{N-1})}{(x_N-x_1)(x_N-x_2)\cdots(x_N-x_{N-1})}y_N \quad \text{(D.1)}$$

where, $y_1 = f(x_1), y_2 = f(x_2), \ldots, y_N = f(x_N)$. A special case of the general Lagrange's formula is linear interpolation, *i.e.*, interpolation by a polynomial of degree one. The above formula reduces to

$$G_l(x) = Ay_1 + By_2 \quad \text{(D.2)}$$

where,

$$A = \frac{x_2 - x}{x_2 - x_1} \quad \text{(D.3)}$$

$$B = \frac{x - x_1}{x_2 - x_1} \quad \text{(D.4)}$$

This method gives a piecewise approximation of the function being modeled, but its second derivative is undefined at the points x_i and it may be discontinuous across such points. It is the simplest interpolation scheme and gives good results for most functions encountered in practice.

This method is used for resampling the data in Section 5.1 and 7.1.1. This technique is a good approximation of the Fourier method discussed in Appendix B.2 as long as the signal does not vary significantly between the two samples of the original data. In other words, if the data is sampled well above the Nyquist rate, linear interpolation is a more convenient method.

D.2 Spline Interpolation

When continuity of higher order derivatives is desirable, the preferred method is to use a spline interpolation. A cubic spline interpolation provides a formula that is smooth in the first derivative and continuous in the second derivative both within an interval and at its boundaries. Let the values of a function be given as $y_i = y(x_i), i = 1 \ldots N$. Then, the cubic spline interpolation is given by the following formulae

$$y = Ay_i + By_{i+1} + Cy_i'' + Dy_{i+1}'' \tag{D.5}$$

where, A and B are as defined in Equations D.3 and D.4, and

$$C = \frac{1}{6}\left(A^3 - A\right)\left(x_{i+1} - x_i\right)^2 \tag{D.6}$$

$$D = \frac{1}{6}\left(B^3 - B\right)\left(x_{i+1} - x_i\right)^2 \tag{D.7}$$

The second derivative in Equation D.5 can be obtained by (1) requiring that the first derivative of y in Equation D.5 be continuous across the boundary between two intervals, and (2) by specifying the value of the second derivative at x_1 and x_N. Most often the latter are specified as zero giving a natural cubic spline. The other derivatives can be obtained from $N-2$ linear equations obtained due to requirement (1). These are

$$\frac{x_i - x_{i-1}}{6}y_{i-1}'' + \frac{x_{i+1} - x_{i-1}}{3}y_i'' + \frac{x_{i+1} - x_i}{6}y_{i+1}'' = \frac{y_{i+1} - y_i}{x_{i+1} - x_i} - \frac{y_i - y_{i-1}}{x_i - x_{i-1}} \tag{D.8}$$

The spline interpolation is usually carried out in two steps. First, the second derivatives at all the points, where the value of the function to approximated is given, are evaluated by solving Equation D.8. This equation specifies what is known as a tridiagonal set of linear equations because each y_i'' is coupled only to its two nearest neighbours $i-1$ and $i+1$. Such linear equations have a very simple form of LU decomposition and are convenient to solve.

Once the second derivatives are evaluated, any number of interpolated values can be evaluated using Equation D.5 appropriate number of times.

Bibliography

Arons, J., 1981a, ApJ, 248, 1099

Arons, J., 1981b, in Proceedings of the Varenna Summer School and Workshop on Plasma Astrophysics, (ESA). Edited by T. Guyenne, pp. 273–275

Arons, J., 1983, ApJ, 266, 215

Arons, J., Scharlemann, E. T., 1979, ApJ, 231, 854

Baade, W., Zwicky, F., 1934, Proc. Natl. Acad. Sci. USA., 20, 254

Backer, D. C., 1970a, Nature, 228, 752

Backer, D. C., 1970b, Nature, 228, 1297

Backer, D. C., 1970c, Nature, 228, 42

Backer, D. C., 1973, ApJ, 182, 245

Backer, D. C., Rankin, J. M., Campbell, D. B., 1975, ApJ, 197, 481

Bartel, N., et al., 1982, ApJ, 258, 776

Benford, G., Buschauer, R., 1977, Mon. Not. R. Astron. Soc., 179, 189

Bertsch, D. L., et al., 1992, Nature, 357, 306

Biggs, J. D., 1990, Mon. Not. R. Astron. Soc., 246, 341

Biggs, J. D., 1992, ApJ, 394, 574

Biggs, J. D., et al., 1985a, Mon. Not. R. Astron. Soc., 215, 281

Biggs, J. D., et al., 1985b, Mon. Not. R. Astron. Soc., 214, 47

Camilo, F., et al., 2000, in Proceedings of the 177th Colloquium of the IAU, "Pulsar astronomy - 2000 and beyond", ASP Conference Series, (San Fransisco: ASP). Edited by M. Kramer and N. Wex and R. Wielebinski, Vol. 202, pp. 3–8

Cheng, A. F., Ruderman, M. A., 1977a, ApJ, 214, 598

Cheng, A. F., Ruderman, M. A., 1977b, ApJ, 212, 800

Cheng, A. F., Ruderman, M. A., 1980, ApJ, 235, 576

Cole, T. W., 1970, Nature, 227, 788

Curtis Michel, F., 1991, Theory of Neutron Star Magnetospheres, University of Chicago Press, Chicago, first edition

Davies, J. G., et al., 1984, Mon. Not. R. Astron. Soc., 211, 57

Deich, W. T. S., et al., 1986, ApJ, 300, 540

Deshpande, A. A., Rankin, J. M., 1999, ApJ, 524, 1008

Drake, F. D., Craft, H. D., 1968, Nature, 220, 231

Erber, T., 1966, Rev. Mod. Phys., 38, 626

Fawley, W. M., Arons, J., Scharlemann, E. T., 1977, ApJ, 217, 227

Ferguson, D. C., et al., 1981, Astron. Astrophys., 94, L6

Filippenko, A. V., Radhakrishnan, V., 1982, ApJ, 263, 828

Fowler, L. A., Wright, G. A. E., 1982, Astron. Astrophys., 109, 279

Fowler, L. A., Wright, G. A. E., Morris, D., 1981, Astron. Astrophys., 93, 54

Gil, J. A., Sendyk, M., 2000, astro-ph, 0002, 0002450

Gil, J. A., et al., 1994, Astron. Astrophys., 282, 45

Gold, T., 1968, Nature, 218, 731

Gold, T., 1969, Nature, 221, 25

Goldreich, P., Julian, W. H., 1969, ApJ, 157, 869

Goldstein, S. J., James, J. T., 1969, ApJ Letters, 158, L179

Halpern, J. P., Holt, S. S., 1992, Nature, 357, 222

Hankins, T. H., Wolszczan, A., 1987, ApJ, 318, 410

Helfand, D. J., Manchester, R. N., Taylor, J. H., 1975, ApJ, 198, 661

Hesse, K. H., Wielebinski, R., 1974, Astron. Astrophys., 31, 409

Hewish, A., et al., 1968, Nature, 217, 709

Hillebrandt, W., Muller, E., 1976, ApJ, 207, 589

Huguenin, G. R., Manchester, R. N., Taylor, J. H., 1971, ApJ, 169, 97

Huguenin, G. R., Taylor, J. H., Troland, T. H., 1970, ApJ, 162, 727

Interactive Data Language, 1995, Interactive Data Language, Research Systems Inc., Boulder, version 4 edition

Izvekova, V. A., Kuzmin, A. D., Shitov, Y. P., 1982, Soviet Astr., 26, 324

Izvekova, V. A., et al., 1993, Mon. Not. R. Astron. Soc., 191, 237

Jones, P. B., 1983, Mon. Not. R. Astron. Soc., 153, 337

Kazbegi, A., et al., 1996, Astron. Astrophys., 309, 515

Komesaroff, M. M., 1970, Nature, 225, 612

Krishnamohan, S., 1980, Mon. Not. R. Astron. Soc., 191, 237

Lorimer, D. R., et al., 1995, Mon. Not. R. Astron. Soc., 273, 411

Lyne, A. G., 1971, Mon. Not. R. Astron. Soc., 153, 27

Lyne, A. G., Ashworth, M., 1983, Mon. Not. R. Astron. Soc., 204, 519

Lyne, A. G., Graham-Smith, F., 1990, Pulsar Astronomy, Cambridge University Press, Cambridge, first edition

Lyne, A. G., Lorimer, D. R., 1994, Nature, 369, 127

Manchester, R. N., Taylor, J. H., 1981, Astron. J., 86, 1953

Manchester, R. N., Taylor, J. H., Huguenin, G. R., 1975, ApJ, 196, 83

Marquardt, D. W., 1963, J. Soc. Ind. Applied Math., 11, 431

Melrose, D. B., 1993, in Pulsars as Physics laboratories, Phil. Trans. of Royal Society of London. (Oxford: Oxford University Press). Edited by R. D. Blandford and A. Hewish and A.G. Lyne and L. Mestel, pp. 105–112

Michel, F. C., 1974, ApJ, 192, 713

Michel, F. C., 1991, Theory of Neutron Star Magnetosphere, The University of Chicago Press, Chicago, first edition

Morris, D., Graham, D. A., Bartel, N., 1981, Mon. Not. R. Astron. Soc., 194, 7

Morris, D., et al., 1980, Astron. Astrophys., 84, 260

Nowakowski, L., et al., 1981, Astron. Astrophys., 116, 158

Nowakowski, L. A., 1994, Astron. Astrophys., 281, 444

Oppenheim, A. V., Schafer, R. W., 1989, Discrete-Time Signal Processing, Prentice Hall, Englewood Cliffs, New Jersey, first edition

Oster, L., Hilton, D. A., Sieber, W., 1977, Astron. Astrophys., 57, 1

Oster, L., Sieber, W., 1976, ApJ, 210, 220

Pacini, F., 1968, Nature, 219, 145

Pacini, F., Salpeter, E. E., 1968, Nature, 218, 733

Page, C. G., 1973, Mon. Not. R. Astron. Soc., 163, 29

Press, W. H., et al., 1992, Numerical Recipes in FORTRAN, Cambridge University Press, Cambridge, second edition

Proszynski, M., Wolszczan, A., 1986, ApJ, 307, 540

Radhakrishnan, V., Cooke, D. J., 1969, Astrophys. Lett. Commun., 3, 225

Rankin, J. M., 1983, ApJ, 274, 333

Rankin, J. M., 1986, ApJ, 301, 901

Rankin, J. M., Wolszczan, A., Stinebring, D. R., 1988, ApJ, 324, 1048

Ritchings, R. T., 1976, Mon. Not. R. Astron. Soc., 176, 249

Ritchings, R. T., Lyne, A. G., 1975, Nature, 257, 293

Ruderman, M. A., Sutherland, P. G., 1975, ApJ, 196, 51

Scharlemann, E. T., Arons, J., Fawley, W. M., 1978, ApJ, 222, 297

Selvanayagam, A. I., et al., 1993, Inst. Elec. Telecom. Engg. Tech. Rev., 10, 4

Seward, F. D., 1984, ApJ Letters, 287, L19

Seward, F. D., Harnden, F. R., 1982, ApJ Letters, 256, L45

Sturrock, P. A., 1971, ApJ, 164, 529

Subrahmanyan, R., 1989, Observational Constraints on the formation of pre-galactic condensates in the Universe, Ph.D. thesis, Indian Institute of Sciences, Bangalore

Sutton, J. M., et al., 1970, ApJ Letters, 159, L89

Swarup, G., et al., 1971, Nature Physical Sciences, 230, 185

Taylor, J. H., Huguenin, G. R., 1971, ApJ, 167, 273

Taylor, J. H., Manchester, R. N., Huguenin, G. R., 1975, ApJ, 195, 513

Unwin, S. C., et al., 1978, Mon. Not. R. Astron. Soc., 182, 711

Vivekanand, M., 1995, Mon. Not. R. Astron. Soc., 274, 785

Vivekanand, M., Joshi, B. C., 1995, Bull. Astron. Soc. India, 23, 479

Wolszczan, A., 1986, Astron. Astrophys., 86, 7

Wolszczan, A., Bartel, N., Sieber, W., 1981, Astron. Astrophys., 100, 91

Wright, G. A. E., 1981, Mon. Not. R. Astron. Soc., 196, 153

Wright, G. A. E., Fowler, L. A., 1981a, Astron. Astrophys., 101, 356

Wright, G. A. E., Fowler, L. A., 1981b, in Proceedings of the 95th Symposium of the IAU, "Pulsars - 13 years of Research on Neutron stars", (Dordrecht: D. Reidel Publishing Company). Edited by W. Sieber and R. Wielebinski, pp. 211–212

Wright, G. A. E., Sieber, W., Wolszczan, A., 1986, Astron. Astrophys., 160, 402

Xu, R. X., Qiao, G. J., Zhang, B., 2000, in Proceedings of the 177th Colloquium of the IAU, "Pulsar astronomy - 2000 and beyond", ASP Conference Series, (San Fransisco: ASP). Edited by M. Kramer and N. Wex and R. Wielebinski, Vol. 202, pp. 665–666

Zhang, B., et al., 1997, ApJ, 478, 313